Optimal locations for the ground segment of optical space communications networks
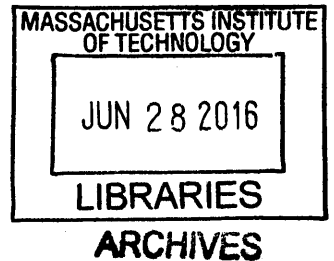
by

Iñigo del Portillo Barrios

Submitted to the Department of Aeronautics and Astronautics
in partial fulfillment of the requirements for the degree of

Master of Science in Aeronautics and Astronautics

at the

MASSACHUSETTS INSTITUTE OF TECHNOLOGY

June 2016

Author . . . .

Signature redacted

Department of Aeronautics and Astronautics
May 18, 2016

Certified by . . . . . .

Signature redacted

Prof. Edward F. Crawley
Professor of Aeronautics and Astronautics and Engineering Systems
Thesis Supervisor

Certified by .

Signature redacted

Dr. Bruce Cameron
Director, System Architecture Lab
Thesis Supervisor

Accepted by . .

Signature redacted

Prof. Paulo C. Lozano
Associate Professor of Aeronautics and Astronautics
Chair, Graduate Program Committee

Optimal locations for the ground segment of optical space communications networks

by

Iñigo del Portillo Barrios

Abstract

Optical communications are envisioned as a key technology for space communication in the near future. This transition to optical terminals is being pushed by the higher data volume demand of certain missions and by the spectrum encroachment in current RF bands. In addition, optical systems present multiple advantages with respect to RF terminals, such as their lower mass, size, and power, as well as the higher data-rate. However, one of the main issues of using optical systems is the space-to-ground link, as it is impossible for the laser beam to penetrate atmospheric clouds. Geographic diversity of ground stations has been proposed as an alternative to mitigate these effects.

This thesis uses the systems architecture approach to analyze different architectures for the ground segment of an optical space communications network to serve low Earth orbit (LEO) missions. In particular, we analyze the tradespace characterized by three decisions: 1) number and location of optical ground stations, 2) use of geostationary relay satellites vs. the direct-to-Earth approach and 3) presence of crosslinks among relay satellites.

Previous analyses studied the problem of mitigating cloud outage through site diversity both from a simulation perspective (working with point designs or a reduced tradespace composed of a fixed set of candidate locations), and from an analytical standpoint after assuming various simplifying hypotheses (independence of ground stations, uniform cloud conditions across the globe). This thesis expands those assumptions, presents a tool to analyze scenarios where no constraints are placed in the location and proposes a new cloud model to obtain first order approximations for the network availability.

In order to analyze the availability of a network of optical ground stations, we use historical weather data from the National Oceanic and Atmospheric Administration (NOAA) and the cloud fraction dataset from Aqua's and Terra's MODIS instruments to characterize weather conditions across the globe. Next, we present the Optical Network Ground Segment Analyzer (ONGSA), a network simulator that incorporates the cloud models to simulate operations of the optical network. Finally we

employ ONGSA to explore the aforementioned tradespace and analyze both cost and performance (in terms of availability) for each architecture.

Results show that a maximum availability of 95.5 % can be achieved using an architecture similar to the actual system (the Tracking and Data Relay Satellite System) and 12 additional optical ground stations. Furthermore, an unconstrained optimization analysis identified the north of Mexico, southwest of Saudi Arabia, Morocco and central Australia as areas with high potential to construct new ground stations. Building new ground stations was identified to be a more cost-effective solution when the required level of availability is high, while using existing infrastructure is a better solution for systems when the required optical availability is low. Our analysis shows that inter-satellite links (ISL) are a cost-effective solution that adds an extra mitigation layer to combat the effects of cloud coverage. In particular, having ISL results in an increase in availability from 80% with six ground stations to 98.7% with the same number of ground stations.

Thesis Supervisor: Prof. Edward F. Crawley
Title: Professor of Aeronautics and Astronautics and Engineering Systems

Thesis Supervisor: Dr. Bruce Cameron
Title: Director, System Architecture Lab

Acknowledgments

THIS PAGE INTENTIONALLY LEFT BLANK

Contents

THIS PAGE INTENTIONALLY LEFT BLANK

List of Figures

11

THIS PAGE INTENTIONALLY LEFT BLANK

List of Tables

THIS PAGE INTENTIONALLY LEFT BLANK

Chapter 1

Introduction

1.1 Motivation

Since its creation in 1958, NASA has developed and maintained a set of communication networks to support the needs of their manned, robotic and Earth observation programs. These networks have continuously evolved, with the purpose of meeting and adjusting to the requirements established by the missions they served.

The evolution of the communications networks is an on-going effort. In 2006 NASA created the Space Communication and Navigation (SCaN) organization to centralize the management of all their communications and tracking networks: the Near Earth Network (NEN), the Deep Space Network (DSN) and the Space Network (SN). The motivation to create this new managerial office was to have a "unified space communications and navigation network infrastructure capable of meeting both robotic and human exploration mission needs" [47], to ensure that the infrastructure provided the highest data rates feasible, and to protect NASA's interests regarding spectrum management.

To accomplish these tasks, SCaN launched several architectural studies to better understand the needs and alternative architectures for NASA's future communications networks. These studies covered a broad spectrum of areas, such as user needs forecast, temporal phase-out/phase-in analyses for new and current assets, as well as architectural evolution studies in the short and long term. One of these recent studies,

17

referred to as the Earth Regimes Network Evolution Study (ERNESt) [21], analyzed different architectural alternatives for NASA's communication networks in 2025 and beyond. The main outcomes of the study were two. First, a new user-initiated services operations concept analogous to today's terrestrial cellphone networks was proposed; second, the study envisioned and advocated for the transition from radio-frequency (RF) to optical technology as the main enabler of higher data-rates and advanced communication services in the future. Figure 1-1 shows a conceptual representation of the proposed architecture in the 2040 horizon. Note how optical links (marked in red lines) play a significant role both as inter-satellite links (ISL) and as space-to-ground (SGL) links.
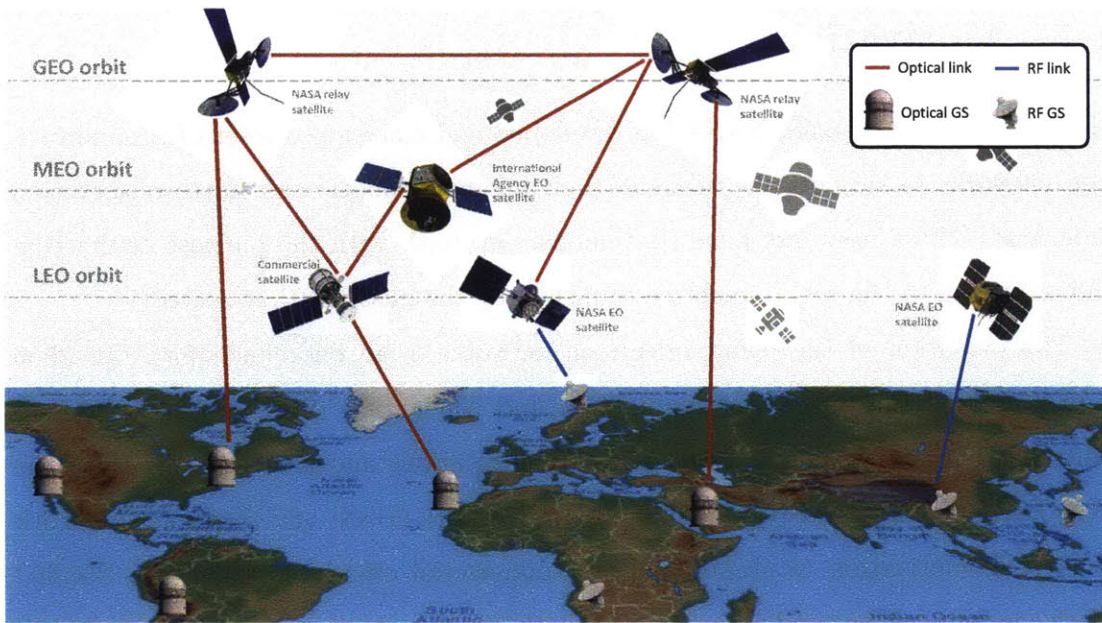
Figure 1-1: ERNESt reference architecture for the year 2040. Image adapted from [21]

This transition to optical communications imposes several new engineering challenges that span from more accurate pointing, acquisition, and tracking, to new protocols that operate in high-speed delay-tolerant environments. Moreover, mitigation of the weather effects in the SGL, in particular the attenuation of the scintillation caused by the atmospheric channel, has become a main research topic. More importantly, cloud coverage over the receiving ground stations causes link outages, which

deteriorate the overall availability of the network. Mitigating the effects of these link outages is the main topic of this thesis.

One of the solutions proposed to the cloud coverage problem is site diversity. By deploying multiple optical ground stations, the link outage probability is reduced; if a cloud blocks an on-going communication between a satellite and an optical ground station (OGS), the satellite can hand over the communication to another OGS that has clear skies. However, constructing such a network of optical ground stations is costly, and therefore several analyses need to be carried out prior to its deployment to determine the optimal locations for the new facilities. This determination is a complex effort, as there are trade-offs between multiple factors such as geographical location, political considerations, or atmospheric conditions, which play a crucial role when determining the best locations. Most previous studies have simulated the cloud conditions (obtained from historical data) over a fixed and pre-existing set of candidate locations. However, no studies have been carried out to determine the optimal locations globally for the ground segment of an optical space communications network. In addition, none of the previous work provides an explicit cost model to analyze the trade-off between performance and cost.

This thesis covers these deficiencies by creating a global cloud model that allows us to evaluate the cloud availability of arbitrary networks of OGSs, together with a comprehensive cost model to assess their cost. Both models are applicable worldwide such that any point on Earth can be selected as a candidate location for an OGS. These models are integrated into the Optical Network Ground Segment Analyzer (ONGSA), a computational tool to assess the cost and availability of a particular network quickly, so that tradespace exploration analysis can be conducted.

1.2   Generic problem statement

The previous section identified the need to conduct analyses that determine the architecture of the ground segment for NASA's future space communications network. In particular, these analyses need to address three main goals:

- To characterize the cloud coverage probability worldwide. This analysis should consider a timespan long enough to capture temporal correlations among candidate locations. Similarly, the spatial correlations among close locations need to be captured. Finally, in order to allow for large tradespace exploration, the cloud model should be simple enough to compute quickly the availability of a network of ground stations.

- To develop a model that allows us to compare the costs of using existing assets against the costs of building new facilities. This cost model should consider the main driving factors involved in building and maintaining the facility throughout its life cycle.

- To build an optimization engine that searches and identifies the optimal architectures from a large space of ground segment design alternatives. The optimization engine must be able to adapt to different scenarios (e.g., a fixed set of candidate OGSs, an unconstrained scenario where new optimal locations need to be discovered).

1.3 Background

This section provides the required background to understand the context for the rest of this thesis. The section starts with a brief history of the space communications networks, emphasizing the development of the ground segment in the last 50 years. Next, the characteristics of free space optics (FSO) are described. Finally, the requirements for an OGS are analyzed. Readers familiar with the evolution of the ground segment of NASA's space communication networks and knowledgeable about the challenges that the atmospheric channel introduces in optical communications may skip this section.

1.3.1 History of space communications ground segment networks

In 1955, three years before NASA was created, the United States Naval Research Laboratory built Minitrack, a worldwide network of ground stations, with the hope of tracking the first artificial satellite. The equipment for Minitrack's ground stations included interferometers and Yagi antennas, which allowed tracking of satellites whose orbits had an inclination lower than 45 degrees. In 1959, NASA took over management of the Minitrack network and expanded it from nine ground stations to a total of twelve facilities. NASA used this network together with the Smithsonian Astrophysical Observatory 12-station network, which was equipped with Baker-Nunn cameras to track satellites optically for NASA's Vanguard Project. As Fred L. Whipple, astronomer in charge at Harvard College's Observatory, explained of the design of the Smithsonian network, the location of these ground stations was driven by the cloud coverage requirements of the optical ground stations, whereas the ground facilities of Minitrack were placed according to electromagnetic and geographical considerations [16].

In the 1960s, as satellites evolved in size and capabilities, it became clear that Minitrack could not provide them with the required quality of service. For example, satellites in polar and sub-synchronous orbits could not be served by Minitrack, since the existing antennas were too small for the larger data return bandwidths, and the level of automation for telemetry and command handling was insufficient. These deficiencies were addressed by adding and closing several sites (up to a total of 23 sites), building larger 12- and 26-meter antennas (SATAN), and adding an alternative tracking device (GRARR). This network, called the Space Tracking and Data Acquisition Network (STADAN), was downsized to 17 ground stations in 1968, after the tracking and acquisition equipment benefited from improved automation.

In parallel with these efforts, Mercury, the first manned human space exploration program at NASA's Manned Spacecraft Center in Houston, required global continuous coverage with two-way communications, ranging and orbit determination for all their

manned missions. To satisfy these specifications, the Manned Spaceflight Network (MSFN), a network of 17 stations around the world, was built. In addition to these ground stations, the MSFN was supported by Department of Defense (DoD) naval ships (particularly in the Pacific region) and aircraft with voice relay and radar equipment.

The MSFN had several upgrades and modifications during its lifetime, adding and closing different stations for the different programs it supported. For example, project Gemini required upgrades in terms of computerization and centralization of the network, which subdivided the ground facilities into primary and secondary stations. The first round of Apollo flights was supported by 14 primary stations (26-m USB antennas), five ships, five aircraft, four secondary stations (9-m S-band antennas) and nine DoD owned stations. Once Apollo missions abandoned low Earth orbit and moved to cis-lunar orbits, the antennas of the Deep Space Network (DSN) were also used as support dishes. By 1972, after the Apollo program was canceled and the number of manned flights planned declined drastically, it was clear that both the MSFN and STADAN were too expensive to be operated separately. Therefore, NASA's administration consolidated both networks into the Spaceflight Tracking and Data Network (STDN), composed of 17 ground stations in total. In the following years, the network gradually lost some of its facilities and several improvements were undertaken to upgrade the existing antennas.

In 1973, as the cost of maintaining a large network of ground stations to provide global coverage kept increasing, Goddard Space Flight Center personnel requested of the industry an analysis of the Tracking and Data Relay Satellite System (TDRSS). TDRSS was a disruptive new idea, where a network composed of two geostationary satellites separated by 130 degrees would support scientific and manned missions by tracking spacecraft and providing them with communication relaying services to transmit the information to an 18-meter dish antenna at the White Sands Test Facility, New Mexico. After multiple budget cuts, delays in the project and discussions in Congress, the first TDRSS satellite was launched in 1983, marking the start of a new era of space communications. Up to seven satellites from this first generation of

TDRSS were launched between 1983 and 1995. This network, referred as the Space Network (SN), was further improved in 1990 with the construction of Guam Remote Ground Terminal (GRGT) which covered the exclusion gap above the Indian Ocean Region and provided full coverage to LEO satellites. Since then, there have not been major changes in the architecture of TDRSS. A second generation of satellites that included Ka-band support was launched between 2002 and 2004, and a third generation with S-band beamforming capabilities was developed and launched in 2013 and 2014.

Over time, the STDN network evolved to what is now the Near Earth Network (NEN), consisting of six NASA-operated ground stations and ten commercial ones that provide downlink services to Earth Observation satellites (mainly in polar orbits) using a variety of antennas with diameters ranging from 4 to 18 m.

More recently, NASA engaged in efforts to consolidate the existing networks under a single management division and to determine the future architecture and requirements of the space communication network. In 2006, the Space Communications and Navigation (SCaN) was created to lower the cost and unify the management division of all communications assets under NASA. This division is in charge of integrating the SN, NEN, and DSN, as well as defining the requirements for and shaping the architecture of NASA's communication network for the years to come.

In line with the previous cost-reduction efforts, SCaN launched the SCAWG study in 2004, whose main goal was to determine the future architecture of the SN. The study focused on the analysis and comparison of several hand-picked different architectures to analyze the trade-offs between RF vs. optical, orbital location of relay satellites in LEO, MEO, GEO and sun-centered, and ISL in relay satellites vs. autonomous relay satellites. The main findings and recommendations of SCAWG were to maintain the GEO relay satellites due to the lowest cost, complexity and ease of transition, and the use of GEO as the baseline for future analyses.

In 2012, NASA launched the Space-Based Relay Study (SBRS) where partners from Industry, the Massachusetts Institute of Technology, as well as in-house expert analyzed a broad range of architecture alternatives that analyzed several factors for

the final solution: procured spacecraft vs. hosted payloads, fractionated spacecraft vs. monolithic architectures, dispersed constellations vs. GEO satellites, optical technology vs. RF band. In this study, NASA and its industry partners focused on single-point designs, whereas MIT developed ITACA [34], a computational tool that allowed for evaluation of tradespaces of thousands of architectures. Note the difference in the approach; while NASA hand-picked several architectures to analyze according to expert's knowledge, MIT developed a methodology (i.e., system architecture) to automatically synthesize and evaluate thousands of architectures, and reveal the insights of the tradespace constituted by the set of decisions previously mentioned.

The SBRS study was followed in 2014 by the ERNESt study, whose main recommendations were to move away from scheduled services towards a user-initiated services approach and to progressively transition from RF technology to optical technologies. The methodology used for the ERNESt study leveraged parts of the SBRS study methodology (e.g., incorporating user mission requirement, Technology assessments, and figure of merits for architecture evaluation) and complemented it on other areas (e.g., synthesis of complete architectures). However, the ERNESt study did not apply a system architecture methodology but analyzed single point designs to come up with an abstract recommended architecture for the NASA's future integrated space communications network. As the proposed architecture is very abstract in some aspects (e.g., location of the ground segment assets), further studies that analyze in depth various aspects of the architecture are required. This thesis goal is to use systems architecture to analyze the alternatives for the ground segment of an optical space communication network to serve LEO missions.

1.3.2   Free space optical communications fundamentals

Free space optical communications (FSO) comprises a set of telecommunications technologies that uses light to wirelessly transmit information between two users. In comparison to optical transmission lines such as fiber optics, FSO do not require a physical connection between the transmitter and receiver. Instead, transmission takes place through free space. Free space is a broad term that includes air, vacuum,

outer space, or any other medium that does not involve a waveguide. Primitive forms of FSOs, such as fire torch signal towers in defensive walls, were used by various ancient cultures as warning systems. The invention of LASERS in the 1960s created a new field of research for FSO, although the interest declined after optical fibers were widely deployed. However, this interest has boosted again due to the new and powerful applications of FSO in the military, space and commercial communications industries.

In particular, FSOs are envisioned as a disruptive technology for space communications in the near future. Several researchers have proposed hybrid RF-optical networks using both space and ground based assets, in which RF equipment is substituted for optical technology for inter-satellite links (ISL) and space-to-ground links (SGL) [5], [21], [18].

This transition to optical terminals in the space-industry is being pushed by higher data volume demands of missions forecast on the 2040 horizon, and by the spectrum encroachment caused by the increasing demand for current RF bands by mobile telecommunications providers [21]. As an example, the DESDyNI (now canceled) and NISAR missions had a joint down-link requirement of 60 Tb/day, whereas nowadays the data-volume transmitted daily by the space network (SN) is roughly 40 Tb. In addition, several studies show that optical systems outperform traditional RF communication systems in terms of weight, size, power, and data-rate [26], [19]. Finally, the most recent demonstrations of free space optical communications systems show that we are at a point where the high technology readiness level (TRL) and lower costs associated with FSO technology make it viable for operational deployment and architecting networks that will replace current RF-based systems.

Free space optical communications that propagate through the Earth's atmosphere experience disturbances in the received signal due to the atmospheric attenuation and turbulence. This results in signal fades, wavefront disturbance, background light due to direct sunlight, and beam spreading at the receiver focal plane. The most important source of attenuation is absorption due to clouds and fog. Rain-cloud coverage introduces an attenuation on the link up to 200 dB/km [28], which often

makes it impossible to close the link budget under the presence of clouds.

As such, one of the main challenges in switching from RF SGL to optical SGL is ensuring network availability in the presence of clouds. As the optical beam cannot penetrate clouds, link disruption occurs in the event of covered skies over the receiving ground stations. A proposed solution to mitigate weather outage is site diversity of the receiver stations. This way, if a satellite locks onto an optical ground station (OGS) and a cloud blocks the link during its transmission it can switch to another OGS and continue downloading its data to Earth. Therefore, site diversity on the ground segment increases the network availability.

The improvement in availability largely depends on the number and location of the ground stations. A network with a very high number of OGSs may achieve an excellent performance in terms of availability, but at the same time it might result in exorbitant maintenance costs that render the system unaffordable. Therefore, a compromise between performance and cost must be achieved when determining the location of the ground stations.

In addition to cloud coverage, precipitation and aerosols introduce another source of attenuation and scattering. Furthermore, fluctuations in the received signal are caused by variations of the atmospheric refractive index. These fluctuations are normally captured by the refractive index structure constant $C_n^2(h)$ [1]. Different models (both empirical and experimental) have been developed to approximate the value of $C_n^2(h)$, the most famous being the Hufnagel-Valley (HV5/7) model, the Submarine Laser Communications (SLC) model, and the CLEAR 1 model. The refractive index structure constant defines the three-dimensional Kolmogorov spectrum of the refractive index, which is the base for further calculations such as the scintillation index as:

$$\sigma_I = \frac{\langle (I - \langle I \rangle)^2 \rangle}{\langle I \rangle^2} = \exp\left(4 \left[0.56 k^{7/6} sec(\theta)^{11/6} \int_{h_0}^{h_0+L} C_n^2(h)(h - h_0)^{5/6} dh \right]^2 \right) - 1 \quad (1.1)$$

with I being the received intensity, $C_n^2(h)$ the refractive index structure constant, h_0 the altitude of the receiver telescope, L the distance between the transmitter and

receiver, and θ the zenith angle formed between source and receiver. The scintillation index is then used to compute the statistical distribution of scintillation as:

$$p_I(I) = \frac{1}{\sqrt{2\pi}I\sigma_I}\exp\left[-\frac{\ln\frac{I}{\langle I\rangle}+\frac{1}{2}\sigma_I^2}{2\sigma_I^2}\right]$$ (1.2)

with σ_I^2 being the scintillation index (normalized variance of the intensity fluctuations).

These intensity fluctuations are normally modeled as an extra losses term in the link budget equation. However, there are several techniques to mitigate the disturbance created by the atmospheric channel. These counter-measures include aperture averaging; the use of temporal, spatial and wavelength diversity; or the use of interleavers. Aperture averaging consists of using a telescope with a large diameter to average out the scintillation effects. Temporal, spatial and wavelength diversity techniques make use of the independence of retarded signals in the temporal domain, multiple receiver apertures in the spatial domain and different attenuations over different wavelengths in the frequency domain, respectively. Finally, interleavers spread the errors generated by the scintillation of the received signal (of bursty nature) over multiple frames so that they can be corrected by using a FEC code. Although interleavers introduce a considerable delay in the data-pipeline (on the order of a couple of 100 ms) the gain in performance that can be achieved outperforms other options.

1.3.3 Optical ground stations requirements

Optical ground stations locations are chosen with the aim of mitigating as much as possible the atmospheric turbulence effects on the laser beam. The ideal location for an optical ground station must meet the following requirements, as described in [18]:

- Low probability of link outage due to cloud coverage. As clouds are the main cause of link outages, having favorable atmospheric conditions is the main driver in the site selection.

- Being located at high altitude with the purpose of reducing the optical air mass that the laser has to traverse and minimizing the effects of atmospheric turbulence over the laser beam.

- Not isolated from common-purpose infrastructures and within a reasonable distance of a wide area network (WAN) point of access, as isolated sites will impose additional costs on the OGS.

- In a politically stable country, where the security of the communications from the receiver OGS and the mission operations center (MOC) can be guaranteed.

- In case of using GEO relay satellites, preferably close to the equator to reduce the slant range and operate in angles close to the zenith angle.

- Located in areas where natural features and man-made structures do not interfere in the line of sight of the laser beam, allowing for operational angles of 0 to 360 degrees in azimuth, and 0 to 90 degrees in elevation.

The previous literature (see Section 1.4) has proposed several existing facilities to act as OGSs. For example, astronomical observatories satisfy most of the requirements described above, but are normally located in isolated areas where high-speed WAN access points are not available, incurring an important cost in that sense. Similarly, existing ground stations from the DSN, the SN, or the NEN are often located at polar latitudes, in order to maximize the number of times that satellites fly over them. However, the cloud coverage probabilities at these high latitude locations are usually too high to guarantee acceptable network availability. Table 1.1 compares the set of requirements met by the different groups of existing assets proposed in previous work to act as OGSs.

Table 1.1: Comparison of the requirements met by different candidate OGS locations

Candidate locations	Cloud Probability	High Altitude	Not isolated	Political Stable	Equatorial latitude
NEN stations	No	No	No	Yes	Some
DSN / SN stations	Some	No	Yes	Yes	Some
Astronomical observatories	Yes	Yes	No	Yes	No

In reality, none of these facilities were originally built with the purpose of becoming optical ground stations that receive data from a high-throughput relay satellite. Therefore the following research question arises. Do existing ground station facilities offer the best conditions in which place an optical ground station, or should new locations be considered? In other words, should we restrict ourselves to the existing facilities, or should we explore the unconstrained tradespace?

1.4 Literature review

Several studies of optimal locations for a set of optical ground stations have been conducted. From a high-level perspective, they can be categorized according to different aspects such as location of the ground stations, tradespace size, or methods used. Table 1.2 summarizes the different attributes of the most relevant previous analyses of cloud coverage and network availability according to these criteria.

The rest of this section explains and provides more details about each of the investigations and their results. This section is sub-divided into three categories. *Single point designs* contains remarks about work where simulation was used to evaluate the availability of a low number (< 11) of architectures. *Tradespace exploration* describes cases where many architectures were simulated and optimization was used to derive the best ones. Finally, *Analytical models* details research that involves the use of an analytical approach instead of simulation to evaluate the availability of a network of OGSs.

Table 1.2: Comparison of the previous work on availability analysis for optical communications

Author	Deep Space	GEO	LEO	Location Ground Stations	Evaluated Tradespace Size (#)	Candidate OGS Location (#)	Perf. Metric	Cost Model	Link Outage Approach	Optimization Methodology
Perlot	No	Yes	No	Europe	Small (1)	Single Point	Availability	No	Analytic	Single Point
Piazzola	No	Yes	No	N. America	Small (1)	Single Point	Data Volume	No	Image Data	Single Point
Poulenard	No	Yes	No	Europe	Small (4)	Fixed (25)	Availability	Backhaul	Image Data	Hand Picked
Tamayaka	No	No	Yes	Japan	Small (6)	Fixed (8)	Availability	No	Analytic	Hand Picked
Poulenard	No	No	Yes	Europe	Small (11)	Fixed (10)	Data Volume	No	Analytic	Hand Picked
Link	Yes	No	No	N. America	Small (512)	Fixed (12)	Availability	No	Image Data	Hand Picked
Fuchs	No	Yes	No	Europe	Medium(10^3)	Fixed (66)	Availability	No	Image Data	Custom Algorithm
OLSG	Yes	Yes	Yes	N. America	Medium (10^4)	Fixed (14)	Availability	Yes	Image Data	Full Enumeration
Wojcik	Yes	No	No	Worldwide	Medium (10^5)	Fixed (30)	Availability	No	Image Data	Custom Algorithm
Portillo	No	Yes	Yes	Worldwide	Big (10^7)	Unconstrained	Availability	Yes	Analytic	Adaptive GA

1.4.1 Single point designs

Giggenbach et al. [15] build their cloud dataset from the ISCCP dataset [33] and use a simulation approach to analyze the network availability for an Earth observation LEO satellite. However, they do not perform optimization over the design space for the locations of the OGSs in the network, but instead analyze two particular configurations. The first one comprises two independent networks of four OGSs located in Australia for which monthly availability results for a year are reported. Their calculations show a joint probability of coverage lower than 5% across all months. The second one is a study where a network of eight OGSs distributed across the globe serves a satellite flying in the ISS orbit. In this case, the data volume downloaded is reported.

In [44], one year of imagery from MTSAT is used to analyze six architectures with up to eight OGSs located in Japan. A mean availability of 94% is achieved for the case with eight OGSs, whereas 90% can be achieved with six OGSs. In addition

30

to the availability computations, an analysis of the distribution of the time between two passes over clear skies for a satellite in a 670-km Sun-synchronous orbit (SSO) is conducted.

Lacoste et al. [23] examine the data volume that several satellites in LEO (flying in SSO orbits with altitudes between 700 and 800 km) would be able to download to a network of six OGSs located in Western Europe. To determine the locations of the OGSs, a cloudiness analysis using three years of cloud data from Meteosat was conducted in collaboration with the French National Meteorological Agency. Results showed that, by using optical technology, the downloaded data volume increases by a factor of three.

In [32], the authors also use a simulation approach to determine the optimal location of a set of ground stations that act as feeder links for a network of high-throughput geostationary satellites. Two years of data from the Meteosat Cloud Mask dataset are used, and four different architectures are analyzed, each of them corresponding to a particular scenario of available locations. Their analysis focuses on European locations, and takes into account the distance to the optical backhaul network to estimate the ground segment cost. The optimization method employed consists of a greedy algorithm that iteratively selects the best OGS, assuming that all of the previously selected OGSs are unavailable, as described in [31].

1.4.2 Tradespace exploration

Link et al. [25] and Wojcik et al. [46] employ the Lasercom Network Optimization Tool (LNOT), a proprietary software simulation tool that uses a high resolution cloud database constructed using NOAA's GOES satellite imagery to determine the fraction of time that a cloud-free line of sight (CFLOS) path is available to a deep space probe. Both projects limit the number of possible locations to a list of facilities and frame the optimization problem as downselecting the subset of N OGSs that maximizes the network availability. Candidate locations in [25] are all within the US territory, whereas in [46] the list of possible locations is extended with stations located across the globe. In [3], an earlier study, the effect of site diversity for an optical network that

communicates with the (later scrapped) Mars Laser Communications Demonstration is analyzed. In their analysis, the authors include other factors that contribute to link outage such as aerosol attenuation, sky radiance and atmospheric seeing.

The Optical Link Group Study report [17] is a comprehensive report based on LNOT, and includes single point analysis for six different scenarios (LEO, HEO, GEO, L1, L2 and Deep Space). An availability of 94.8 % was reported for a network with seven OGSs serving LEO users, and an availability of 95 % was reported for a 3-OGSs network communicating to a single geostationary relay satellite located over the Atlantic region.

In [10], the authors analyze the availability for a GEO satellite communicating with a network of optical ground stations in the European-African region using five years of cloud data from Meteosat. Their analyses provide availability for a German, European and international network, using a candidate set of 22, 49, and 66 ground stations, respectively. To reduce the computational effort necessary to evaluate all the candidate locations, they develop a custom optimization algorithm that considers both single and joint cloud coverage statistics.

1.4.3   Analytical models

Perlot and Armengol [30] propose an analytical model to quantify the probability distribution for the network availability, assuming both a binary attenuation channel where cloud coverage causes link disruption and a continuous model where clouds introduce an attenuation over the signal that depends on their thickness.

Gharanjik et al. [14] use a similar model to the one proposed in [30] but assume a minimum of N networks must be available simultaneously to provide the required throughput using multiplexing. That is, an N + P scheme where N active ground stations are used to transmit and the remaining P idle ground stations are used for site diversity is considered. The paper discusses the number of OGSs required to achieve different levels of throughput.

Overall, this literature review reveals three aspects that previous work lacks and are of vital importance for the OGS network architecting process. First, all of the

previous studies focus on analyzing a predefined set of candidate OGS locations, which ranges from 8 to 66 locations. Second, most literature analyzes the availability of a network focusing on a particular region of the Earth. Third, none work has been done to develop cost models to analyze the trade-off between performance and cost. This thesis expand the previous analyses and covers this research gap by analyzing a worldwide unconstrained scenario and developing a cost model for the OGSs.

1.5 Specific problem statement

To identify the optical ground segment architecture(s) that better address the needs of future near-Earth space missions **by**:

1. Implementing a model that considers cloud coverage worldwide, and given the locations of the ground stations evaluates the network availability and cost

2. Exploring the architecture space defined by combinations of ground stations, presence of relay satellites in GEO and presence of ISL among them

using a variable chromosome length genetic algorithm.

1.6 Thesis overview

The remainder of this thesis is organized as follows:

Chapter 2 introduces the Optical Network Ground Segment Analyzer (ONGSA), a computational tool to assess the cost and availability of a particular OGS network. In particular, the assumptions and hypothesis that are the bases of the cloud model are presented, together with the procedure to compute the network availability and the cost model used by the tool. This chapter concludes by presenting the tradespace exploration and optimization algorithms built into ONGSA.

Chapter 3 presents the validation of the different models used by the tool. The cloud and availability models are validated against data from two cloud coverage datasets (ISCCP and EUMETSAT) different from those used to create and adjust

the models. For the availability model, the results from ONGSA are compared against the values reported in the literature. Lastly, the cost model is benchmarked with the cost values that appear in [17].

Chapter 4 describes the scenarios considered in this study and presents the results of employing ONGSA and analyzing the different trade-offs that appear in the architectural design space. First, a set of scenarios using existing assets from NASA and astronomical observatories is analyzed, and then, the analysis of the trade-offs between using existing facilities and building new OGS is presented.

Finally, Chapter 5 summarizes the findings and contributions of this thesis, identifies limitations and outlines future directions for research in this area.

Chapter 2

Optical Network Ground Segment Analyzer (ONGSA)

2.1 Introduction

This chapter describes the Optical Network Ground Segment Analyzer (ONGSA), a tool developed to compute the optimal location for a network of optical ground stations to maximize the availability of the system at the minimum cost. The chapter is structured as follows. First, an overview of the tool together with its inputs and outputs is provided. Next, the different models used by the tool are described. These include the cloud model, the cost model and the model to compute the network availability. Finally, the different optimization techniques used by the tool to determine the optimal architectures are presented.

2.2 Tool overview

ONGSA is an architectural tool developed to analyze the availability and cost of an optical space communication network. The tool is capable of enumerating thousands of ground segment architectures, evaluating them, and exploring the design-space using different optimization techniques. From a system architecture perspective, the tool covers the *representing*, *structuring* and *simulating* layers of the architecting

process, as described by Simmons in [40]. The viewing layer is covered by producing custom graphs and diagrams, but the tool does not incorporate a user interface to interact with it and explore the outputs produced.

Three decisions are available in the tool to encode architectures: 1) number and location of the optical ground stations, 2) presence of relay satellites in the GEO orbit and 3) use of inter-satellite links (ISL) among relay satellites. The candidate set of locations (existing or non-existing facilities) can be introduced as an array of latitude-longitude coordinates or as a binary mask of allowed locations using MODIS Climate Modeling Grid (CMG) as the reference grid. The number of relay satellites, as well as their orbital-slot positions (fixed slots vs. slot locations optimized for maximum availability) can be configured too. From a System Architecture Problem standpoint, as described in [38] by Selva, the first decision can be considered a down-selecting problem, whereas the second and third decisions are assigning problems.
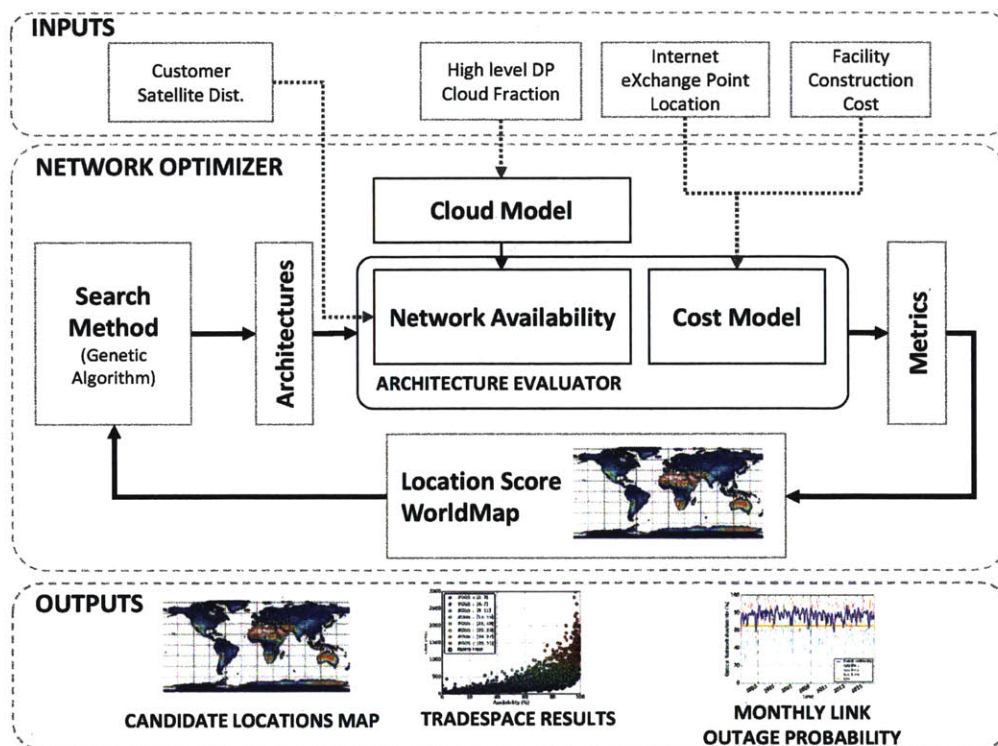
Figure 2-1: ONGSA overview.

Figure 2-1 shows the overall picture of the tool. The top block contains the main inputs to the models used by the architecture evaluator, whereas the bottom block contains the outputs produced by the tool. The block in the middle depicts the network optimizer, the central component of the tool.

ONGSA uses four main datasets as its inputs. On one hand, the cloud model is based on NASA's Earth Observations Cloud Fraction dataset[1], a high level data product which summarizes the fraction of time a certain location has cloudy skies every month. Using as inputs the cloud model, and the customer satellite distribution, the network availability is computed. On the other hand, the cost model uses the distance to the closest access network exchange point and the facility construction cost database [7] as its inputs.

The network optimizer is the main component of ONSGA. It is responsible for enumerating a set of architectures, evaluating them in terms of availability and cost, and if needed, iterating this process to improve the quality of the solutions obtained. It is composed of two main modules, a *search method* and an *architecture evaluator*. The search method is an algorithm that enumerates a set of architectures aiming to discover those that offer the best performance at the lowest cost. ONSGA has different search methods such as the *full enumerator* (useful when analyzing scenarios with a fixed set of candidate locations for the OGS), or the *variable length chromosome GA*. These methods are further discussed in Section 2.4. The set of architectures generated by the *search method* is evaluated by the *architecture evaluator*. This module computes the availability of an architecture using a probabilistic model and its cost using a parametric cost model. These models are described in detail in Section 2.3.

Finally, the tool produces three types of outputs. First, for each of the evaluated architectures, a detailed report of costs and network availability is generated. The cost report breaks down the costs on recurring and non-recurring costs. The monthly availability for each of the assets in the network (OGS and relay satellites if present) is computed. Second, the *Location Score WorldMap* is produced. The Location Score

---

[1]http://neo.sci.gsfc.nasa.gov/view.php?datasetId=MYDAL2_M_CLD_FR

37

WorldMap consists on a world map with a score assigned to any latitude-longitude point on Earth that indicates the goodness of that point as a location for a new OGS. Finally, a scatter plot where each point represents a different architecture in the bi-dimensional availability-cost space is produced for each of the iterations taken by the search method.

2.3 ONSGA Models

2.3.1 Cloud Model

The previous literature has used two different approaches to tackle cloud modeling for optical availability estimation. On one hand, a common method is the *simulation approach*, where past high-frequency satellite imagery is used to evaluate the availability of the network. On the other hand, the *analytic approach* uses a probabilistic cloud model, which assumes certain values for the cloud probabilities of each ground station and models the different temporal and spatial correlations among sites in the same network, to evaluate the network availability.

Most of the previous studies have used the simulation approach. In this approach, satellite imagery with a temporal resolution as low as 15 minutes is used to estimate the network availability of a set of OGSs. Due to the high temporal granularity of the data, the estimations of cloud coverage are highly accurate.

However, this approach has three drawbacks that make it unsuitable for tradespace exploration. First, since the complete dataset is too large, it cannot be loaded completely in RAM memory. Instead, data from every OGS needs to be loaded every time a candidate architecture is evaluated. This continuous loading process, in turn, slows down the execution time of the program, which prevents us from evaluating a large set of architectures. Second, as our analyses are conducted using a commodity laptop, there is a storage capacity constraint. This constraint imposes a limit on the timespan of the data that can be used in the analysis (the size of a year of worldwide 15-minute imagery data is roughly 3 Tb). Because of this limit, most of the previous

works use a timespan of one to two years for their analyses. Finally, certain datasets provide no cloud mask data products, and therefore the end-user needs to design his own algorithms to determine whether a cloud was present at the time the image was taken or not.

Because of the limitations exposed above, this work uses the analytical approach, better suited for tradespace exploration. This approach uses a probabilistic model to determine the probability of finding a ground station with clear skies so it can transmit at a certain point in time. A common formulation is to assume the channel to be an ON/OFF channel in which p_i refers to the probability of being in the OFF state (i.e., a cloud blocks the path from the spacecraft to the OGS). Mathematically, this channel is a random variable ($\mathcal{X}_i$) distributed according to a Bernoulli distribution.

$$\mathcal{X}_i \sim B\left(p_i\right) = \begin{cases} 1 & \text{w.p. } p_i \\ 0 & \text{w.p. } 1 - p_i \end{cases} \quad \forall i \in [1, N] \qquad (2.1)$$

To determine the availability of a satellite, a new random variable ($\mathcal{N}$) is defined. This random variable models the number of ground stations which are at the same time in the line of sight (LOS) to the satellite and available (present a clear sky for communication purposes). $\mathcal{N}$ is defined in Eq. 2.2.

$$\mathcal{N} = \sum_{i=1}^{N} \mathcal{X}_i \qquad (2.2)$$

$\mathcal{N}$ models the state of the network at any time. By knowing its probability density function (PDF) $f_N(\mathcal{N})$, the expected fraction of time that the system suffers link outages can be computed. In particular, the link outage probability (LOP) is defined as the probability that all the OGSs that are in the LOS with a satellite fail due to cloud coverage at the same time. Its value can be computed as:

$$\text{LOP} = f_N(N) = \mathcal{P}\left(\mathcal{N} = N\right) \qquad (2.3)$$

Previous analytical models use several hypotheses to approximate the PDF of $f_N(\mathcal{N})$.

39

In [30], the authors propose a simplified model where all the OGSs have identical cloud probabilities ($p = p_i = p_j \; \forall i, j$). In this situation $f_N(\mathcal{N})$ is simply the binomial distribution, and the LOP, as defined before, can be computed as:

$$\text{LOP} = p^N \tag{2.4}$$

In [11], Gagnon et al. remove the equal probability assumption, but still consider that the OGSs are uncorrelated. In that situation the PDF of $\mathcal{N}$ follows a Poisson binomial distribution and the LOP can still be easily computed as shown in Eq. 2.5.

$$\text{LOP} = \prod_{i=1}^{N} p_i \tag{2.5}$$

However, the premise of statistical independence is not valid when the distance between ground stations falls below a certain threshold [12], since weather conditions are tightly correlated in spatially close locations. In addition, it is clear that the cloud probability on each latitude longitude point is not stationary and it changes over different seasons and years. This contrasts with the formulation taken by the literature that uses analytical model, where no models mention the time dependence of these values.

Since these two factors have an important impact on the LOP, it is needed to develop a comprehensive analytical cloud model that accounts for both the temporal and the spatial correlation among cloud conditions in different regions. Moreover, the cloud model shall be simple enough to enable fast computation of the network availability. To accomplish this objective, two correlations models have been built. The next two sections discuss these correlation models.

Temporal correlation model and dataset selection

Since our cloud model will be used for tradespace exploration, it must be simple enough so that multiple architectures can be evaluated quickly. One of the conditions to meet this requirement is that the model does not depend on large volumes of data.

40

To reduce the amount of values used to describe the weather conditions, single binary observations (cloudy / clear sky) can be aggregate into the mean cloud probability over a certain period of time (T) (i.e., assume that the stochastic process that models the cloud coverage over a certain region is piecewise stationary during T consecutive time units).

The temporal correlation model has a double function. First, it determines the highest value that can be chosen for T (i.e., the value that minimizes the number of points required to compute the network availability) without losing information on the correlation among different ground stations. Second, this model determines how long the timespan analyzed must be so that the results of the analyses are general and are not biased by the particular atmospheric conditions of the timespan used to conduct them.
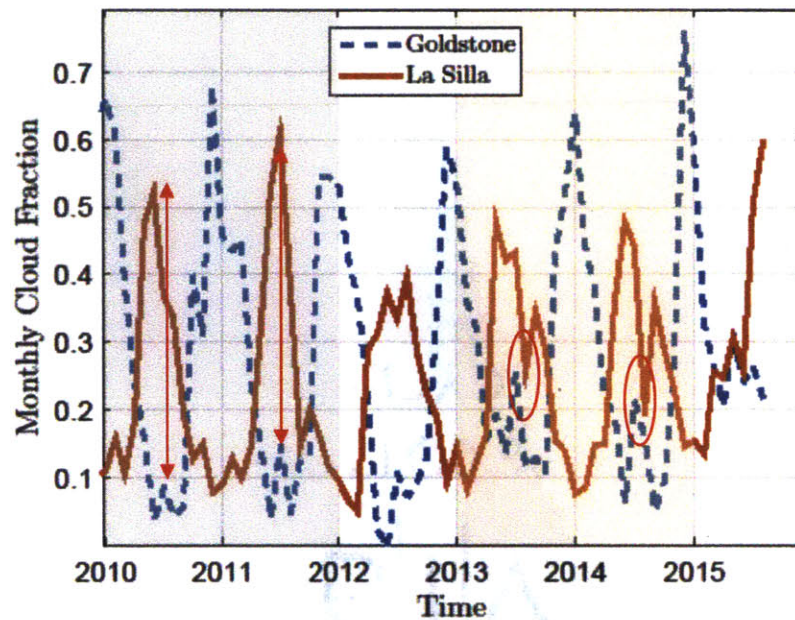
Figure 2-2: Monthly cloud fraction for La Silla and Goldstone from 2010 to 2015

As an example, Figure 2-2 depicts the monthly cloud fraction for two existing ground stations, Goldstone in California and La Silla in Chile. It is clear that both ground stations are negatively correlated. This happens because Goldstone is in the Northern Hemisphere and La Silla is in the Southern Hemisphere, so when one of

41

the stations is in the winter season (high cloud fraction), then the other one is in summer. It is clear that if T is chosen to be one year, part of the temporal correlation information would be lost. In addition, focusing on the two 2-year periods of 2010-2011 and 2013-2014, specifically in the months of July, it can be observed that the time series presents a very different behavior. In 2010-2011 the cloud fraction in Goldstone was much smaller than in La Silla, whereas in 2013-2014 both values were almost the same.

An exploratory analysis showed that the variability of the results when considering less than four years of data is very high. Figure 2-3 shows a histogram of the difference on the availability for 10,000 architectures when computing the network availability (as described in Section 2.3.3) for the years 2005-2006 and 2010-2011. The average of the absolute value of the difference (as a percentage of the real availability value) is 9.86 %. For some specific architectures this value is greater than 40%.
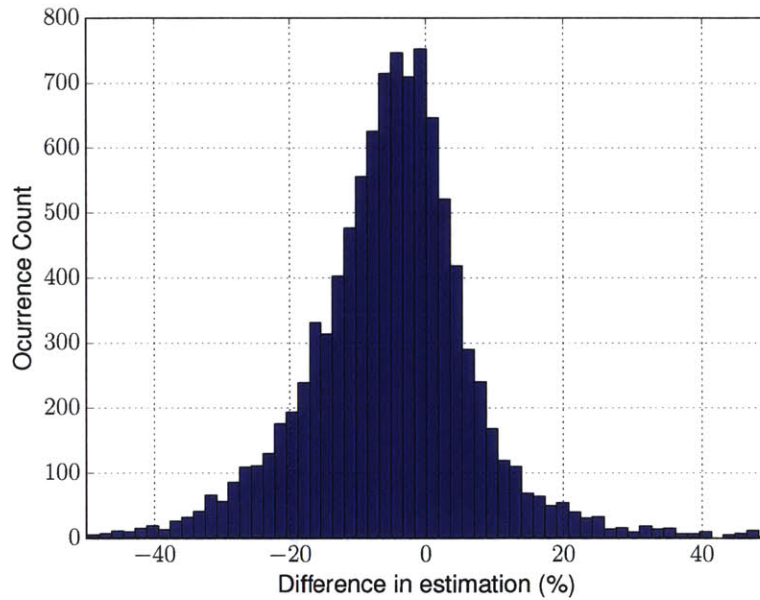
Figure 2-3: Histogram of differences computed as $\frac{A_{05-06} - A_{10-11}}{A_{02-15}} \cdot 100$

This information plays an important role when choosing the dataset that will be used to model the cloud conditions on our analyses. Different datasets trade coverage, spatial resolution, frequency of observations, and length of the observa-

tions. These datasets are normally provided by meteorological agencies such as the National Oceanic and Atmospheric Administration (NOAA), the European Meteorological Satellites (EUMETSAT), or independent projects like the International Satellite Cloud Climatology Project (ISCCP). Table 2.1 contains a summary of the characteristics of the datasets considered.

Table 2.1: Characteristics of different cloud datasets

	MODIS	ISCCP	EUMETSAT	GOES	FENGYUN	Himimawari
Coverage region	Global	Global	Europe Africa	America	S. East Asia Oceania	East Asia Oceania
Frequency of observations	1 day, 8 days, 1 month	3 hours	15 minutes	15 minutes	15 minutes	15 min
Spatial resolution	0.1 deg	2.5 deg	< 0.1 deg	< 0.1 deg	< 0.1 deg	< 0.1 deg
Cloud fraction data product	Yes	Yes	No	No	No	No
Cloud mask data product	No	No	Yes	No	Yes	Yes
Timespan	2002-Present	1983-2009	2006-Present	-Present	2014-Present	-Present
Publicly available	Yes	Yes	Yes	Yes	Yes	No

Given the information in Table 2.1, MODIS was chosen as the source dataset to represent the cloud conditions in our analyses. This decision was based on the following criteria. First, MODIS is a dataset that offers global coverage. Therefore, it is not necessary to assemble a world-wide model using multiple datasets from different sources. Second, MODIS provides the cloud fraction (i.e., cloud probability) for each point, and therefore there is no need for further pre-processing of the data. Third, MODIS offers a long enough timespan to have significant results. Finally, the spatial resolution of MODIS is high enough to capture the different cloud conditions in different regions of the globe.

The frequency of the observations considered remains to be determined; in other words, what value of T is going to be used. The analyses conducted by Sanchez in [35]

43

showed that there is a value of T that minimizes the estimator error and variance. In turn, he showed that this value is close to 35 days. Therefore, among the three MODIS data products available for the cloud fraction dataset (daily, 8-days, monthly), the monthly one was chosen. Finally, to reduce the magnitude of these errors and capture as many situations as possible, the longest period of time available in any dataset at the time the data was gathered, which was 186 months from February 2002 to August 2015, was used.

Figure 2-4 contains a pictorial representation of August 2015 from the EOS Cloud Fraction data product from NASA's satellites Terra and Aqua.
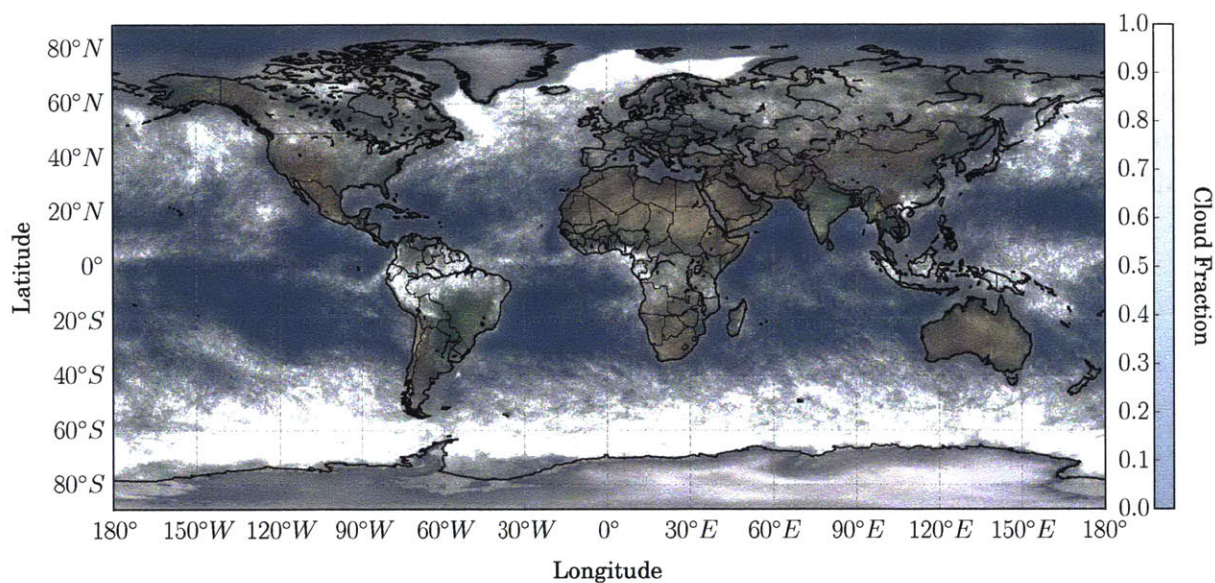
Figure 2-4: Worldmap of cloud fraction values from MODIS dataset for August 2015

Spatial correlation model

Assuming statistical independence when in reality the ground stations are correlated can yield erroneous results, as described in [30]. To avoid this risk, the effects of

spatial correlation need to be included in our calculations. In [30] the authors propose sampling-based techniques to simulate the real behavior of the correlated random processes. However, these techniques are computationally expensive and unsuited for architectural studies, as the LOP for each architecture must be computed thousands of times, drawing different cloud probability-values for every computation.

A more computationally affordable procedure is described in [12], where the spatial distribution of clouds is characterized analytically by fitting an exponential model to real data gathered every six hours for five years in 33 different locations in Spain. In particular, they describe the statistical dependence index as the ratio between the real joint probability $\mathbf{P}(A \cap B)$ and the product of the marginal probabilities $\mathbf{P}(A), \mathbf{P}(B)$, as shown in Eq. 2.6.

$$\mathbf{P}(A \cap B) = \chi_{A,B} \mathbf{P}(A)\mathbf{P}(B) \tag{2.6}$$

where A and B refer to the events "*Clouds over the OGS$_x$*", $x \in \{A, B\}$ and $\chi_{A,B}$ is the statistical dependence index.

As our model extends to the whole globe, we replicate the results from [12] using a dataset of 4,000 sites in the US, South America, Australia, Europe and Southeastern Asia. These data were downloaded from NOAA's National Climatic Data Center (NNDC) DS3505 dataset, which contains information on the cloud coverage status every 20 minutes.

Cloud coverage information in NNDC is represented by the number of oktas of the sky which are covered. The bulk data is pre-processed to remove those ground stations with insufficient values, or those whose registers are not reliable. Next, the values for $\mathbf{P}(A \cap B), \mathbf{P}(A), \mathbf{P}(B)$ and $\chi_{A,B}$ are computed for every pair of ground stations, and an exponential model is adjusted to the data using the distance, latitude and longitude of each of the ground stations as independent variables. None of the coefficients were significant apart from the distance between ground stations. Eq. 2.7 presents the resulting model, whereas Fig. 2-5 shows how the adjusted model fits the

data points.

$$\chi_{A,B} = \alpha_0 + \alpha_1 \exp\left(-\frac{d}{d_0}\right) = 0.98 + 0.71 \exp\left(-\frac{d}{424.1}\right) \tag{2.7}$$
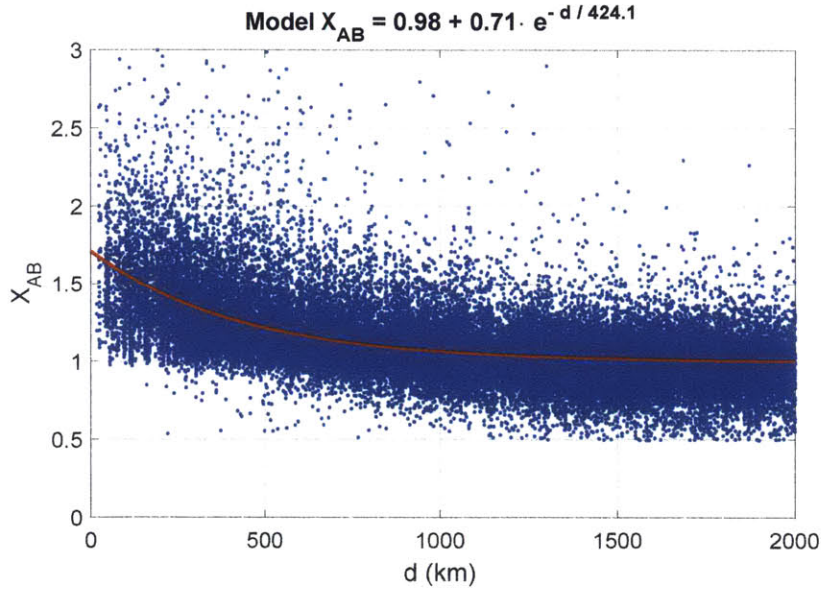
Figure 2-5: Statistical dependence index ($\chi_{A,B}$) against distance between pairs of ground stations.

Note that our model presents a similar cloud correlation distance (d_0 in Eq. 2.7) to the one provided in the model derived in [12]. Note that the model error presents a decreasing variance (or range of truth values) as d increases (i.e., the range of the blue dots, which correspond to observations of the statistical dependence index, decreases with d). This happens due to the formulation of the model, since the range of possible values for $\chi_{A,B}$ is bigger for d small than for d big. For example, consider two ground stations (A and B) located at the same position. As they are at the same position, $\mathbf{P}(A) = \mathbf{P}(B)$, and $\mathbf{P}(A \cap B) = \mathbf{P}(A)$. Therefore, as $\mathbf{P}(A \cap B) = \chi_{A,B}\mathbf{P}(A)\mathbf{P}(B)$, then $\chi_{A,B} = \frac{1}{\mathbf{P}(A)}$. In this situation, the range of $\chi_{A,B}$ can go from 1 (for $\mathbf{P}(A) = 1$) to ∞ (for $\mathbf{P}(A) = 0$), while our model approximates it as a constant ($\chi_{A,B} = 1.59$ for $d = 0$). In contrast, for larger values of d the OGSs A and B are more likely to be

uncorrelated, and therefore the value of $\chi_{A,B}$ trends to be close to 1.

Even in this latter case, the real values of the statistical dependence index show a high dispersion with respect to the values obtained from the fitted model. This is due to the difficulty of such a simple exponential regression model to fit all the different correlation situations between close ground stations. The root mean-square error between the estimates and the actual data is 0.084. This model is further validated in Section 3.2, using a dataset different to the one used to adjust it.

Finally, the spatial cloud model described has several limitations that need additional considerations. First, only architectures where ground stations are at most pairwise spatially correlated can be evaluated. Only these situations (by filtering out those architectures that do not satisfy this constraint) are considered for the analyses in Chapter 4. Second, our model does not capture other temporal correlations apart from the seasonal correlation. This includes, for example, the correlations due to day-night effects, the jet-stream effects, or the effects that different type and opacity of clouds have on the link budget. Even though most of these cases represent second order effects, when looking at the statistical "tails" corresponding to very high availabilities they might dominate. Quantifying the effect of these correlations is one point that needs to be addressed in future work (See Section 5.4).

2.3.2 Cost model

The goal of the cost model module is to come up with an estimation of the lifecycle cost of a ground segment architecture good enough for relative comparison across architectures. The cost of an architecture is the sum of the costs of each of the OGSs that compose it. At the same time, the OGS cost is split into non-recurring investment costs and recurring operational costs. The drivers of the recurring costs are wide area communication operational costs, and reparation and maintenance of the facility costs. The drivers of the non-recurring costs are site construction, optical terminal cost, and wide area communication network development costs.

This section describes the equations to estimate each of these components costs. These values are compared to those that appear in the previous literature in Section

3.4. All the monetary values in the cost model are expressed in FY2015$k.

Non recurring cost

The main drivers of the non-recurring cost are site construction, optical terminal cost, and wide area communication network development. This costs are only incurred once, when the ground station is built. This subsection describes the parametric model for each of the aforementioned costs.

Estimating the cost of a single terrestrial optical terminal has been analyzed in references [36], [42], [13], [41]. Even though the vast majority of the existing models relate the cost of a telescope to a single variable, its diameter, some authors in the literature present multivariate cost models that include other parameters such as the year of development, TRL, or the number of segments [41]. There is a general agreement among these papers that the cost of a telescope scales as αD^β; the value of α has decreased with time, as manufacturing has become cheaper, whereas β has remained constant (and with unanimous agreement about its value) in time. For monolithic telescopes, most references provide a model where the cost is proportional to the diameter of the telescope to the power of 2.6 [24], [36] or 2.7 [2], [42] ($\beta = 2.6$, $\beta = 2.7$)). The values of the cost estimation ratios (CERs) used in the model are presented in Eq. 2.8. This model is valid for small telescopes with a diameter smaller than 1.5 m, which is always the case in our analysis.

$$C_{tels} = 6,230 \; \$k \; D_{\text{tel}}^{2.7} \qquad \text{if} \quad D_{\text{tel}} \le 1.5m \qquad (2.8)$$

On the other hand, the site construction cost is estimated using a parametric model from the DoD Facilities Pricing Guide [7]. The model uses a unit cost per square meter ($\$/m^2$) for each type of facility which is multiplied by a) the dimensions of the facility and b) the *area cost factor* which accounts for differences in labor, materials and equipment in different geographic locations. The construction cost is computed

as

$$C_{cons} = F(L) \cdot U_c \cdot A_{gs} \tag{2.9}$$

where $F(L)$ is the area cost factor, U_c is the unit construction cost, and A_{gs} are the dimensions of the facility (estimated to be 1780 m^2).

Finally, the WAN communication investment is modeled to be proportional to the distance from the ground station to the closest Internet exchange point (IXP). This cost-term intends to capture the costs associated to establishing a high-bandwidth wide area network cable from the ground station to a transport network access point. The CER for the WAN cost is presented in Eq. 2.10, where the value of 15.9 k\$ is obtained as the higher cost of the fiber optic cable installation estimated for the year 2013 by the U.S. Department of Transportation [29]

$$C_{WAN,nr} = 15.9\text{k\$} \cdot d_{\text{IXP}} \tag{2.10}$$

where d_{IXP} is the distance to the closest IXP. The locations of the IXP across the globe were obtained from the European Internet Exchange Association[2] database that contains 513 entries.

All in all, the construction cost is computed as

$$C_{nr} = F(L)(C_{WAN,nr} + C_{cons} + C_{tels}) \tag{2.11}$$

where F(L) is the cost area factor for a ground station located in country L. Figure 2-6 presents a world-map with the non-recurring cost for each latitude-longitude point.

---

[2]European Internet Exchange Association https://www.euro-ix.net/
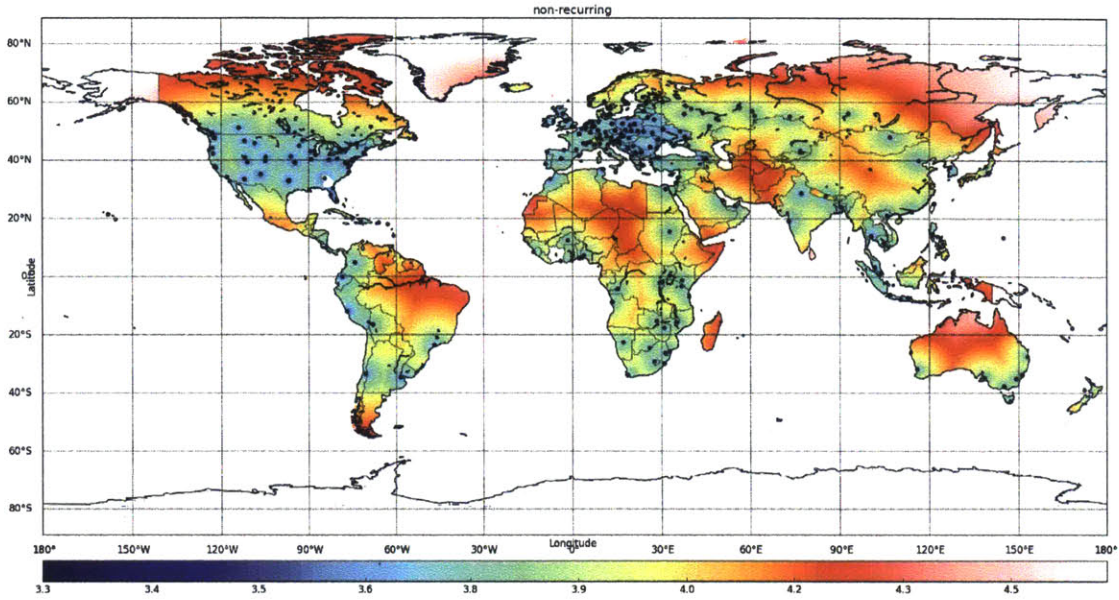
Figure 2-6: World-map of non-recurring cost (in M$, FY2015) for a new OGS. Black markers denote the position of an Internet exchange point (IXP).

Recurring cost

Our cost model assesses the recurring cost of a ground station as the sum of two different components: operational costs of the WAN, and maintenance and operational cost of the facility and the telescope.

First, the WAN operational cost $(C_{\text{WAN},r})$ is estimated to be 390 k$ per year, as indicated in the Networx Unit Pricer[3], the US General Services Administration costing information guide for domestic and international network services for federal agencies.

Second, the maintenance and operational costs are given by the sustainment cost (as described in [7]) multiplied by the sustainment cost factor (which again depends on the country the facility is located on) and the dimensions of the facility.

$$C_{M\&O} = S(L) \cdot U_s \cdot A_{gs} \tag{2.12}$$

---

[3]https://releasedprices.networx.gov/

where S(L) is the sustainment cost factor in country L, U_s is the unit sustainment cost, and A_{gs} are the dimensions of the facility.

All the terms in the non-recurring cost are multiplied by the *inflation factor* as described in [7], which accounts for the future-year inflation, and escalation costs for operations and maintenance. In turn, the total recurring cost (C_r) is given by Eq. 2.13

$$C_r = \sum_{t=1}^{T} \frac{C_{\text{WAN},r} + C_{M\&O}}{(1 + I(r))^t} \qquad (2.13)$$

where $I(r)$ is the inflation factor, T is the lifetime of the ground stations (set to 30 years in our analysis), and t is an index that designates the difference between the year in which the recurring costs is incurred and the initial year (2015).

2.3.3 Network availability model

As the cloud model is discretized in time using months as the time unit (see Section 2.3.1), first the monthly network availability (NA_m) is computed. The monthly network availability is the probability that a satellite in a random orbit has at least one ground station in cloud-free line of sight (CFLOS) at any point in time of month m. The monthly link outage probability (LOP_m) is defined as the complement of the monthly network availability (NA_m) as denoted in Eq. 2.14. Finally, the network availability (NA) is defined as the percentile 5 of the time series of monthly network availabilities. Note that this definition of NA differs from the traditional metric used to measure the network availability, which is the mean value of the time series. The rationale behind the choice of the 5 percentile is that it accounts for sudden drops of the availability in particular months, which can extremely harm the data volume returned by certain short-term missions.

$$NA_m = 1 - LOP_m \qquad (2.14)$$

The availability of a given network of OGSs is computed using the following four step procedure.

First, for each optical ground station (OGS_i) a mask (M_{gs_i}) that indicates which points at a given height (h) will be in line of sight with the ground station is computed. For that purpose, a 1° resolution (both in latitude and longitude) spherical grid with radius $R_E + h$ (R_E is the radius of the Earth), concentric to the Earth, is defined. Then, the set of points of the grid whose elevation angle is above the minimum elevation angle admissible for the receiver ground station is computed. The elevation angle between a point of the grid (P) and a particular OGS can be computed using Eq. 2.16, 2.17

$$M_{gs_i} = \{P = (L_P, l_P) | \epsilon(P) > \epsilon_{min}\} \tag{2.15}$$

$$\epsilon(P) = \arccos \frac{sin\gamma}{\sqrt{1 + \frac{R_E}{R_E+h}^2 - 2\frac{R_E}{R_E+h}\cos\gamma}} \tag{2.16}$$

$$\cos(\gamma) = \sin L_P \sin L_{OGS} + \cos L_P \cos L_{OGS} \cos(l_P - l_{OGS}) \tag{2.17}$$

where L_{OGS} and l_{OGS} are the latitude and longitude coordinates of the OGSs, L_P and l_P are the latitude and longitude coordinates of the point i of the spherical grid, h is the height at which the spherical grid is located and ϵ_{min} is the minimum elevation angle in order to establish a successful communication link. In this work $\epsilon_{min} = 20°$ following the guidelines of [46].

Second, the LOP_P for each point of the mask is determined by computing on which point the optical beam will pierce the cloud layer (estimated being at a height of 12 km.). In addition, some orbits are more popular than others, so the probability of a satellite being in LOS with a OGS is not uniform among all points of the mask. In order to account for this effect, the satellite density over the Earth surface (i.e., over which latitude-longitude points of the Earth's surface is more likely to find a satellite with its Nadir pointing towards that point) is computed.

52
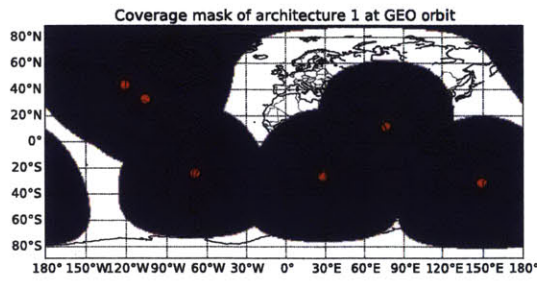
(a) Step 1 - Determine the coverage mask at GEO
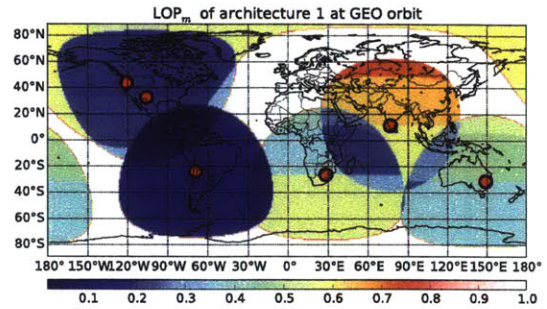
(b) Step 2 - Determine the LOP_m for each point of GEO
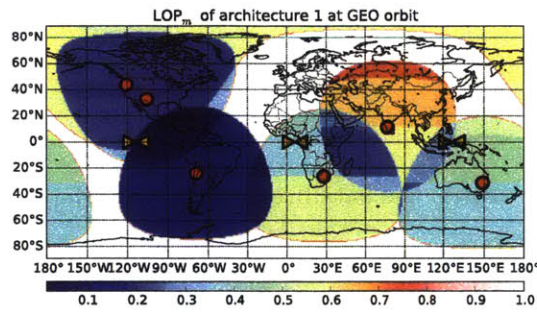
(c) Step 3 - Detrermine the Location of the satellites (marked in orange)
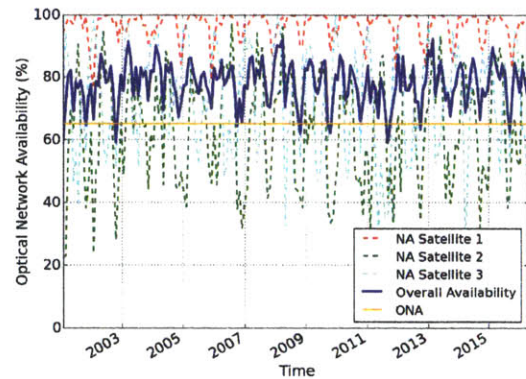
(d) Step 4 - Compute the Optical Network Availability for each satellite and the whole network

Figure 2-7: Procedure to compute NA_m

For that purpose, an STK[4] scenario is created with all the active satellites in LEO whose mission belongs to one of the following categories:scientific, Earth observation, weather, human space flight, or technology demonstrator. Then, their orbits are propagated and their latitude-longitude coordinates (discretized to a 0.1 degree resolution) are registered for a period of a year (10 second time-step). Finally the probability of having a satellite whose nadir intersects every point of the globe is computed using a frequentist approach. The 3600×1800 matrix whose values indicate the probability of having a satellite over point P is denoted as $S(P)$. These results are plotted in Fig.

___
[4] AGI's Systems ToolKit http://www.agi.com/products/stk/
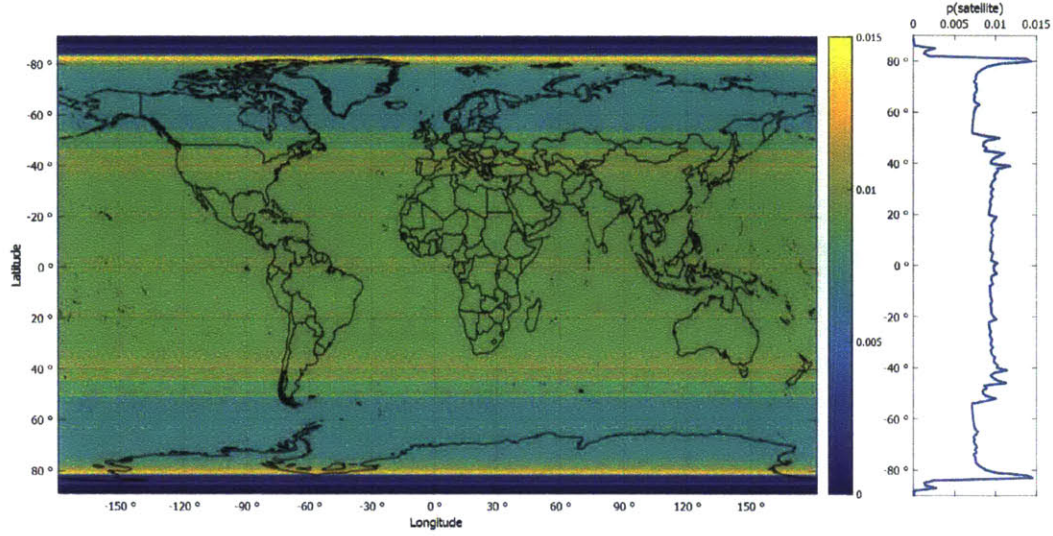
Figure 2-8: Satellite density over the surface of Earth.

2-8. Note that due to the precession of the orbits, the satellite density only depends of the latitude of the point (plotted in the left graph).

Third, in case the scenario has relay satellites, their optimal locations are determined. In some of the scenarios, one of the assumptions is that a set of three satellites in GEO is available to relay the communications of the LEO satellites to/from an OGS. This system is similar to TDRSS configuration [45]. However, it is assumed that the orbital slots where the relay satellites are located are not predefined but optimized for every OGS network architecture.

Finding the optimal slots for the relay satellites can be formulated as a mathematical optimization problem described by Eq. 2.18.

$$
L^*(s_i) \quad = \quad \arg\max_{L(s_i)} \text{Per}_5 \left[\text{NA}(L(S), \text{OGS})_m \right] \tag{2.18}
$$

$$
s.t.
$$

$$
110 \quad \leq |L(s_i) - L(s_j)| \leq 130 \qquad \forall i, j, \quad i \neq j
$$

$$
L(s_i) \quad \in [-180, 180]
$$

where $\text{Per}_5[\cdot]$ stands for the percentile 5%, $L(s_i)$ denotes the orbital slot of the relay

satellite i, and $\text{NA}(L(S), \text{OGS})_m$ is a function that computes the monthly network availability at month m given the location of the satellites and the set of OGSs that compose the architecture. Note that the first constraint enforces that satellites are evenly spaced in the geostationary orbit.

In this study two forms for the availability function $\text{NA}(L(S), \text{OGS})$ are considered, depending on whether the relay satellites have cross-link capabilities or not.

Fourth, once the optimal location of the relay satellites has been determined, the actual NA for the architecture is computed. The next subsections describe how the NA is computed for different scenarios.

Results of steps 1-4 for a test architecture with three optical relay satellites without ISL among them, and six OGSs in Chile, Australia, India, the Canary Islands and the USA (2) can be observed in Figure 2-7.

Availability for GEO relay satellites

As previously mentioned, the network availability is defined as $\text{NA} = \text{Per}_5[\text{NA}_m]$. The monthly network availability (NA_m) can be computed from the monthly link outage probability (LOP_m), as one is the complement of the other (see Eq. 2.14). A first step to compute the NA_m is to compute the LOP_m at a certain point P. Let the set $\{\text{OGS}_P\}$ be the set of optical ground stations in direct visibility with a satellite located in point P and $C(\text{gs})$ be the event "it is cloudy over the optical ground station gs" for gs $\in \text{OGS}_P$. Then, the probability that the satellite cannot communicate back with any of the OGSs is given by:

$$\text{LOP}_{P,m} = P\left(\bigcap_{i=1}^{N} C(\text{gs}_i)\right) \qquad \forall \text{gs} \in \text{gs}_P \qquad (2.19)$$

$P(\bigcap_{i=1}^{N} C(\text{gs}_i))$ can be computed as the product of the individual cloud probabilities $P(C(\text{gs}_i))$ for those ground stations that are statistically independent, and using Eq. 2.6 for those who are pairwise spatially correlated. It's easy to see that this formulation derives erroneous results if more than two ground stations are correlated, as only pairwise correlations can be assessed. To avoid erroneous values, the tool checks

on the ground station selection procedure (previous to the availability computation) that no more than two ground stations are correlated in a valid architecture. For example, imagine a situation where an OGS (A) is simultaneously spatially correlated to two other OGSs (B and C). Then, the spatial correlation model would allow us to compute $\mathbf{P}(A \cap B)$ and $\mathbf{P}(A \cap C)$, but no $\mathbf{P}(A \cap B \cap C)$. Because of that, those architectures where this situation is present are automatically discarded from the analysis. Currently, this is one of the limitations of the tool. Sections 5.3 and 5.4 describe some alternatives to the spatial correlation model that would enable the evaluation of this type of scenarios.

Now, in the scenario in which the three relay satellites can communicate among them using their cross-links, the monthly network LOP is equal to the probability that none of the relay satellites can communicate with any of the ground stations with which they are in line of sight. The NA_m is then the complement of the product of the individual LOPs for each satellite s_i, $i = \{1, 2, 3\}$

$$\mathrm{NA}(L(S), \mathrm{OGS})_m = 1 - \prod_{i=1}^{3} \mathrm{LOP}_{L(s_i), m} \qquad (2.20)$$

where $L(s_i)$ refers to the point in space where satellite i is located, and can be computed using Eq. 2.19.

On the other hand, if the relay satellites do not have ISL, then the NA_m is computed using the following procedure

$$\mathrm{NA}(L(S), \mathrm{OGS})_m = \left(1 - \sum_{p \in M_{s_i}} S(p) \mathrm{LOP}_{L(s_i), m} \right) \qquad (2.21)$$

where $S(p)$ is the satellite density matrix (see Figure 2-8).

Availability for LEO satellites using Direct to Earth downlink

Another plausible scenario for optical communications is one where satellites down-link their data directly to the OGSs. In this case the network monthly LOP can be computed by simply multiplying the LOP for each point of the sphere with radius

equal to $R_E + 600km$ (the sphere that contains all the possible circular orbits with height 600 km) by the satellite density matrix $S(p)$ and aggregating over all the possible points p. The monthly NA is its complement as described in Eq. 2.22.

$$\text{NA}(L(S), \text{OGS})_m = \left(1 - \sum_{p \in P} S(p) \text{LOP}_{p,m} \right) \tag{2.22}$$

where p denotes one point of the grid, $S(\cdot)$ is the satellite density matrix, and LOP_p is the link outage probability of point p.

2.4 Optimization Engine

Once the objectives of the study have been defined, our problem needs to be translated into a mathematical formulation. There are mainly two kinds of scenarios to analyze: those where there is a finite set of candidate OGSs, and those that consider unconstrained optimization over the entire surface of the Earth. In other words, find the best locations to place new OGSs (or use existing infrastructure) so that a certain value of NA is achieved at the minimum cost. These two situations, even similar from a conceptual standpoint, have very different implications from an optimization perspective; the complexity of the first case is bounded by $2^{|S|}$ (where $|S|$ is the cardinality of the candidate OGSs set), whereas in the unconstrained scenario this complexity is orders of magnitude larger as the amount of points to consider is significantly larger.

As a result, different optimization methodologies to find the best architectural options are required. This section describes the two methods implemented within ONSGA to solve the two situations described above.

2.4.1 Fixed set of candidate locations

This section describes the optimization technique used to solve the problem in which a fixed set of candidate locations for the optical ground stations is considered. Each architecture is comprised of a subset of these OGSs. The problem of choosing the

57

best architectures can be framed as a down-selecting problem [39], where subsets of k OGSs are chosen out of the N candidate locations so that the value (NA at a certain cost) delivered by the network is maximized. This formulation results in a total number of possible architectures to be considered equal to $\sum_{k=1}^{N} \binom{N}{k} = 2^N$.

This number, in general, is too large to perform a full factorial evaluation. Thus, heuristic techniques are used to solve our problem. ONGSA uses a genetic algorithm (GA), (i.e., a population-based meta-heuristic optimization algorithm), to look for the solutions in the Pareto Front. The GA implemented follows the prescriptions of the Non-dominated Sorting Genetic Algorithm-II (NSGA-II), a multi-objective genetic algorithm [6].

NSGA-II operates as follows. Initially, a random population of N architectures is generated and evaluated. Next, $\frac{N}{2}$ architectures are selected to act as parents for the following generation using the following criteria [6]:

- Architectures with lower Pareto ranking are selected first.

- Among those architectures with similar Pareto ranking, those with a lower crowding distance are selected first. The crowding distance is a measure of the closeness to other solutions with similar Pareto ranking for a particular architecture (i.e., a measure of the density of Pareto solutions around a particular architecture). Reference [6] describes the procedure to compute the crowding distance of a point in the Pareto Front. NSGA-II prioritizes the selection of architectures in low-density regions of the Pareto Front.

Then, two genetic operators are applied to the selected parents to produce $\frac{N}{2}$ offspring. ONGSA implements two genetic operators, *crossover* and *mutation*.

Crossover acts first, takes as inputs two parents selected at random (the father and the mother), and produces two offspring (a son and a daughter). Each architecture is represented using a $|S|$-length bit-string (b), where $b[i] = 1$ means that the $i-th$ OGS is part of the architecture. Uniform crossover ([43]) is applied to the two bit-strings representing the father and the mother architectures. In uniform crossover initially the son takes his bits from the father and the daughter takes them from her mother.

Then, each bit is swapped between son and daughter with probability 0.5. In total, applying crossover to a set of $\frac{N}{2}$ parents produces $\frac{N}{2}$ new offspring, which together conform a new generation of N architectures.

Mutation is a genetic operator applied with probability p_{mut} to all the parents and offspring produced by crossover. If mutation is applied to an architecture, a random OGS is removed from the architecture with probability p_{remove}. Then, independently of the outcome of this first step, a new OGS is added with probability p_{add}.

After both operators have been applied, the new generation is evaluated. The process repeats until a termination criterion (i.e., maximum number of generations G_{max} evaluated, no new architectures in the Pareto Front) is met. The by-default setup of parameters for our GA is $N = 20,000$, $G_{max} = 25$, $p_{mut} = 0.1$, $p_{add} = p_{remove} = 0.5$.

2.4.2 Unconstrained Optimization

The unconstrained scenario is various orders of magnitude more complex than the fixed set of candidate locations one. This complexity is due to the enormous number of possible architectures that result from considering any point on Earth as a potential locations for an OGS. To effectively determine which regions of the Earth offer favorable conditions to place optical facilities, a variable length chromosome genetic algorithm was implemented. This section describes the algorithm used by ONSGA to solve an unconstrained optimization problem.

Variable length chromosome genetic algorithms (VLC-GA) are an enhanced version of the Simple Genetic Algorithm developed by Holland in [20]. VLC-GAs have been used in the context of topology optimization [22], pixel classification [27], or genetic planning [4]. The main difference of a VLC-GA with respect to a GA is that the latter uses a fixed length chromosome (i.e.: variable that encodes an architecture) whereas the former progressively increases the chromosome length as the optimization process progresses.

VLC-GAs are especially useful for some types of optimization problems in which the finesse of the solution depends on the length of the chromosome. However, it is

normally difficult to know a priori the optimal length of the chromosome, and using a uniform mapping might increase the computational burden of the optimization engine [22]. A VLC-GA can be obtained so that in initial stages of the optimization problem, a coarse solution is obtained, and later steps progressively refine it to obtain finer solutions. This idea of progressive refinement fits the unconstrained optimization problem formulation; first, coarse regions where good locations are identified, and then, the extent of these regions is further refined in subsequent steps.

The VLC-GA implemented in ONSGA proceeds as follows:

1. Divide the world map in 2.5 x 2.5 degree (latitude x longitude) regions. Delete those regions that only comprise sea-point inside them. The chromosome length for this iteration step equals the number of remaining regions ($|R|$). Note that these regions are not equal-area regions.

2. Sample N architectures randomly (or using an a priori probability density function) determining in which regions there will be an OGS. This information is encoded using a bit-string binary vector of length $|R|$. For each region where there is an OGS, select its location randomly in a land-point inside the region.

3. Evaluate the N architectures using ONSGA and compute the network availability and cost of each of them.

4. For each region, compute the average Pareto-ranking of the architectures with at least one OGS in them.

5. For the R_{top} top average Pareto-ranking regions, divide them in four new regions. Merge the R_{bottom} pairs of adjacent regions with the lowest average Pareto-rankings. The new number of regions $|R_{t+1}| = |R_{(t)}|(1 + 4R_{top} - R_{bottom})$.

6. For each architecture, build a new chromosome of length $|R_{t+1}|$ where the i-th bit indicates whether the architecture has an OGS in the i-th region or not.

7. Apply the genetic operators: use the NSGA-II algorithm and the crossover and mutation algorithms as described in Section 2.4.1 to produce a new population

of architectures.

8. Go to step 3 and iterate until the convergence criteria is met.

Figure 2-9 contains a block diagram of the algorithm. Note that the algorithms starts with a coarse division in regions of the Earth, and that certain areas get subsequently refined as the optimization process progresses over time. As the algorithm advances, the smaller a region is, the higher density of OGSs on that particular region, since refined areas correspond to good regions for placing a new OGS.
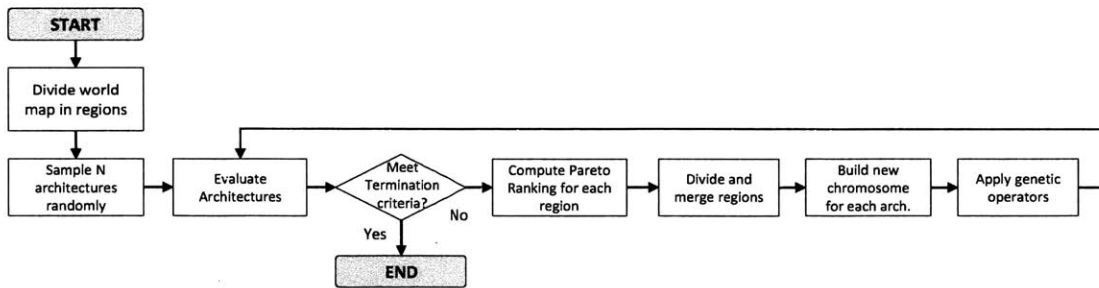
Figure 2-9: Block diagram for the VLC-GA algorithm

In order for the algorithm to operate correctly, is necessary to have a large population size. The by-default set-up of parameters of the algorithm is $N = 200,000$, $R_{top} = 10\%$, $R_{bottom} = 10\%$ and $R = 8000$. In addition, none of the regions can be sub-divided more than four times (that is, the minimum size of a region is 0.16 degrees), and historical information of the performance of previous populations is used to compute statistics for each region.

THIS PAGE INTENTIONALLY LEFT BLANK

Chapter 3

Tool validation

3.1 Introduction

Chapter 2 presented ONGSA, a tool to analyze the availability-cost tradespace of different ground-segment architectures for space optical communications networks. The tool is composed of three main modules, namely the cloud model, the availability model, and the cost model. This chapter devotes its attention to the validation process carried out for the different models of the tool.

The rest of the chapter describes and analyzes the benchmarks used to 1) evaluate the goodness of the results produced, and 2) understand the limitations and errors caused by the assumptions and simplifications made during the modeling phase.

First, the cloud model is compared against two publicly available cloud datasets: ESA's EUMETSAT Cloud Mask Data and the International Satellite Cloud Climatology Project (ISCCP) Gridded Cloud Product, to assess the error in the monthly average cloud fraction and the error obtained using the spatial correlation coefficient index.

Second, the procedure to compute the availability of a complete network of OGSs is validated. For that purpose, the results obtained using ONGSA and different datasets are compared. In addition, several analyses from the previous literature are replicated and their results are compared to those obtained using ONGSA. The objective of this analysis is double: first, to understand the magnitude of the error produced by

ONGSA when analyzing the tradespaces produced; second, to understand the validity and methodologies of previous studies.

Finally, the cost estimates reported by the cost model of ONGSA are compared to publicly available data in the Optical Link Study Group Final Report [17]. Due to the scarcity of public cost information on space assets, it is difficult to perform further statistical analysis to validate the model.

3.2 Cloud model validation

3.2.1 Methodology

The outline of the methodology to validate the cloud model described in Section 2.3.1 can be broken into three main parts; first, downloading and formatting the datasets from different climate monitoring agencies; second, defining the metrics used to compare the data; and third, comparing both qualitatively and quantitatively the data obtained by using different datasets. More explicitly, four steps occur in total:

1. Download the ISCCP D1 dataset and EUMETSAT's MGC dataset

2. Format datasets so that all the values are expressed using the Climate Modeling Grid as the reference system

3. Define the metrics used on each of the case studies proposed.

4. Analyze both quantitatively and qualitatively the differences between results and extract conclusions.

3.2.2 Dataset description

There are multiple satellite imagery data banks that contain data products as well as raw images that can be further processed to gain knowledge about cloud conditions over specific regions of the world. For example, for regions located in America, the National Oceanic and Atmospheric Administration (NOAA) Geostationary Satellite

Server contains a database of images from the GOES satellites that can be processed to determine the cloudiness of a specific area [46]; for regions in Europe, EUMETSAT's data center has an archive of imagery and data products obtained using METEOSAT satellites; for those in Asia, the Japan Meteorological Agency (JMA), together with the Earth Observation Research Center (EORC) from the Japan Aerospace Exploration Agency (JAXA), provides imagery from Himamawari satellite, while data from the Chinese Fengyun weather satellites can be accessed at the Chinese Meteorological Agency web-page[1]. In addition, other institutions such as the International Satellite Cloud Climatology Project (ISCCP) compile cloud atlases using raw data from some of the aforementioned satellites and other sources.

However, given that the access to these images is sometimes not free; and often there are limitations as to which organizations can access them, two specific datasets were chosen for the cloud model validation analyses: *EUMETSATS's Cloud Mask* dataset [8] and the *ISCCP Gridded Cloud Product (D1)* [33].

The EUMETSAT's Cloud Mask dataset is a collection of binary pixel-level scenes, where each pixel is classified as clear sky over water, clear sky over land, clouds or out-of-disk. It covers latitudes between -65S and 65N, and longitudes between -65W and 65E. A full-disk image is produced every 15 minutes, and data from 2004 onwards can be downloaded.

The ISCCP Gridded Cloud Product (D1) is a global data product that contains spatial averages of weather quantities and statistical summaries, including properties of cloud types, projected into a 280 km equal-area grid. Cloud presence is detected using an algorithm[2] that uses space contrast tests in the IR channel, together with radiance threshold algorithms in both IR and VIS images. Data is recorded every three hours, and is available for the range of dates from July 1983 to December 2009.

---

[1]http://satellite.cma.gov.cn/
[2]http://isccp.giss.nasa.gov/newalg.html

3.2.3 Dataset processing

As each of the datasets uses its own format and reference system, and encodes cloud information using different values, it is necessary to pre-process the data before further analysis can be done. In addition, missing values due to malfunctioning of the satellites, errors in the processing facilities or scheduled maintenance operations are accounted for at this stage. This section describes the steps carried out during this preprocessing stage to standardize the data.

The EUMETSAT dataset scenes are 3712 x 3712 pixel images with each pixel taking one of three possible values, depending whether there are clouds, clear skies or the pixel is out of the Earth-disk. In order to make it easier to compare the cloud values to those in the MODIS dataset, it is necessary to do a mapping from this reference system to the Climate Modeling Grid reference System. The LRIT/HRIT Global Specification [9] includes instructions to map each of the EUMETSAT disk pixels to its geographical coordinates latitude and longitude.

In contrast, the ISCCP dataset contains cloud statistics of 6595 equal-area tiles that cover the whole surface of the world. A single value cloud-average is given for each of these tiles. Each tile's side is approximately 280-km and the distribution of cells is depicted in Figure 3-1. Two pre-processing operations are defined for this dataset.

- Define a function to map this gridded-average values to the Climate Modeling Grid reference system, assuming that the cloud fraction on every point of the grid equals the tile-average.

- Define a function, given a set of cloud values expressed in the Climate Modeling Grid, to compute the cloud fraction average values for the ISCCP tile-grid.
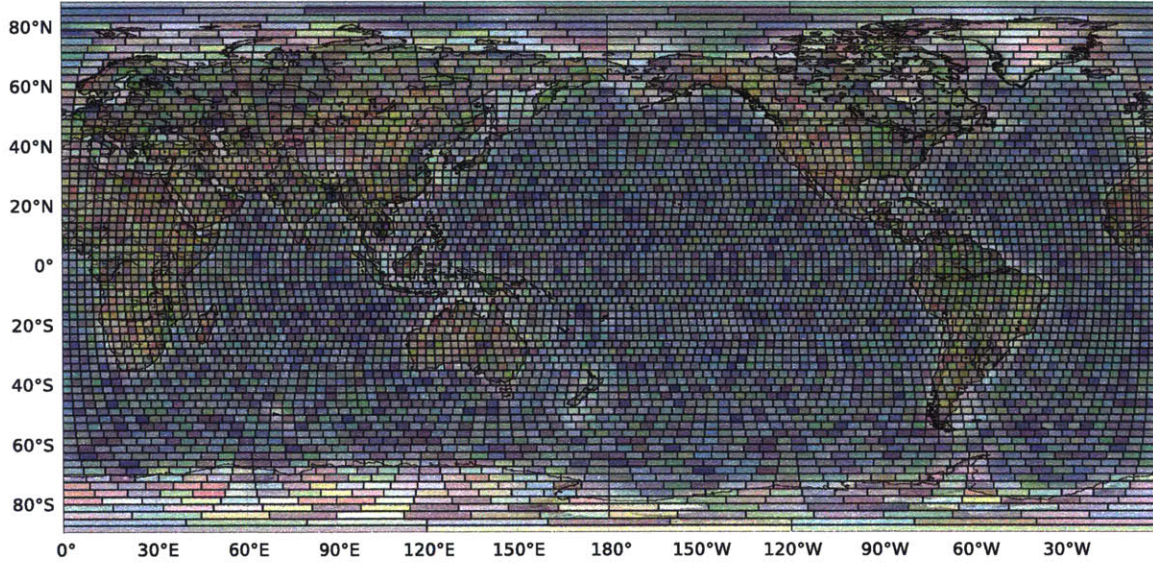
Figure 3-1: ISCCP tile distribution map.

3.2.4 Metric definition

The goal of this section is to determine the metrics used during the validation of the different models. The models in ONGSA can be classified in two types. On one hand, there are models that provide single point predictions, such as the dependence index model; on the other hand, there are models which provide a temporal series of values that correspond to a stochastic process. For both types of models, standard statistical point-wise measures can be used to determine how close the values predicted by the models are to the actual real values. The metrics used in our analysis are:

- The Mean Absolute Error (MAE) is, a point-wise metric that computes the how close the forecasts $(f(x_i))$ are to the real values (y_i). The mean absolute error is given by:

$$\text{MAE} = \frac{1}{N} \sum_{i=1}^{N} |f(x_i) - y_i| \tag{3.1}$$

- The Root Mean Square Error (RMSE), another point-wise metric that computes

the deviations between forecasts ($f(x_i)$) and real values (y_i). The RMSE gives higher importance to larger error that the MAE. It is computed as:

$$\text{RMS} = \sqrt{\frac{1}{N} \sum_{i=1}^{N} (f(x_i) - y_i)^2} \tag{3.2}$$

3.2.5 Temporal scale validation

The temporal scale validation tries to quantify the error incurred when using the values from the MODIS monthly cloud fraction dataset to approximate the cloud probabilities. The first analysis to perform is to compare the error among different datasets, to provide a baseline for how much cloud probability values can differ by just using different datasets is available. For that purpose, the mean monthly cloud probability values reported by EUMETSAT and ISCCP (assumed to be ground truth) are compared to those reported by MODIS. The mean monthly cloud probabilities are computed as the empirical mean of the binary time series for each pixel for the EUMETSAT dataset, and as the average cloud fraction on each cell for the ISCCP dataset. In addition, the values reported by ISCCP and EUMETSAT are compared as a baseline for how different these two datasets (considered to be ground truth) can be.

Table 3.1 shows the error for the MODIS dataset when compared to the EUMET-SAT and ISCCP datasets, both on the global scale and in particular regions. The average overall RMSE is 0.093 between EUMETSAT and MODIS, and 0.116 between ISCCP and MODIS. Between ISCCP and EUMETSAT, the average RMSE is 0.07. From these results it can be concluded that even though MODIS presents a slightly higher error with the two other datasets, this error is in the same order of magnitude than the error between ISCCP and EUMETSAT.

Table 3.1: RMSE of the error in the cloud probabilities for different datasets aggregated by months and regions.

RMSE EUMETSAT - MODIS		Monthly averages 2005-2006 and 2010-2011											
Region	**Avg.**	Jan	Feb	Mar	Apr	May	Jun	Jul	Aug	Sep	Oct	Nov	Dec
Overall	0.093	0.112	0.085	0.086	0.090	0.090	0.099	0.102	0.102	0.098	0.084	0.078	0.086
Sea	0.079	0.107	0.076	0.079	0.077	0.071	0.078	0.081	0.081	0.083	0.069	0.065	0.074
Land	0.120	0.122	0.101	0.100	0.115	0.125	0.139	0.143	0.142	0.128	0.113	0.103	0.110
Saharian Africa	0.104	0.101	0.091	0.081	0.109	0.120	0.128	0.128	0.134	0.097	0.080	0.075	0.097
Sub-Saharian Africa	0.125	0.113	0.105	0.102	0.116	0.127	0.150	0.151	0.148	0.137	0.129	0.111	0.112
Western Europe	0.096	0.147	0.115	0.104	0.089	0.074	0.069	0.075	0.080	0.085	0.092	0.109	0.116
Eastern Europe	0.086	0.129	0.088	0.087	0.068	0.069	0.072	0.077	0.076	0.075	0.078	0.105	0.112
Middle East	0.190	0.144	0.120	0.145	0.219	0.254	0.266	0.277	0.255	0.185	0.152	0.120	0.141

RMSE ISCCP - MODIS		Monthly averages 2005-2006											
Region	**Avg.**	Jan	Feb	Mar	Apr	May	Jun	Jul	Aug	Sep	Oct	Nov	Dec
Overall	0.116	0.106	0.107	0.123	0.118	0.123	0.136	0.133	0.119	0.104	0.104	0.101	0.121
Sea	0.098	0.092	0.097	0.103	0.092	0.100	0.113	0.111	0.103	0.087	0.086	0.084	0.104
Land	0.154	0.133	0.129	0.163	0.172	0.168	0.184	0.179	0.151	0.138	0.142	0.137	0.155
Saharian Africa	0.160	0.128	0.134	0.179	0.194	0.203	0.186	0.180	0.183	0.182	0.154	0.090	0.101
Sub-Saharian Africa	0.150	0.127	0.139	0.141	0.148	0.154	0.164	0.164	0.174	0.167	0.168	0.129	0.122
Western Europe	0.091	0.121	0.112	0.084	0.073	0.069	0.083	0.095	0.096	0.077	0.071	0.098	0.116
Eastern Europe	0.098	0.139	0.096	0.072	0.069	0.075	0.084	0.091	0.099	0.079	0.072	0.144	0.150
Middle East	0.146	0.130	0.115	0.145	0.198	0.189	0.165	0.182	0.183	0.135	0.105	0.091	0.110

RMSE ISCCP - EUMETSAT		Monthly averages 2005-2006											
Region	**Avg.**	Jan	Feb	Mar	Apr	May	Jun	Jul	Aug	Sep	Oct	Nov	Dec
Overall	0.070	0.101	0.065	0.069	0.067	0.068	0.070	0.070	0.066	0.074	0.067	0.060	0.060
Sea	0.065	0.101	0.061	0.063	0.062	0.063	0.063	0.062	0.061	0.065	0.062	0.057	0.057
Land	0.079	0.100	0.073	0.080	0.076	0.077	0.084	0.084	0.077	0.091	0.077	0.066	0.066
Saharian Africa	0.096	0.128	0.089	0.131	0.110	0.090	0.084	0.086	0.078	0.122	0.098	0.066	0.075
Sub-Saharian Africa	0.079	0.112	0.071	0.077	0.075	0.075	0.081	0.085	0.075	0.090	0.077	0.066	0.065
Western Europe	0.080	0.092	0.084	0.084	0.075	0.080	0.089	0.078	0.071	0.103	0.072	0.061	0.076
Eastern Europe	0.074	0.072	0.091	0.079	0.070	0.077	0.081	0.065	0.066	0.071	0.073	0.075	0.071
Middle East	0.103	0.114	0.072	0.083	0.097	0.129	0.145	0.137	0.112	0.102	0.098	0.069	0.079

Among the different regions, Eastern and Western Europe show the greater agreement across all the datasets, while the Middle East and African regions show the

greatest discrepancies. In addition, there is greater agreement between datasets about the cloudiness over the sea areas than over land areas. Finally, from a time-wise perspective, a cyclic behavior of the error for the ISCCP-MODIS comparison can be observed, but not in the rest of the comparisons. Note that in general, the summer months show the greatest differences between datasets (especially across the regions in the Southern Hemisphere). Moreover, the month of January also shows larger error values for those comparisons that involve the EUMETSAT dataset.

Figure 3-3 shows different worldmap plots that quantify the difference on every region. Note how the MODIS dataset underestimates the probability of clouds for region of the Gulf of Guinea and the proximities of Cape Verde in comparison to the EUMETSAT dataset, whereas for the regions of Saudi Arabia, Yemen and Oman MODIS indicates clearer skies compared to EUMETSAT. By comparing MODIS to the ISCCP dataset, it can be observed that there are big differences in the Andean states, Southeast Asia, Colombia and Venezuela in addition to the aforementioned areas. Finally, the comparison between ISCCP and EUMETSAT shows the biggest differences in parts of Saudi Arabia and the Persian Gulf.

From both the table and the images, it can thus be concluded that the differences in the results obtained using the MODIS monthly cloud fraction dataset, as opposed to other options, can be bounded within 10%. However, if the error between the ISCCP and the EUMETSAT dataset is compared, as depicted in Figure 3-3b, the value is similar to the one obtained for the comparison between MODIS and the rest of the datasets. Therefore it is difficult to establish one of these dataset as ground truth. Note that the cloud fraction values reported on each of them depend on the algorithms used to process the raw data captured by the instruments on-board the satellites.

Finally, Figure 3-2 shows histograms for the RMSE and the MAE errors when comparing the EUMETSAT dataset to the MODIS dataset. Note that both histograms are heavily right-skewed, with the biggest mass concentrated in the interval $[0, 0.1)$. In particular, the mean RMSE is 0.114, while the mean MAE is 0.093. Also, note that 10% of the points have an error greater than 0.2, both in RMSE and in

MAE. This indicates that the results might be highly dependent on the dataset used to assess the cloud probability. Section 3.3.3 presents the results on the availability when using different cloud datasets.
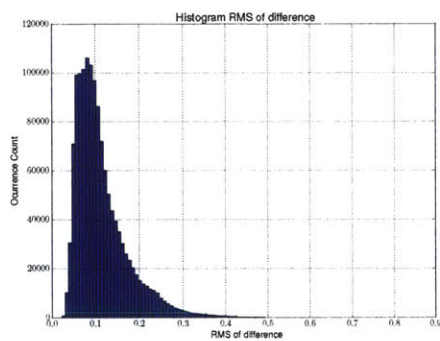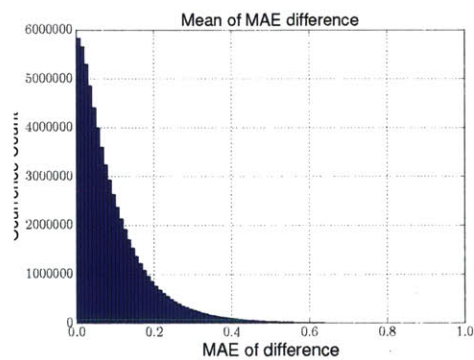
(a) Histogram of the RMSE   (b) Histogram of the MAE

Figure 3-2: Histogram of errors between the EUMETSAT and the MODIS datasets for the years 2005, 2006, 2010, and 2011

71
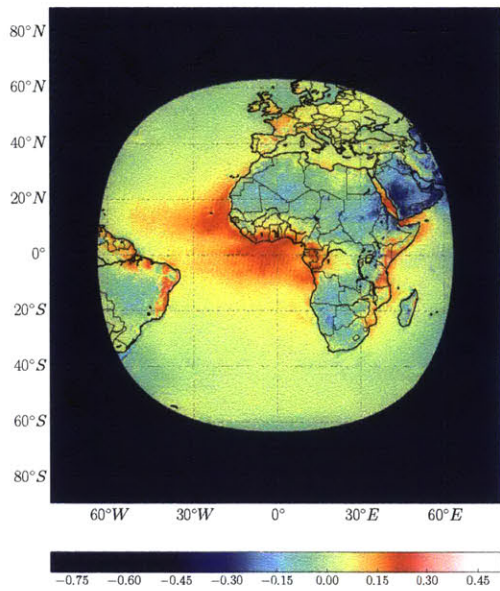
(a) Difference between EUMETSAT and MODIS
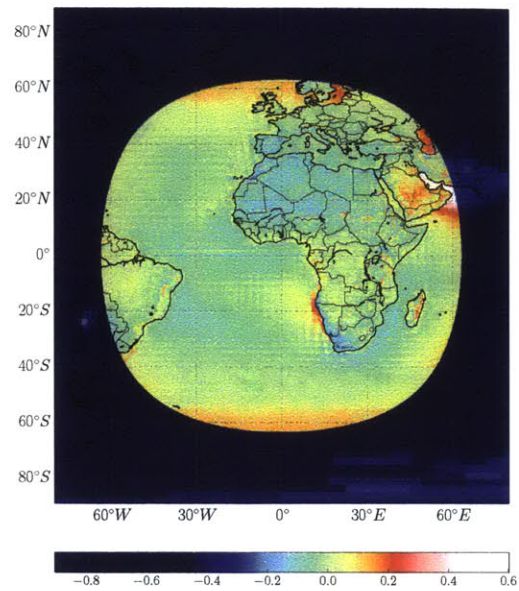
(b) Difference between ISCCP and EU-METSAT
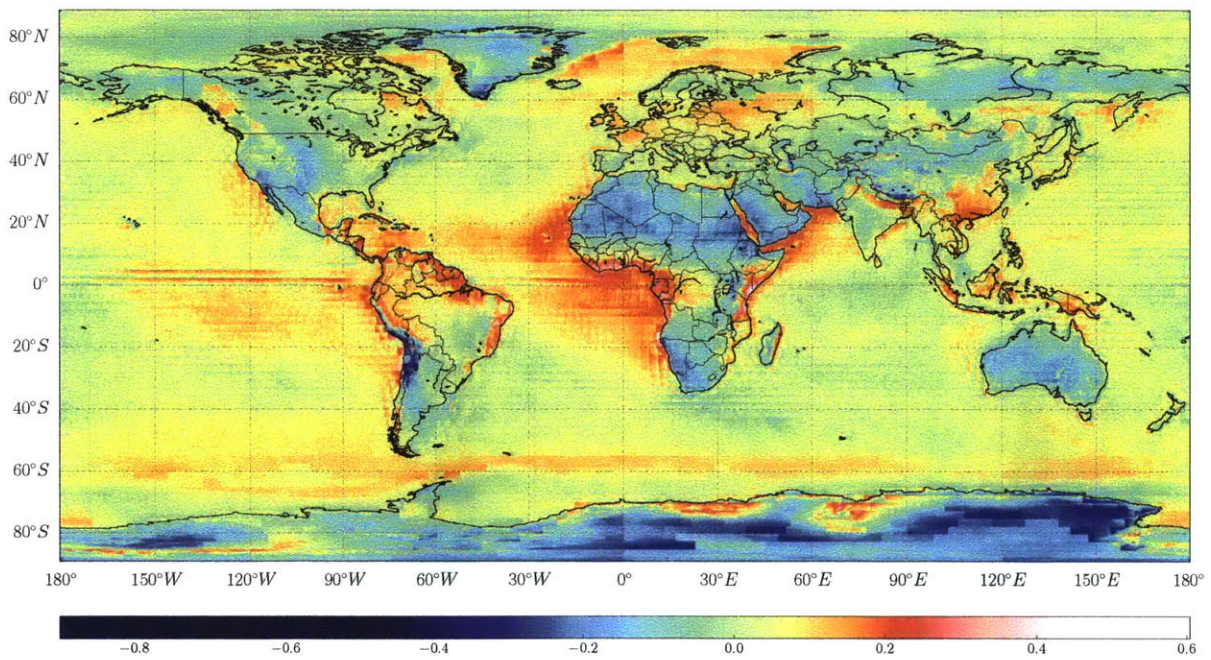
(c) Difference between ISCCP and MODIS

Figure 3-3: Average of the differences between monthly averages computed for different datasets

72

3.2.6 Spatial correlation validation

The goal of the second analysis is to validate the spatial correlation cloud model described in Section 2.3.1. Remember that the model approximates the monthly joint cloud probability of ground stations A and B by:

$$\mathbf{P}(A \cap B)_m = \chi_{A,B}\mathbf{P}(A)_m\mathbf{P}(B)_m \tag{3.3}$$

where A and B refer to the events "*Clouds over the OGS_x*", $x \in \{A, B\}$ and $\chi_{A,B}$ is the statistical dependence index.

For this analysis the EUMETSAT dataset is used to:

- A) compute the monthly joint cloud probability of a set of correlated OGSs (that is, compute the real value of $\mathbf{P}(A \cap B)_m$)

- B) compute the average month cloud probability for each of the OGSs ($\mathbf{P}(A)_m$ and $\mathbf{P}(B)_m$), and then apply the spatial correlation model described in Eq. 3.3 to compute the joint cloud probability.
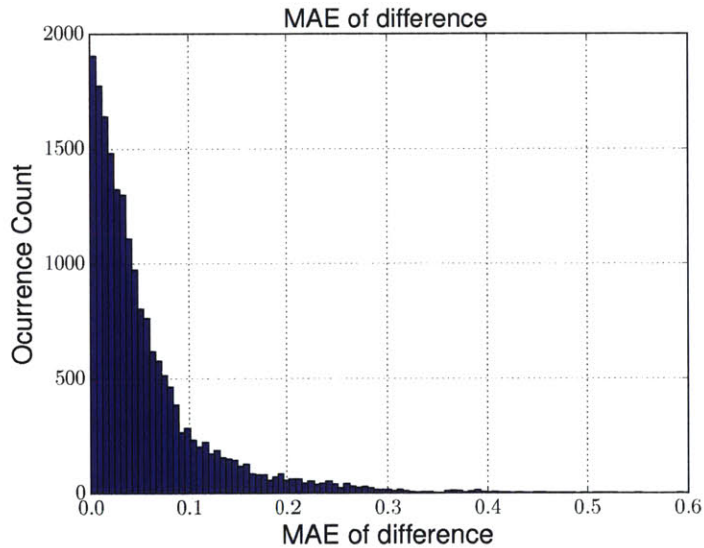
Figure 3-4: Histogram of MAE for the spatial correlation model error

Finally, the error (i.e., the difference between A) and B)) is computed. The RMSE

is 0.084 whereas the MAE is 0.057. A histogram for the MAE is depicted in Figure 3-4. Note how the highest portion of mass is concentrated below 0.1, which means that the estimates calculated using the model of the joint cloud probability are within 0.1 of the true value most of the times.
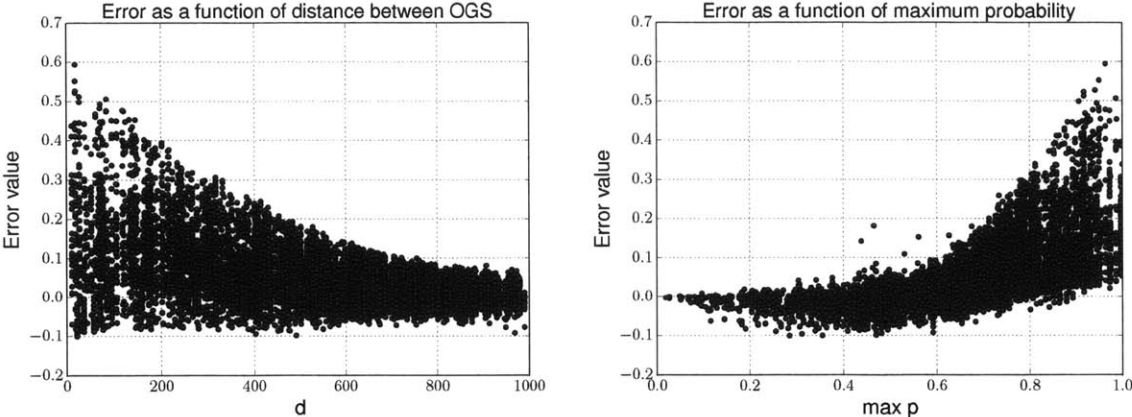
(a) Spatial dependence index errors vs. distance between OGSs

(b) Spatial dependence index errors vs. maximum probability in $\mathbf{P}(A)_m$, $\mathbf{P}(B)_m$

Figure 3-5: Dependence of the spatial dependence index errors with the distance and maximum probability

Next, the behavior of the errors with respect to the distance between the pair of correlated ground stations and with respect to the marginal cloud probabilities is analyzed. Figure 3-5a shows how the variance of the errors decreases as the distance increases. This is due to the fact that the further away the OGSs are located the more independent they are, and therefore the value of the statistical dependence index approaches 1. In this situation the joint cloud probability equals the product of the marginal probabilities. Figure 3-5b shows the dependence of the errors on the maximum marginal probability (i.e., the maximum between $\mathbf{P}(A)_m$ and $\mathbf{P}(B)_m$). It can be observed that the higher the maximum probability, the more deviation in the errors. This is due to the formulation of the model; in reality, the maximum value that the joint cloud probability can take is bounded by the maximum marginal probability, but in our model the joint probability value can be higher (for very high probabilities, it can even be greater than 1). This is one of the main limitations of

the spatial correlation model. Chapter 5 outlines several alternative formulations to overcome these issues.

3.3 Availability model validation

3.3.1 Methodology

To validate the availability model, three separate analyses are performed. First, Section 3.3.2 assesses the error of the availability model by computing the availability of a set of architectures using the EUMETSAT dataset. As the EUMETSAT dataset includes only data from Europe and Africa, the set of architectures will only have OGSs located in this region. The candidate locations for the OGSs for this analysis are the same that those described in the Annex of [10].

Second, Section 3.3.3 compares the results obtained using the model described in Section 2.3 with the MODIS dataset to the results obtained using all the values existing in the EUMETSAT and the ISCCP datasets. The same architectures defined for the analysis in Section 3.3.2 are used in this analysis. Additionally, a second set of 10,000 architectures is defined for the ISCCP dataset. These architectures contain OGSs located uniformly across the world.

In the third analysis, the results for certain architectures are compared to the values reported in previous work. The results of this comparison are reported in Section 3.3.4.

3.3.2 Error assessment for the EUMETSAT dataset

In this analysis, the network availability for the years 2005, 2006, 2010, and 2011 is computed for 10,000 randomly selected architectures. The monthly availability using the 2-hour time interval data (ground truth) is compared to the values obtained using ONSGA (i.e., using the monthly probabilities and the dependence index) (model approach). Note that two assumptions are made here:

- The monthly average is a sufficient statistic to compute the monthly availability,

and

- The spatial correlation model is used to capture spatial correlations

The histogram of RMSE and MAE for this analysis is presented in Figure 3-6. The mean RMSE is 0.0519 whereas the mean MAE is 0.0393. Percentage-wise, the mean percentage absolute error is 2.89% and the mean percentage RMSE is 4.24%. The histograms show that most of the errors concentrate around 0, and that no more than 1% of the architectures show an error greater than 0.2.

(a) Histogram of the RMSE   (b) Histogram of the MAE
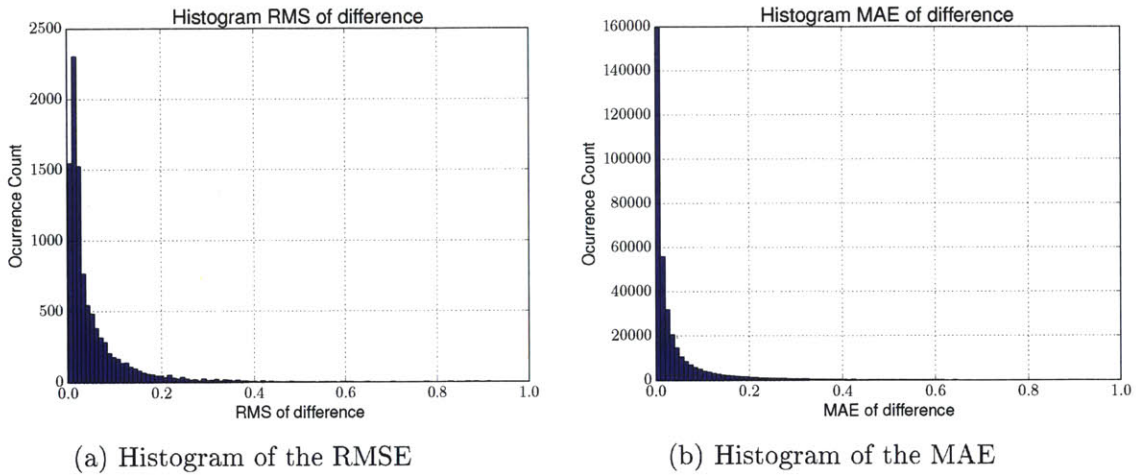
Figure 3-6: Histogram of errors between the availability model and ground truth using the EUMETSAT datasets for the years 2005, 2006, 2010 and 2011

Figure 3-7 shows the predicted time series (in blue) and the ground truth time series (in green) for nine randomly selected architectures, each architecture having between three and ten OGSs. The number in parentheses next to the number of ground stations indicates the number of pairs of ground stations spatially correlated within the architecture.
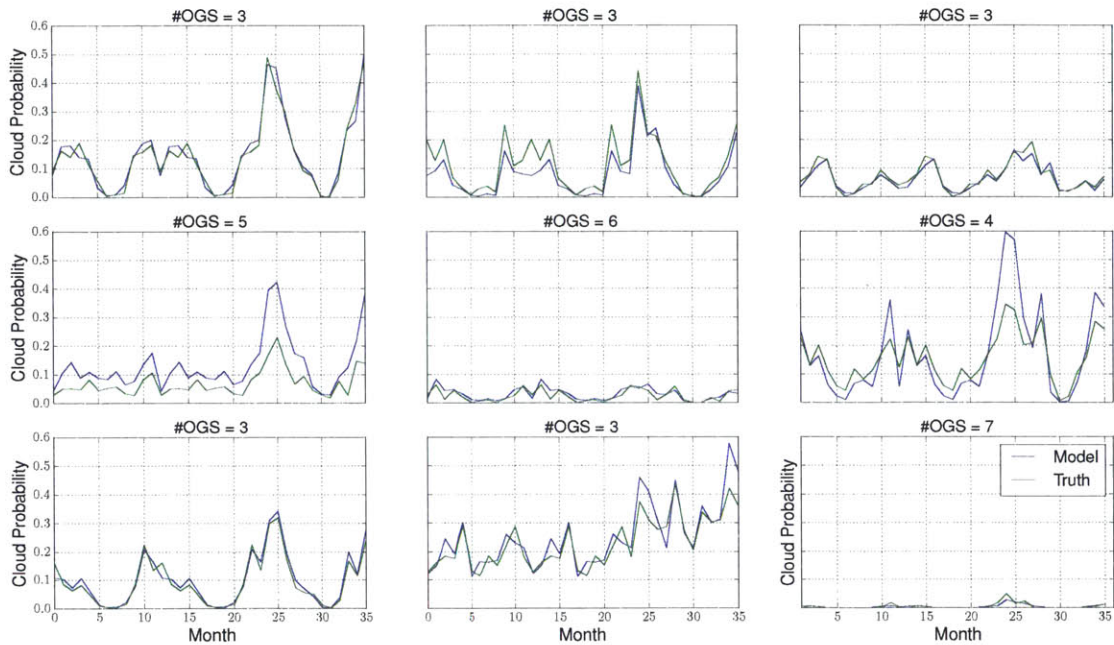
Figure 3-7: Comparison of predicted availability and ground truth for nine randomly selected architectures

Note that this availability error can be attributed to two main errors. On one hand, there is error due to taking monthly averages instead of 2-hour empirical data; on the other hand, there is also error obtained from using the correlation model. It would be interesting to see if the error in the availability increases as the number of correlated pairs of ground stations increases, and to that end, no significant differences in the mean errors (both RMSE and MAE) are observed among those architectures that have different number of OGSs correlated.

3.3.3 Comparison with other datasets

This section assesses the differences in the results obtained using the MODIS dataset to estimate the monthly cloud probabilities of ONGSA to those obtained using other datasets such as ISCCP or EUMETSAT. Then, the magnitude of these errors is compared to the differences obtained in Section 3.2.

Figure 3-8 shows the predicted and ground truth values for the different datasets considered. The first thing of note is that the ground truth values differ heavily

depending on the model used to establish the ground truth data (ISCCP or EU-METSAT). This is due largely to the difference in values between the datasets (as explained in Section 3.2.5). Secondly, by viewing the plots, the values reported when using the MODIS dataset to estimate cloud probabilities are closer to those reported when using the ISCCP dataset in cases 1, 2, and 7, while in cases 4, 8, and 9 these values are closer to those reported with the EUMETSAT dataset. This surprising fact suggests that the results are highly dependent on the dataset used to approximate the monthly cloud probabilities. Assessing the impact and validity of the different datasets, as well as quantifying in a more rigorous manner the differences between datasets is a topic for future research. as described in Section 5.4.
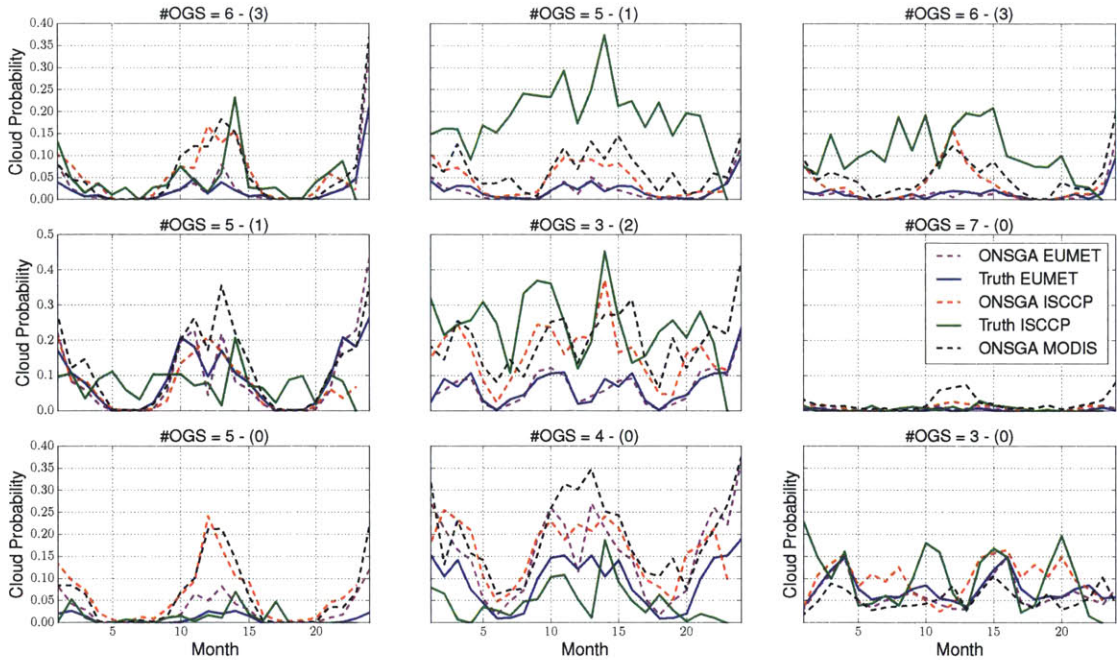
Figure 3-8: Comparison of availability using different datasets for nine randomly selected architectures

Table 3.2 contains the MAE and RMSE for the monthly availability for 10,000 architectures computed using the different datasets to evaluate the monthly cloud probabilities. Note that both tables are symmetric. The errors for ONGSA using the cloud probabilities from MODIS (this is the dataset used in the analysis in Chapter 4) have been marked with bold font. Two interesting conclusions can be drawn from

the numbers obtained. First, the error using MODIS is similar to the error between the ground truth values when using the ISCCP and EUMETSAT datasets (marked in red). Note that these values are on the same order of magnitude than the error obtained among dataset in Section 3.2. This suggests that the values obtained with the MODIS dataset are no worse than those obtained by using the other datasets. Second, the error between ONGSA using MODIS is smaller than the error when using ONGSA with any of the other datasets (even though the values obtained when using MODIS are very similar to those obtained when using EUMETSAT).

Table 3.2: MAE and RMS of the error between the monthly availabilities computed for 10,000 architectures using different cloud datasets.

	MAE					RMS				
	ONGSA EUMET	ONGSA ISCCP	Truth EUMET	Truth ISCCP	ONGSA MODIS	ONGSA EUMET	ONGSA ISCCP	Truth EUMET	Truth ISCCP	ONGSA MODIS
O. EUMET	-	0.051	0.039	0.080	**0.052**	-	0.066	0.052	0.096	**0.068**
O. ISCCP	0.051	-	0.072	0.076	**0.042**	0.066	-	0.087	0.093	**0.054**
T. EUMET	0.039	0.072	-	0.073	**0.067**	0.052	0.087	-	0.087	**0.083**
T. ISCCP	0.080	0.076	0.073	-	**0.075**	0.096	0.093	0.087	-	**0.094**
O. MODIS	**0.052**	**0.042**	**0.075**	**0.075**	-	**0.068**	**0.054**	**0.083**	**0.094**	-

3.3.4 Comparison with previous work

This section compares the results obtained with ONGSA with those reported in the literature. Note that the availability metric defined in ONGSA is the value that leaves 95% of the time series of monthly optical availabilities above it (that is the 5% percentile), whereas most of the previous literature used the mean value. The rationale for using the 5% percentile was explained in Section 2.3.3. However, to make the results comparable, the average of the monthly values reported by ONGSA is used within this section.

Table 3.3: Comparison of the availability model with results from previous literature

Author	Region	Years Imagery	#GS	#Sat	Optimal Locations	ONGSA NA (%)	Litera-ture NA (%)	Error (%)
Biswas	USA	1997-2002	4	1	Goldstone (CA); Kitt Peak (AZ); McDonald Observatory (TX); and Mauna Kea (HI)	94.2	95.3	1.13
Poulenard	Europe + Middle East	2 years	5	1	Egypt, Yanbu (Saudi Arabia), Jeddah (Saudi Arabia), Gibraltar, Montpelier (France)	96.5	99.9	3.40
Poulenard	Europe	2012	4	1	Halfa (Sudan), Karak (Israel), Ouargla (Algeria), Garoowe (Somalia)	97.1	99.8	2.71
Wojzic	Worldwide	2003-2004	6	3	Goldstone, Las Campanas, HESS,Perth, Alice Spring, Mt Srombo	84.6	91.0	7.03
Link	North America	2001-2005	5	1	Mauna Kea (HI), Table Mountain (CA), Las Brisas (CO), Mount Graham (AZ), Capilla Peak (NM)	84.6	86.3	1.97
OLSG	America	2003	2	1	La Silla (Chile), White Sands (NM)	88.1	90.0	2.11

Table 3.3 compares the results reported with those obtained by ONGSA for similar architectures. The mean error in the availability between ONGSA and the values reported in the literature is 3.5%. However, there seems to be a bias in that ONGSA trends to underestimates the values computed by previous studies.

Finally, the methodology to compute the network availability (NA) had to be adapted for the cases proposed in [46, Wojcik], [25, Link] and [3, Biswas], since in these studies the network availability was computed for a network with a deep space probe. Note that the availability reported by ONGSA for the network in Wojcik presents the highest disparity across all the results. This difference occurs as this network has three OGSs spatially correlated in Australia, and as explained in Section 2.3.1 this situations are not properly captured by the current spatial correlation model.

3.4 Cost model validation

This section devotes its attention to the cost model validation. This task is particularly challenging, given that public data is scarce and most of the times not very reliable. Note that the cost model intend is to allow relative cost comparisons rather than absolute value comparisons. The main document that contains information with regard to the costs of optical ground stations is Ref. [17], in which NASA analyzed the costs of upgrading some of its ground stations to support optical communications.

To validate the cost model, the error committed during estimation of the annual cost of maintenance (non-recurring and recurring) for each of the OGSs that appear in reference [17] is evaluated. Table 3.4 compares the values obtained using the cost model integrated in ONGSA to those reported in the Optical Link Study Group (OLSG) Final Report. Note how the differences in the non-recurring costs are below 10% for half of the data points. The model does overestimate the cost of construction in Hawaii (Mauna Kea), as the area cost factor for that region in the DoD Cost Handbook is relatively high as compared to the cost factor for locations in continental US. In addition, the error on the cost of White Sands is large, as in [17] it was assumed that the telescope for the LLCD experiment could be re-used with minor modifications, reducing greatly the telescope cost. On the other hand, the recurring costs are generally underestimated by 15% (again with the exception of Hawaii) compared to the maintenance costs reported by the OLSG report. Note that [17] did not consider building costs (and therefore this part of the model could not be validated for new ground stations), and that the maintenance and operations costs is constant across ground stations in different countries.

Finally, the low number of data points prevents further statistical analysis which makes it difficult to assess the validity of the cost model beyond the conclusions presented in this section.

81

Table 3.4: Validation for the cost model

	Lifecycle cost	Non recurring cost		Recurring cost	
	M\$	k\$	error (%)	k\$	error (%)
Mauna Kea	74.6	18,397.60	84.92	2,459	57.83
La Silla	34.3	8,564.4	-10.4	1,128.3	-3.56
Table Mountain	40.8	9,833.20	5.37	1,354.1	9.64
Teide	36.7	9,198.80	9.64	1,202.2	-22.84
White Sands, SN	29.5	7,216.3 [3]	159.77	973.7	-16.78
Madrid DSN	36.7	9,198.80	3.81	1,202.2	-6.08
Hartebeesthoek	42.1	10,309	21.78	1,391	-10.72

Chapter 4

Results

4.1 Introduction

This chapter presents the results of employing ONGSA to understand the trade-offs when architecting the ground segment of the future optical space communications network. One of the fundamental questions of this thesis is to determine whether existing assets offer the best conditions to locate optical equipment for such a network or whether new locations should be considered (see Section 1.3.3). To answer this question, several scenarios have been analyzed and their results compared. The chapter starts by describing the different sets of ground stations considered and the space segment scenarios studied. Next, the results obtained after running ONGSA for each of them are analyzed and compared.

Results show that a maximum availability of 95.5 % can be achieved using an architecture similar to the actual system (the Tracking and Data Relay Satellite System) and 12 additional optical ground stations. Furthermore, an unconstrained optimization analysis identified the north of Mexico, southwest of Saudi Arabia, Morocco and central Australia as areas with high potential to construct new ground stations. Building new ground stations was identified to be a more cost-effective solution when the required level of availability is high, while using existing infrastructure is a better solution for systems when the required optical availability is low.

4.2 Scenario and candidate location sets description

4.2.1 Candidate locations sets

In order to determine whether existing assets exhibit the best conditions to place an optical ground station, five different scenarios were defined. Four of them are composed of existing assets; NASA assets from existing networks, as well as astronomical observatories are considered as potential locations for OGSs.

- Set A - NASA NEN assets: This set of candidate locations set composed of all the assets in NASA's Near Earth Network.

- Set B - All NASA assets: This set of candidate locations is formed by NASA-owned assets in the NEN, DSN and SN.

- Set C - NASA Observatories: This set of candidate locations is composed of 25 astronomical observatories proposed by NASA's Optical Link Study Group [37]. This set does not include any of the candidate OGSs contained in sets A and B.

- Set D - Astronomical Observatories: This set of candidate locations is composed of 40 astronomical observatories facilities, all of them being at an altitude greater than 1,000 m.

- Set E - Unconstrained Optimization: This set of candidate locations contains any latitude-longitude point among the borders of a set of politically stable countries. Appendix B contains further details on the list of banned countries and the criteria for considering them politically unstable.

Figure 4-1 shows the location of each of the candidate OGSs considered. Note that some regions have a high density of candidate locations (e.g., the south west of the US, or the Andes region), whereas in other regions there are not many candidate locations (e.g., Central Africa and the north of Asia including Russia). Appendix A contains further details on the candidate locations considered in this study.
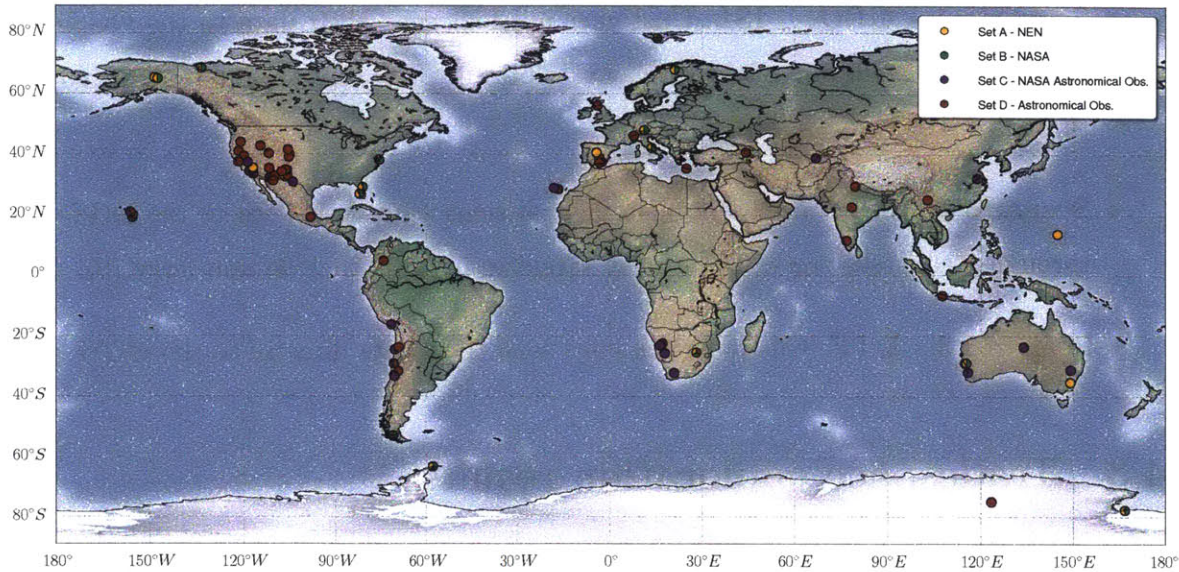
Figure 4-1: Location of the OGSs considered on each of the sets

4.2.2 Space segment scenarios

Two different approaches have been proposed to make the transition from RF architectures to hybrid RF-optical systems. The first one envisions the existence of geostationary satellites that relay the information sent from the LEO customers to the OGSs. This system would imitate the behavior of the SN nowadays. Furthermore, the use of optical ISL between the relay satellites has been proposed as an additional mechanism to combat the effects of cloud weather on link disruption [17].

The second approach is to develop a system that is similar in its operations to the NEN; in other words, the customer missions in LEO download their data directly to the OGSs. This approach is easier to carry out, as deploying optical terminals into existing infrastructure entails less risk than deploying dedicated optical relay satellites in space.

In order to understand the trade-offs in terms of availability and cost involved for each of the aforementioned approaches, the following three scenarios to serve as

inputs for the tool are defined.

- **Scenario 1 - GEO + ISL**: Customer missions send their data to the OGSs through a constellation of three relay satellites in GEO that are interconnected through ISL.

- **Scenario 2 - GEO no ISL**: Customer missions send their data to the OGSs through a constellation of three relay satellites in GEO that do not carry ISL.

- **Scenario 3 - DTE**: Customer missions send their data directly to the OGSs.

4.3 Tradespace exploration results

4.3.1 Optimal ground stations locations

The objective of this section is to determine which are the best OGSs locations for a space communications network to serve LEO customer missions. Site diversity has been identified as the main mitigation technique to guarantee high availability of the system and fight against link outage due to cloud coverage.

This section presents the results of employing ONGSA to analyze the best locations among each of the different sets of candidate OGSs, as described in Section 4.2.1. This analysis will be conducted using Scenario 2 as the baseline case. That is, customer missions send their data to the optical ground stations through a constellation of three relay satellites in GEO that do not dispose of ISL. Note that this is a similar system to the Tracking Data and Relay Satellite System, currently used by NASA to support communications from some of its Earth observation missions flying in LEO.

NASA owned assets

This first study considers current NASA-owned or -operated facilities as candidate OGSs sites. This includes sets A (assets in the NEN) and B (assets in the NEN, DSN and SN) described in Section 4.2.1.

Figure 4-2 shows the tradespace results for Set A after running the GA for 25 generations with a 20,000-architecture population size. As depicted in the graph, the maximum availability achievable using those assets in the NEN is 77.6% at a cost of $278 M. Note how the system attains its maximum availability relatively quickly, and how the benefits of increasing the number of ground stations above 11 are marginally low.
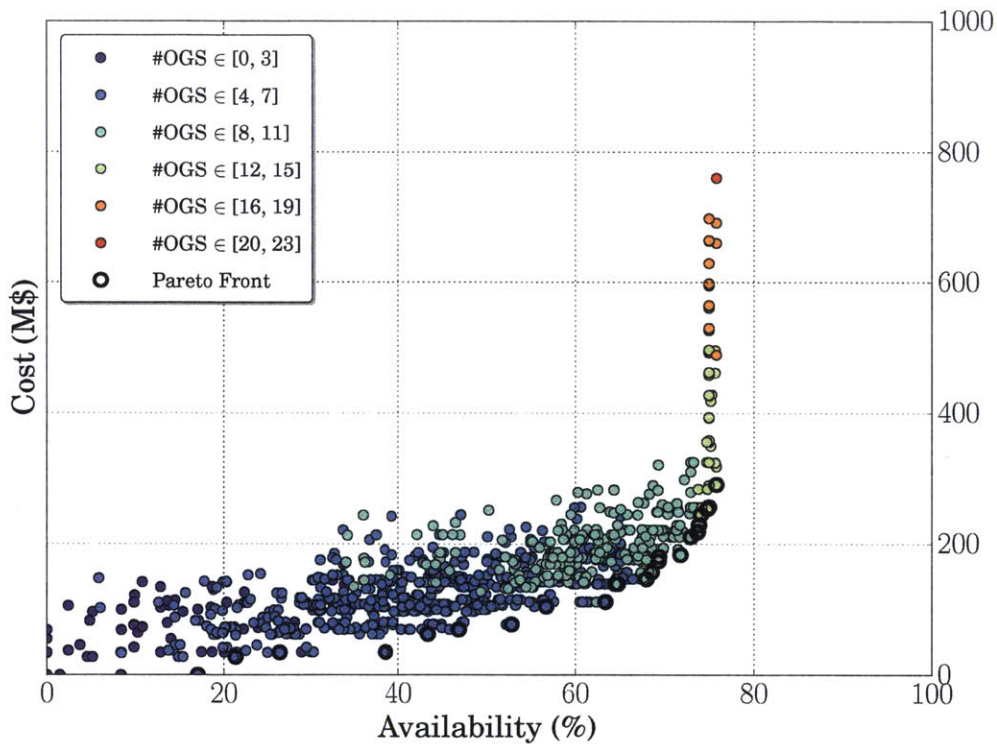
Figure 4-2: Tradespace of the GEO no ISL scenario with Set A of candidate locations.

Figure 4-3 shows the importance of each OGS within the Pareto Front architectures by representing its frequency of occurrence. Two OGSs, Wallops Flight Facility and South Point, appear on all the Pareto Front architectures, whereas Santiago Satellite Stations is also a common choice. In addition to these, Hatebeesthoek in South Africa and the USN Western Australia ground station appear on more than half of the Pareto Front architectures. Figure 4-3b represents this same information on a world map, where the size and intensity of the red circle around each candidate

87

location is proportional to its popularity.
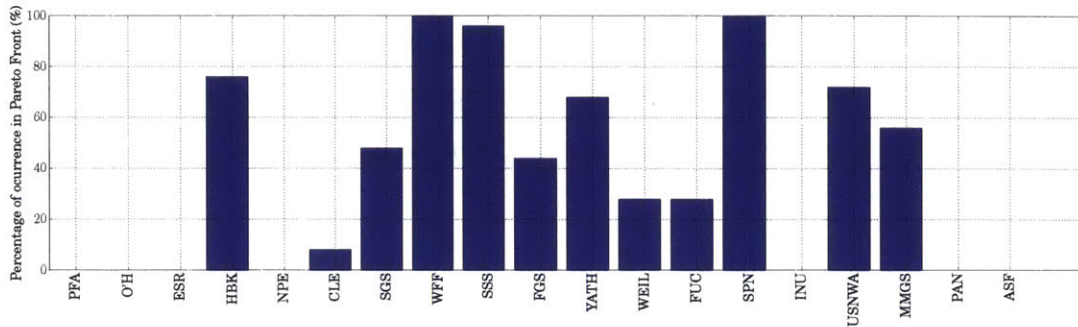
(a) Importance of each candidate OGS of Set A in the Pareto Front. The complete name of each ground station can be found in Table A.3 in Appendix A.
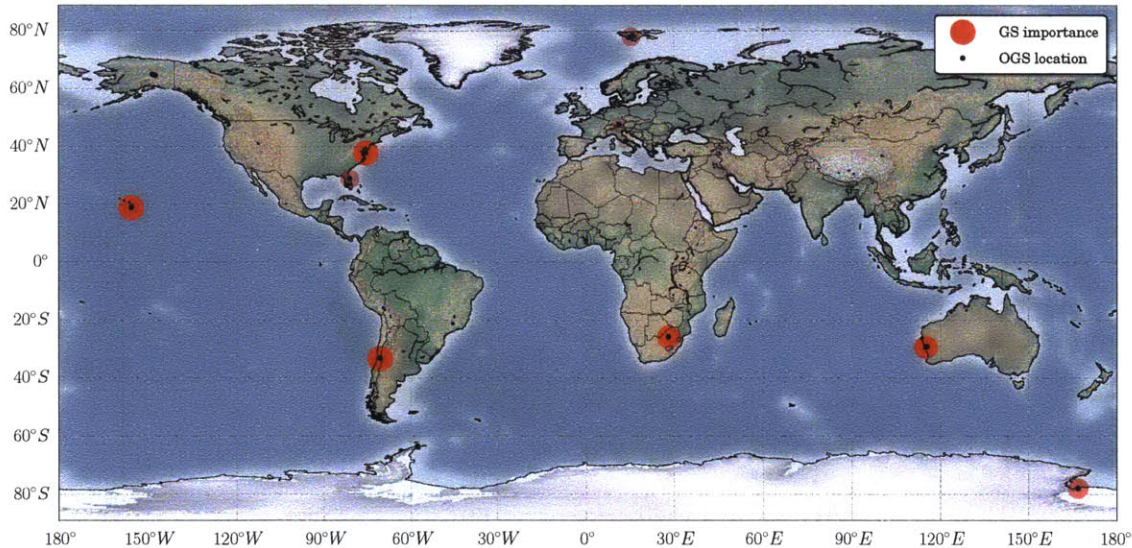
(b) Worldmap showing the importance of each OGS of Set A for the GEO no ISL scenario.

Figure 4-3: OGS importance for the GEO no ISL scenario with Set A of candidate locations

On the other hand, when the set of candidate OGSs is expanded to include the assets from the SN and the DSN, the maximum availability attainable is increased to 84.2%, at a cost of $450 M, as Figure 4-4 shows. This availability value is achieved using a network of 15 OGSs. Similarly, an investment of $200 M yields a maximum availability of 76.4% using 10 OGSs. Networks with more than 15 OGSs do not offer

significant increases in terms of availability of the network.
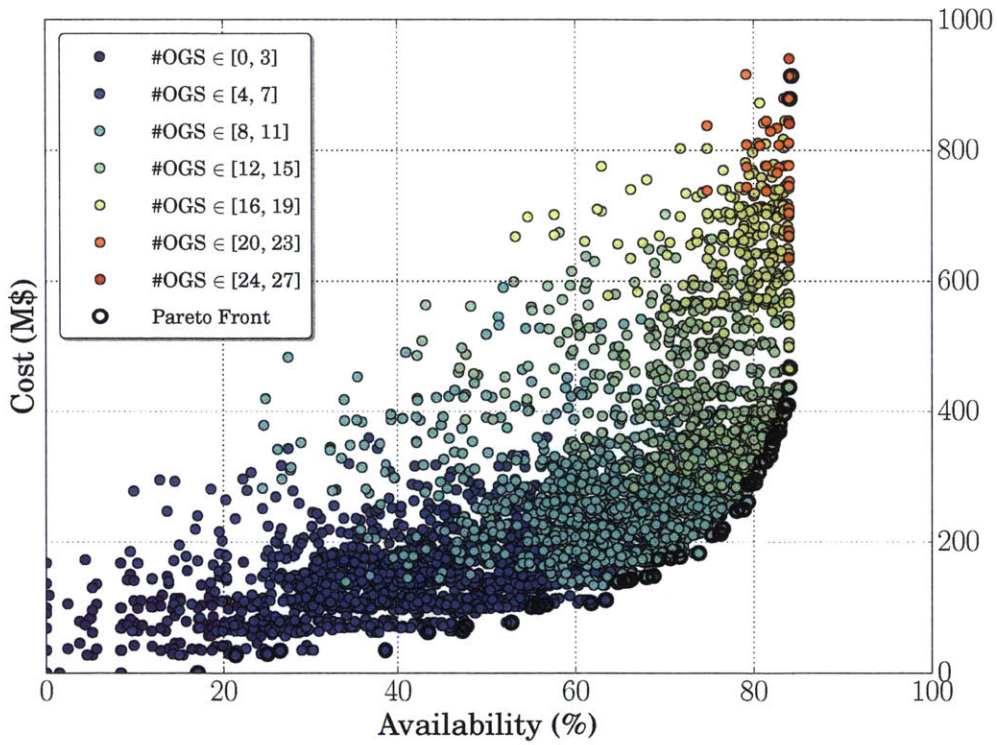
Figure 4-4: Tradespace of the GEO no ISL scenario with Set B of candidate locations.

Figure 4-5 depicts the importance of each OGS in the Pareto Front architectures, both numerically in the bar-plot (Fig. 4-5a) and graphically in the world map (Fig. 4-5b). Both Wallops Flight Facility and South Point appear again in all the Pareto Front architectures. The rest of the OGSs identified in the previous analysis (using Set A - NEN assets) are still identified as popular candidate locations. Finally, White Sands Complex (US) and Madrid (SP), two of the OGSs added to Set A in this analysis, appear in more than 50% of the architectures in the Pareto Front.
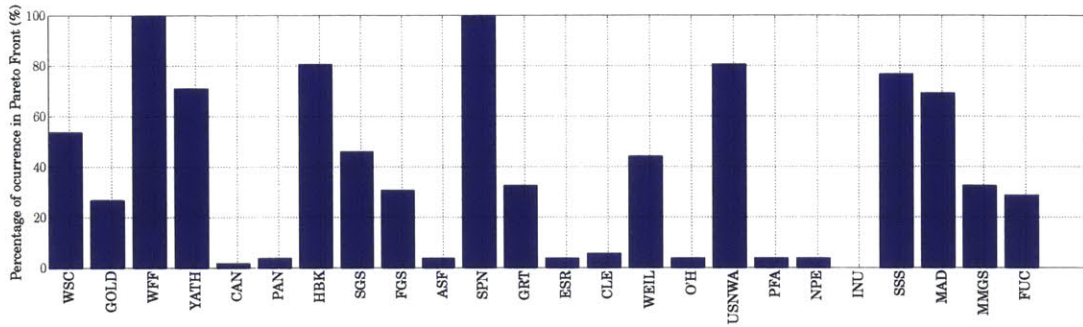
(a) Importance of each candidate OGS of Set B in the Pareto Front. The complete name of each ground station can be found in Table A.1 in Appendix A.
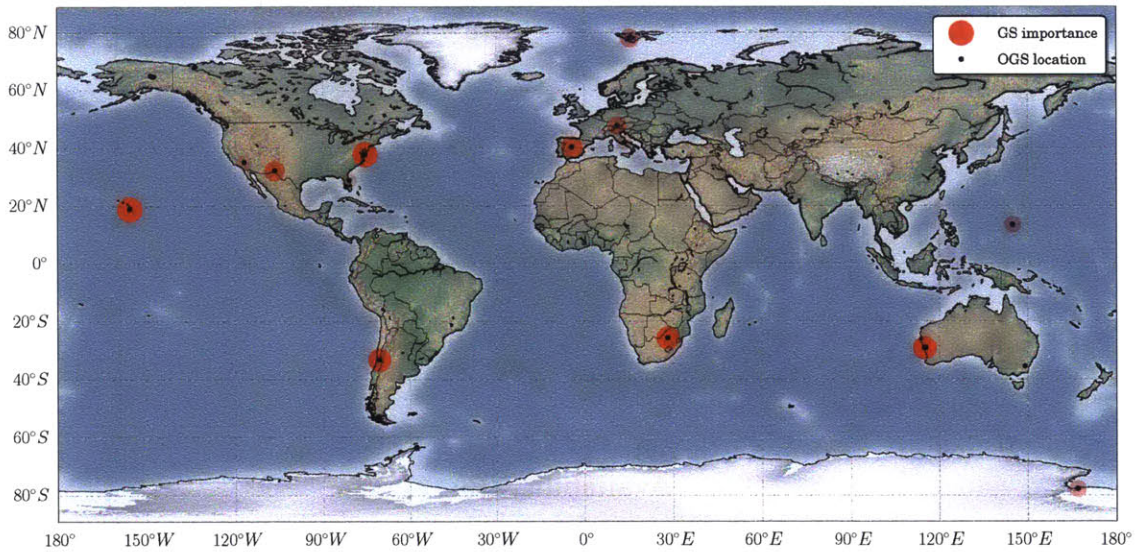
(b) Worldmap showing the importance of each OGS of Set B for the GEO no ISL scenario.

Figure 4-5: OGS importance for the GEO no ISL scenario with Set B of candidate locations

NASA astronomical observatories

In this case, the analysis conducted in the previous section is reproduced but using Set C (NASA handpicked astronomical observatories) as the candidate set of OGSs. All the optimization parameters are similar to the ones described in Section 4.3.1. Figure 4-6 depicts the tradespace results, whereas Figure 4-7 describes the relative importance of each astronomical observatory considered.

90

Figure 4-6 shows that an architecture with a cost of $200 M offers an availability of 90.6% using 6 OGSs, whereas an availability of 94.3% can be reached using a network of 14 OGSs at a cost of $500 M. Note that the maximum availability achievable when using astronomical observatories proposed by NASA (95.5%) is clearly superior to the availability attainable when using current NASA assets.
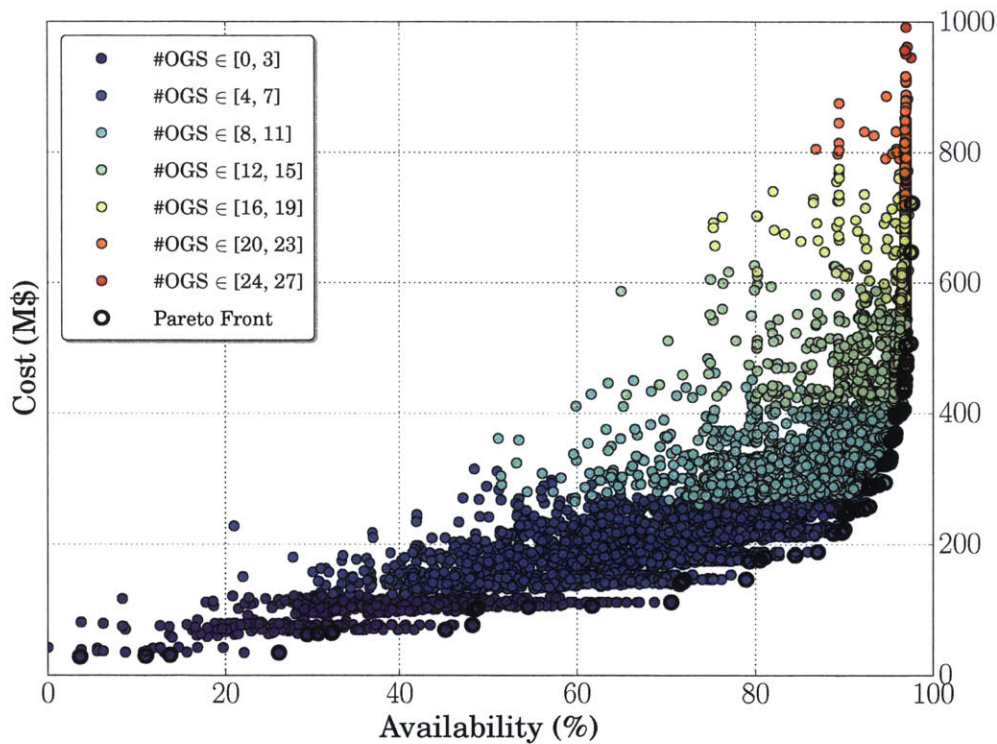
Figure 4-6: Tradespace of the GEO no ISL scenario with Set C of candidate locations.

Figure 4-7a shows the frequency of appearance of each candidate location in the Pareto Front architectures, whereas Fig. 4-7b shows this same quantity on a worldmap. Six OGSs appear in more than 50% of the architectures in the Pareto Front. These are (ordered by descending popularity) Paranal (CL), Alice Springs (AU), Perth Observatory (AU), Astron Observatory (SA), Gamsberg (NA), and Australian Astronomical Observatory (AU). Note that all of these observatories are located in the Southern Hemisphere. Attractive regions are the Andes Mountain Range, the south of Africa (Namibia and South Africa) and Australia. In addition,

91

some regions in the south of Spain and the Canary Islands, as well as the south of the United States appear occasionally among the OGSs of the Pareto Front architectures.
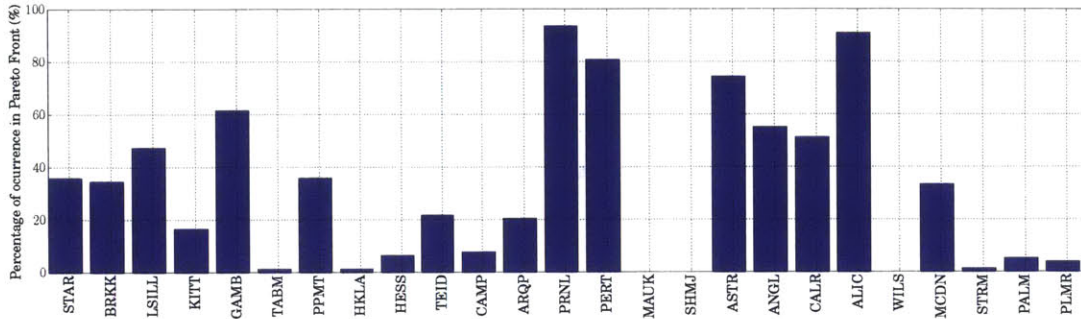
(a) Importance of each candidate OGS of Set C in the Pareto Front. The complete name of each ground station can be found in Table A.2 in Appendix A.
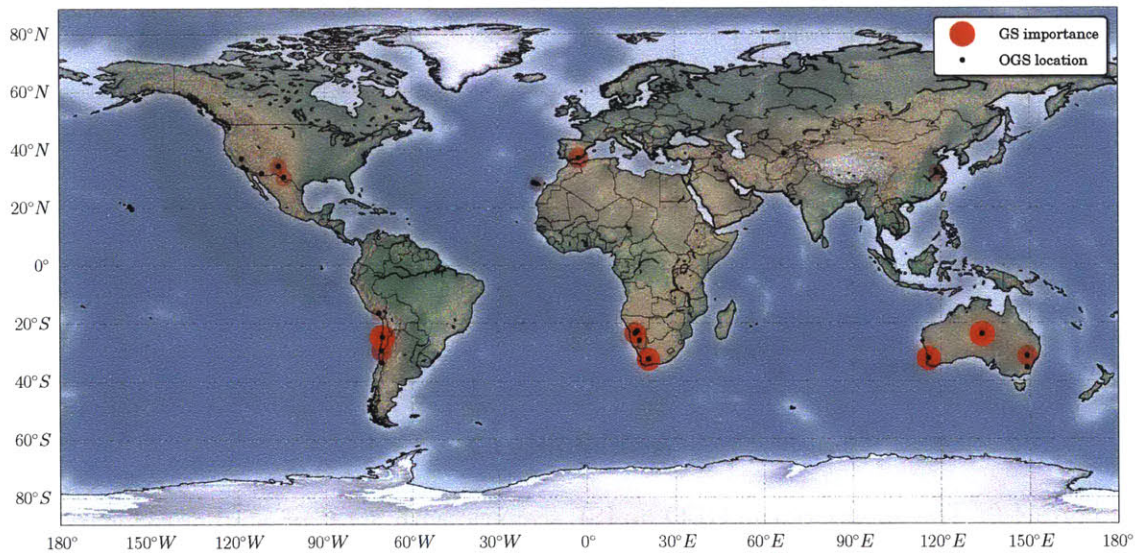
(b) Worldmap showing the importance of each OGS of Set C for the GEO no ISL scenario.

Figure 4-7: OGS importance for the GEO no ISL scenario with Set C of candidate locations

Worldwide astronomical observatories

This section presents the results of conducting a similar analysis but using Set D as candidate locations for the OGSs – 40 astronomical observatories worldwide at a height higher than 1000 m.

Figure 4-8 shows that a constellation of three relay satellites without ISL can achieve availabilities of 80.5% at a cost of $211 M using six OGSs, whereas availabilities around 91% are achieved at an expense of $400 M and twelve OGSs. The maximum availability achieved is 96.3% using 20 OGSs. Note that this value is slightly inferior to the maximum availability attained when using the set of NASA's handpicked astronomical observatories, while the costs curves are similar for both cases.
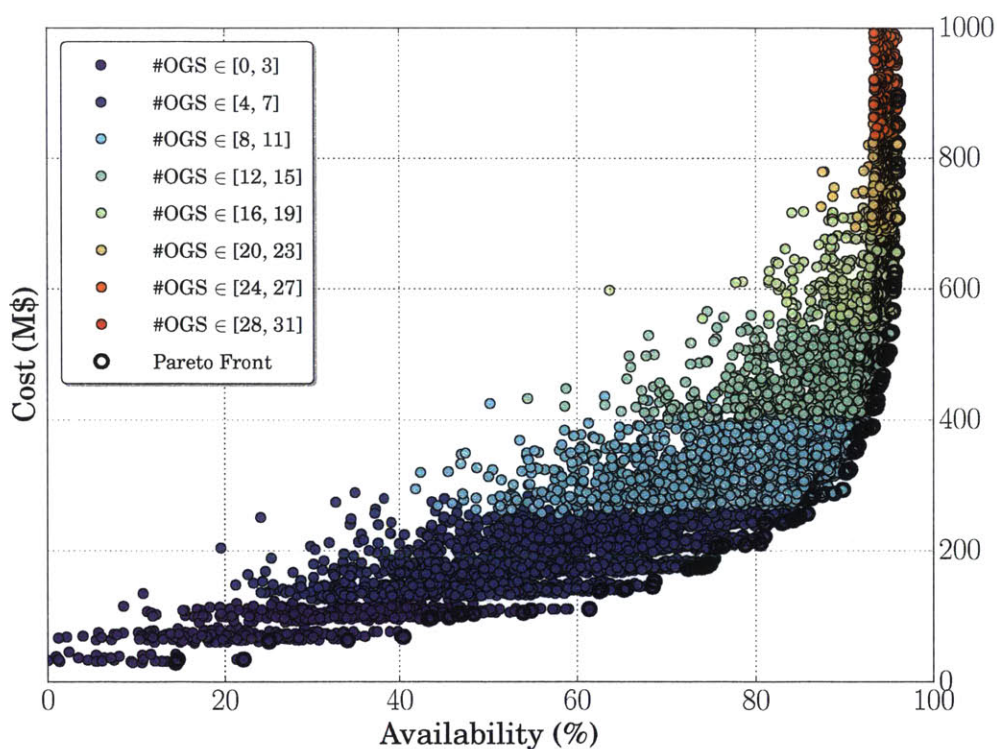
Figure 4-8: Tradespace of the GEO no ISL scenario with Set D of candidate locations.

Figure 4-9 shows the importance of each OGS within the Pareto Front. Seven OGSs appear in more than half of the Pareto Front architectures. These are (in decreasing order of popularity) Aryabhatta Research Institute of Observational Sciences (IN), the High Energy Stereoscopic System (NA), La Silla Observatory (CL), Ooty Radio Telescope (IN), IRAM Telescope (SP), Siding Spring Observatory (AU), and Hartebeesthoek Radio Astronomy Observatory (SA). Note that some areas such as

Chile, Namibia, and Australia were already identified as good candidate locations in the previous analysis, whereas India is incorporated in this analysis. This fact indicates that future analysis may want to include astronomical observatories in this region in the set of candidate OGSs considered.
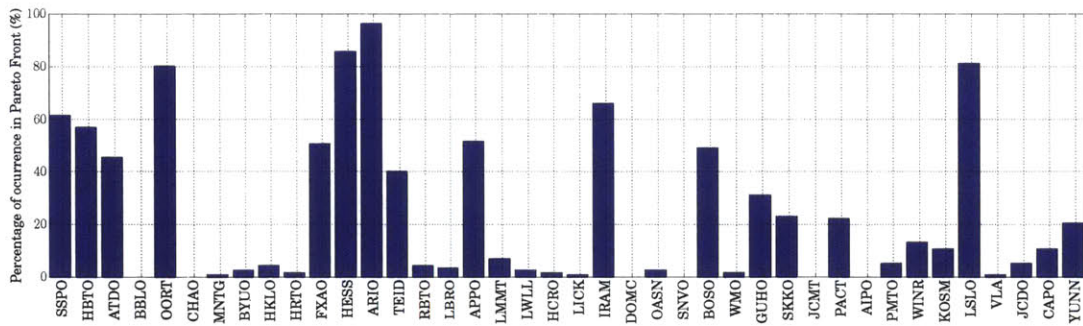
(a) Importance of each candidate OGS of Set D in the Pareto Front. The complete name of each ground station can be found in Table A.3 in Appendix A.
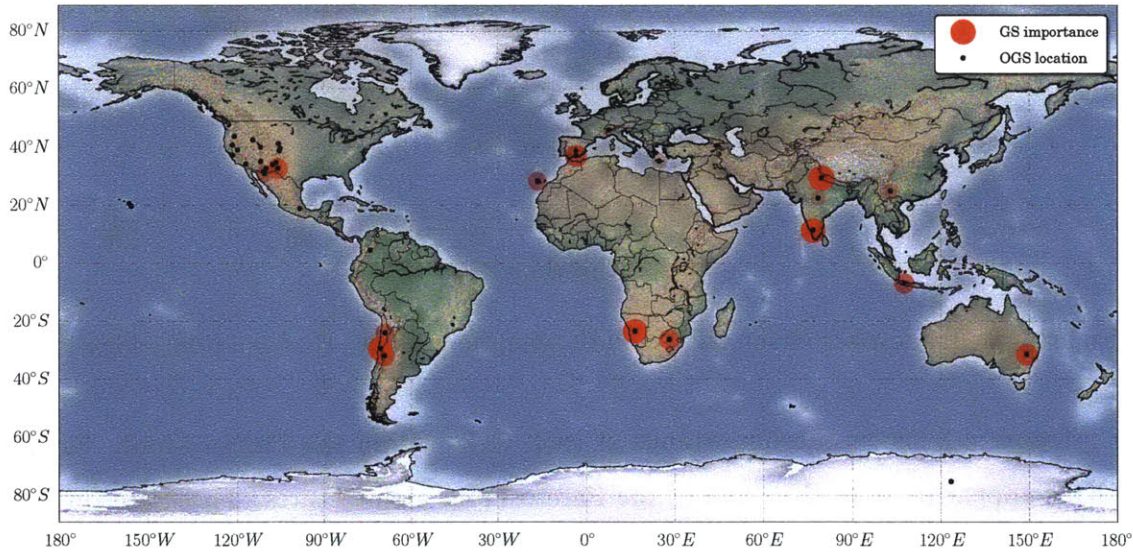
(b) Worldmap showing the importance of each OGS of Set D for the GEO no ISL scenario.

Figure 4-9: OGS importance for the GEO no ISL scenario with Set D of candidate locations

Unconstrained optimization

The previous analyses have considered fixed sets of candidate locations to serve as OGSs for a space optical communications network. However, most of the sites considered were not built originally with the purpose of serving in such a network. In consequence, the availability achieved in several of the previous analyses has been low, or a very high number of ground stations was required to reach high availability values.

This section presents the results of the unconstrained optimization analysis. In contrast to the analyses conducted in the previous three sections, here every latitude-longitude point on the Earth is considered as a potential candidate for the OGSs (with the exception of points in certain countries that are banned due to political reasons following the guidelines explained in Appendix B). Note that the unconstrained scenario is a completely different analysis, with which the question of what are the trade-offs between constructing new OGSs and using existing facilities in terms of availability and cost is answered.

The analysis of the unconstrained scenario is a more challenging problem from an optimization standpoint, as the number of candidate locations is multiple orders of magnitude larger than in previous analyses. In order to explore the tradespace defined by this set of candidate locations, the variable chromosome length genetic algorithm described in Section 2.4.2 is employed. The algorithm is configured to run for 25 generations with 200,000 architectures as its population size. The rest of the parameters are set to their default values.

Figure 4-10 shows the resulting tradespace after the algorithm has reached the termination condition. In this case, an availability of 89.6% can be achieved at a cost of $200 M, whereas architectures with a cost of $400 M attain an availability of 96.2%. The maximum availability achievable is 99.996%, even though the required number of OGSs is extremely large (25 sites are required). Architectures with 15 OGSs and a cost of $650 M present availabilities higher than 99%. Note that this extra degree of freedom provided by the unconstrained optimization allows the increase of availability

to values close to 100% at a reasonable cost.
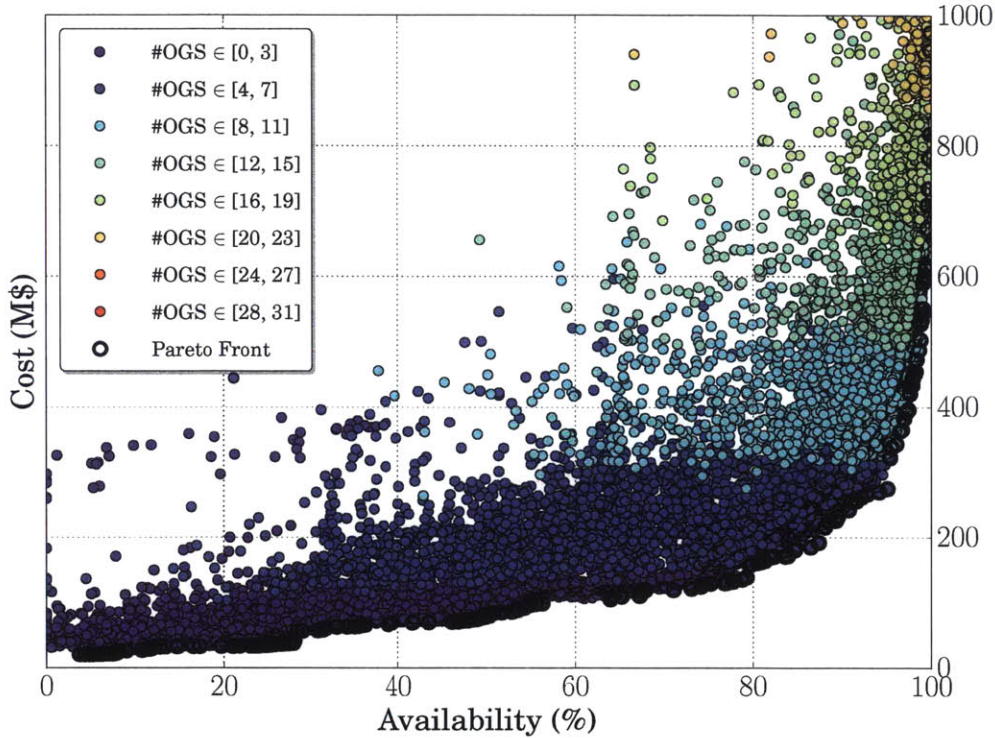
Figure 4-10: Tradespace of the GEO no ISL scenario with Set E of candidate locations.

Figure 4-11 shows the highest ranked locations in the Location Score Worldmap. The regions colored in red and white correspond to high popularity regions in the Pareto Front (i.e., those regions that have a high score in the Location Score Worldmap). Among the sites with highest scores, several already known good candidate locations are identified. These locations include the west coast of the U.S., the east and west coasts of Australia, South Africa, the Andean region in Chile, or the north of Namibia. Note that all of these locations were identified as promising locations in the studies previously conducted in this thesis. Indeed, all these locations have existing astronomical observatories that could be used as part of the ground segment for an optical space network. In addition to these regions, several new candidate locations such as the north of Mexico, the south of Saudi Arabia, Morocco and Simpsons Desert in central Australia have been identified.
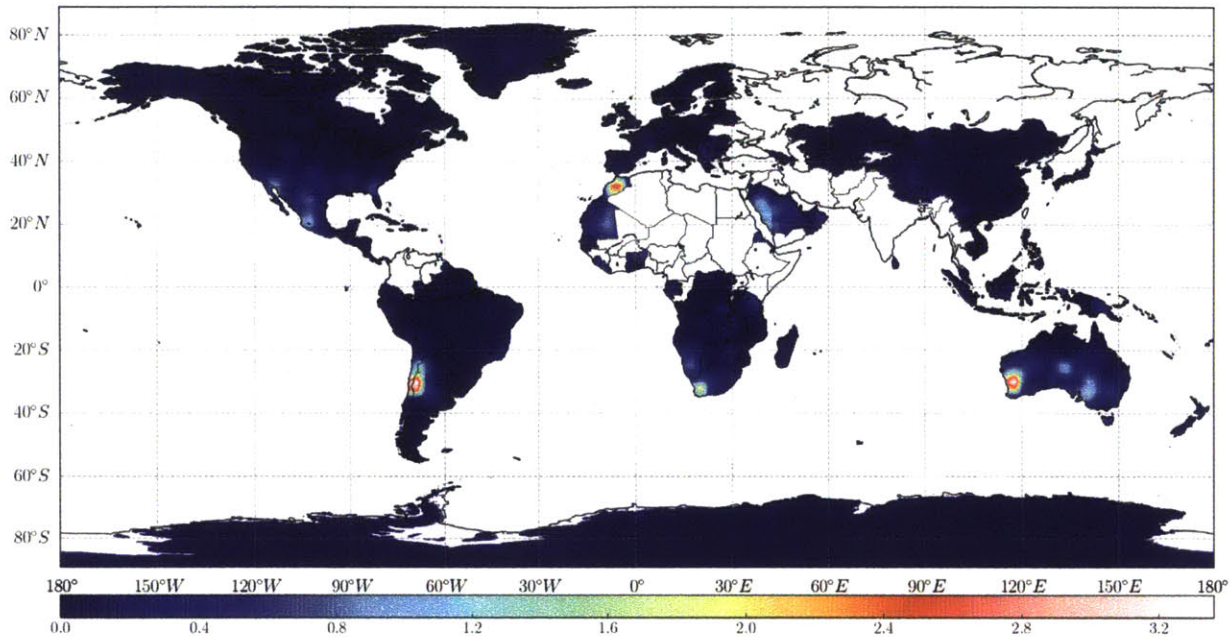
Figure 4-11: Location Score Worldmap for the Set E of candidate locations

Three main reasons explain why these locations appear as popular ones in the Location Score Worldmap:

- Located in cheap countries. All the new preferred locations are in what are considered cheap countries. This means that the cost of building and maintaining an OGS is low as compared to other alternative locations.

- Weather conditions: The new regions are located in desert-like areas, which means that they enjoy clear skies most of the year. This happens, for example, in the Chihuahuan Desert in Northern Mexico, the Sahara Desert in Morocco, the Arabian Desert in Saudi Arabia, and Simpsons Desert in central Australia.

- Distance to IXP: The new locations are relatively close to the transport network access points, which helps reduce the cost of laying down fiber optic to relay the information received to the mission operations center.

97

Comparison of results

This section's objective is to compare the results of the previous analyses, focusing on the differences among the constrained analyses and the unconstrained one. In particular, the trends and situations in which building new ground stations results in more benefits than using existing facilities are identified, and the rationale behind this behavior is explained.

Figure 4-12 shows a comparison of the Pareto Fronts obtained for each of the candidate locations sets. Note that the curves plotted correspond only to the non-dominated architectures of each analysis. Two regions can be easily distinguished in the graph. On one hand, for low availabilities, using existing assets dominates the option of building new infrastructure. On the other hand, for very high performing architectures, it is more beneficial to explore new locations than to use existing assets.
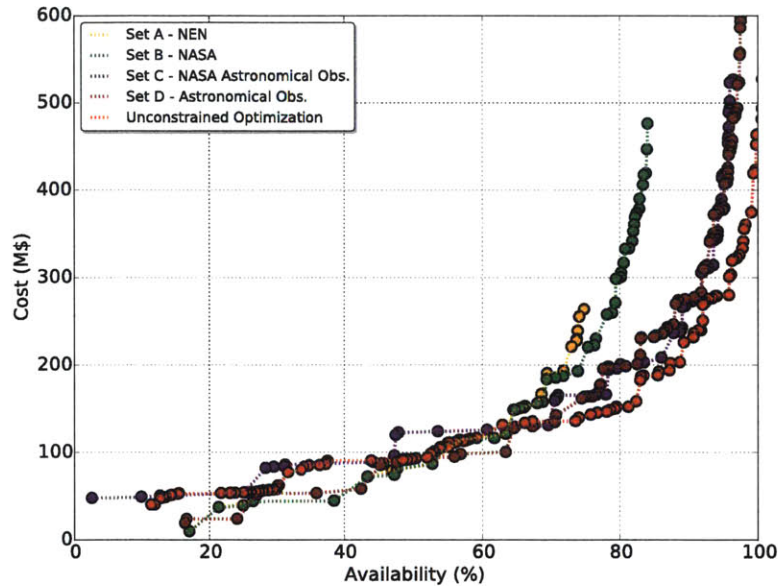
Figure 4-12: Comparison of the Pareto Fronts of the different candidate locations sets.

This discrepancy occurs as the cost of building new infrastructure implies a high investment upfront. However, when the number of existing facilities needed to provide a certain availability is high, the cost of maintenance and operations of such facilities

is higher than the cost of building a lower number of *new* OGSs that would achieve the same performance. Figure 4-13 illustrates this behavior. It can be observed that the availability attainable given a certain number of OGSs is always higher in the unconstrained set. For example, for a network with 10 OGSs, a maximum availability of 82.2% can be achieved using current NASA assets (green line), whereas this number can be increased to 95.4% using astronomical observatories, and to 97.1% using new facilities. The scenario where the candidate locations are those recommended by NASA in reference [17] offers the next higher availability. Note that values of availability which are close to 100% can be achieved only by building new OGSs.
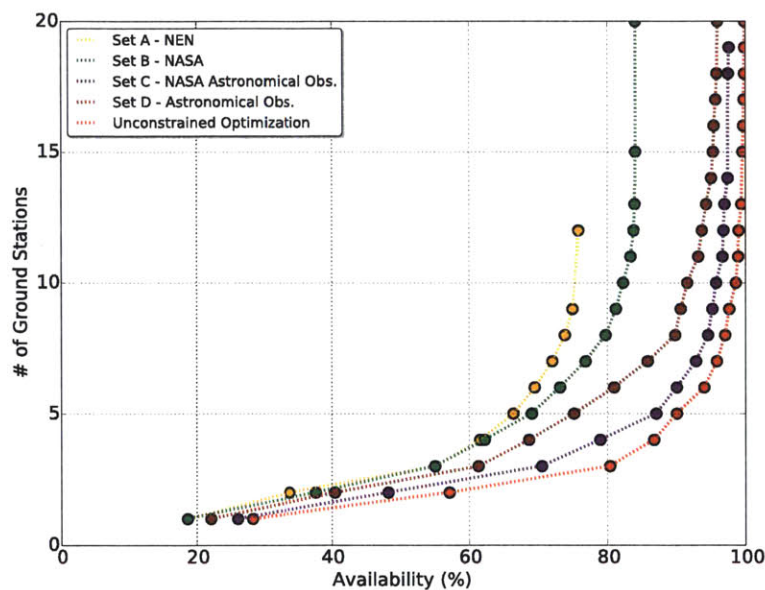
Figure 4-13: Availability vs. number of OGSs for the Pareto Fronts of the different candidate location sets.

4.3.2 Other link outage mitigation techniques

The objective of this section is to evaluate the impact of other mitigation techniques for the link outage probability due to cloud coverage. In particular, two different techniques are discussed:

- Use inter-satellite links (ISL) among the relay satellites. This way, if the OGSs in line of sight of a relay satellite in GEO are all covered by clouds, the satellite can relay its data to another relay satellite whose OGSs present clear skies. The main drawback of this approach is that the capacity of the space-to-ground links must be increased, as now satellites might have to transmit other satellites' data in addition to their own.

- Use the direct-to-Earth (DTE) approach. Instead of using relay satellites in GEO orbit, customer missions download their data directly to the network of OGSs.

Finally, even though it is not considered a mitigation technique, the distribution of the orbital slots occupied by the GEO relay satellites is analyzed. Some slots in the geostationary belt present advantageous conditions, due to the number of OGSs in line of sight. Geostationary slots are assigned by the International Telecommunications Unit (ITU) to the different satellite operators and governmental agencies, in a similar fashion as the radio-electric spectrum is allocated to different operators. Currently NASA has satellites in the following orbital slots: 41 W, 62 W, 171 W, 174 W, and 85 E. However, enabling some flexibility in the orbital slot where the relay satellites are placed might lead to increases in availability.

Inter-satellite links

This section quantifies the effect of having ISL on-board the relay satellites in terms of improvement in the availability achieved by the network. To analyze this issue, Set D of candidate OGSs (astronomical observatories at a height higher than 1000 m) is used to evaluate the performance of the architectures under Scenarios 1 (GEO + ISL) and 2 (GEO no ISL).

Figure 4-14 shows the tradespaces obtained using Set B of OGSs and the Scenarios 1 (GEO + ISL) and 2 (GEO no ISL). It can be observed that the use of ISL among the relay satellites increases the availability of the network substantially. In particular, the maximum availability attainable moves from 96.3% to 99.9%. In addition, higher

availabilities can be achieved at a lower cost. As an example, using a $200 M network with six OGSs results in an availability of 80% in the case of not using ISL, whereas this same architecture achieves an availability of 98.7% when using ISL.
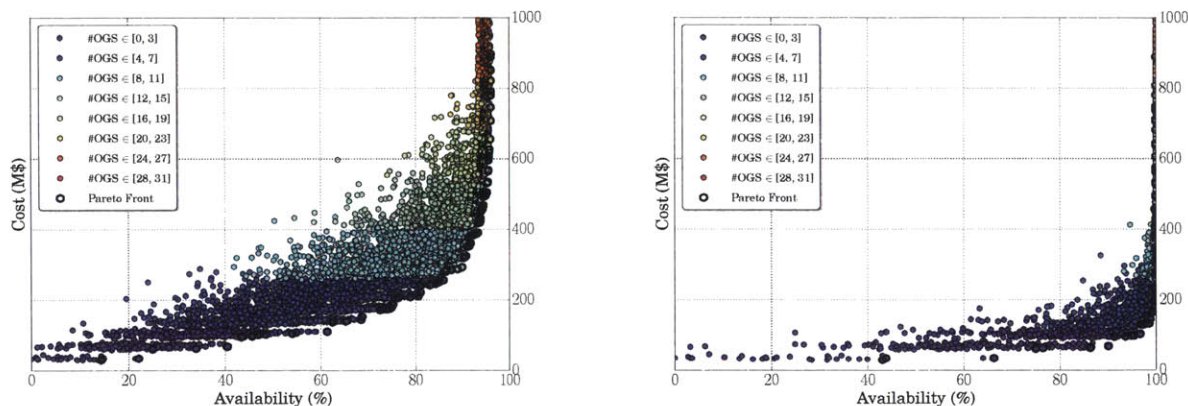
(a) Tradespace of the Scenario 1 (GEO no ISL)

(b) Tradespace of the Scenario 2 (GEO + ISL)

Figure 4-14: Tradespaces using Set B of OGSs and the Scenarios 1 and 2.

The use of ISL implies an average increase in availability of over 71.3%, even though this effect depends on the number of OGSs in the architecture. Figure 4-15 shows the increase in availability of the network (as a percentage of the *no ISL* availability) versus the number of OGSs in the architecture. Note how this increase follows a decreasing exponential trend; for architectures with a low number of OGSs, the increase in availability can be as high as 200%, whereas for architectures with a high number of OGSs (≥ 15), this increase is lower than 10%. This behavior is due to the fact that in architectures with a very low number of OGSs, all of them might be in line of sight with a unique relay satellite. Therefore, when there is no ISL available between the relay satellites, the availability is bounded to be lower than 33.3% (as only one third of the surface of the customer missions orbital-sphere is covered by the satellite). However, when using ISL, the relay satellites can communicate among them and all the surface of the orbital sphere is covered by them, extending the upper bound on the availability to be 100%. Conversely, for architectures with a high number of OGSs, all the satellites can access to multiple OGSs and the benefit of

101

using ISL is smaller.
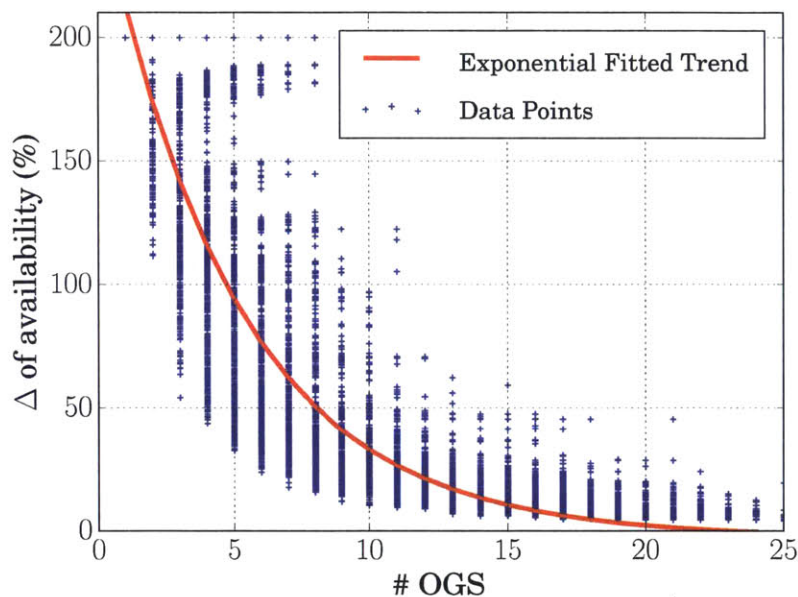
Figure 4-15: Increase in availability (in percentage) versus number of OGS in the architecture.

Finally, comparing Figure 4-16 with Figure 4-9 allows us to understand the effect of using ISL in the selection of OGSs for this particular case. In Figure 4-16 seven OGSs appear in more than half of the Pareto Front architectures, even though these are not the same locations that appear in Figure 4-9. In particular, La Silla Observatory (CL), Apache Point Observatory (US), Atacama Desert Observatory (CL), Felix Aguilar Observatory (AGR), Aryabhatta Research Institute of Observational Sciences (IN), and Ooty Radio Telescope (IN) are among the most popular choices. Note that this locations are clustered in two small regions of the planet: the Andes in Chile and the mountains in India.

Indeed, most the configurations in the Pareto Front share a common pattern in terms on how OGSs are selected. Those architectures that make use of ISL among relay satellites trend to concentrate a high number of OGSs in a single region and place a relay satellite on top of them. Then, this satellite is used as the main sink for all the traffic of the network, receiving the traffic from the other satellites through

the ISL that connects them. This design-strategy seems a reasonable choice given how the network availability (NA) is computed.
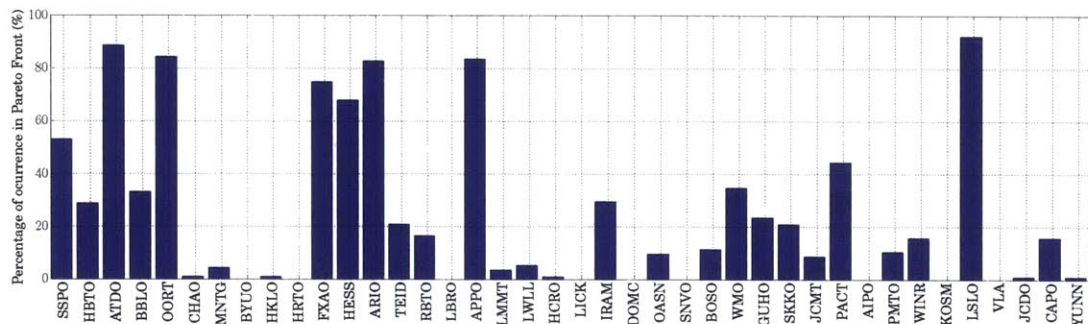
(a) Importance of each candidate OGS in the Pareto Front. The complete name of each ground station can be found in Table A.3 in Appendix A.
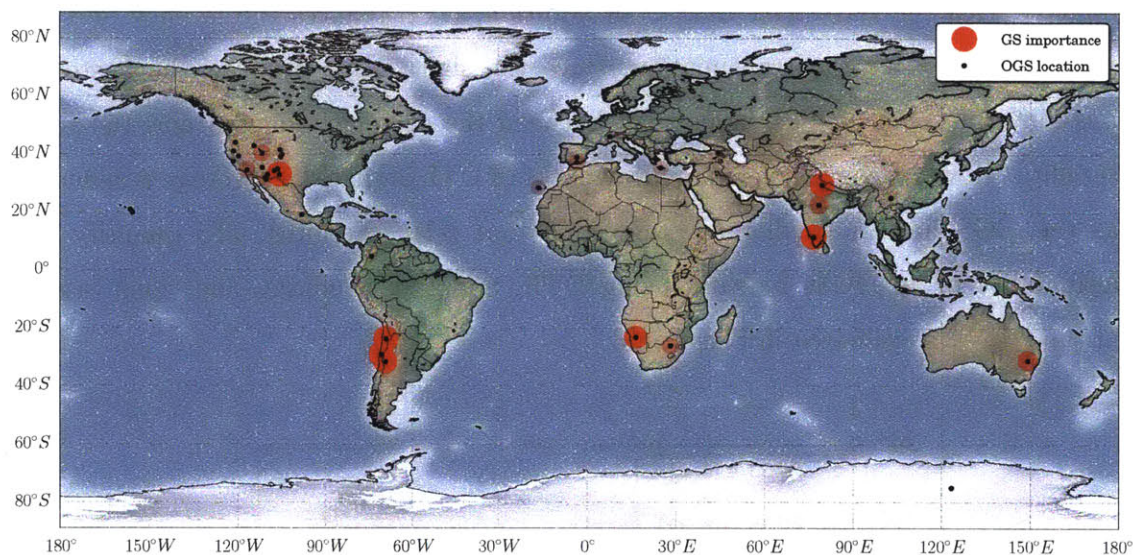
(b) Worldmap showing the importance of each OGS for the GEO + ISL scenario.

Figure 4-16: OGS importance for the Set B of candidate locations evaluated with Scenario 2 (GEO + ISL)

This approach contrasts with the one followed by architectures that do not use ISL (Scenario 2), in which OGSs trend to be equally distributed across the whole globe. This way, they construct a robust and reliable ground segment. This spread nature of the network might result in greater costs for the terrestrial back-haul network

connecting the OGSs. However, quantifying the impact of such investment is out of the scope of this thesis even though its analysis might be a good starting point for future work related to this topic. Finally, in this scenario, an OGS usually has more than one satellite in line of sight, as this contributes to reduce the LOP of both of them.

Direct to Earth approach

Another proposed approach for customer missions to transmit their data back to Earth, is to communicate directly to the OGSs. This approach is referred as Direct to Earth (DTE) communications. One of its advantages is that the expensive space segment (i.e., the relay satellites) are no needed, and customer missions can contact directly with the terrestrial OGSs. In addition, DTE reduces the latency and the power required for the transmission, since the slant range between the customer mission and the OGS is smaller than between the customer mission and the relay satellite. However, one of the main drawbacks of DTE is that the coverage is reduced, as the OGS have a smaller coverage area that relay satellites. To quantify the availability of an OGSs network using DTE, Set A of candidate locations (assets of the NEN) is evaluated in Scenario 3.
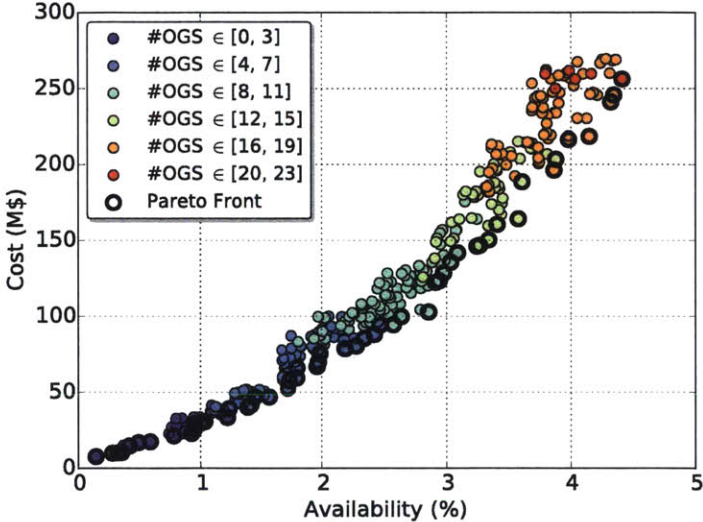
Figure 4-17: Tradespace of the Scenario 3 using Set A of candidate locations.

104

Figure 4-17 illustrates the behavior of the network when the users download their data using DTE links to the ground stations. In comparison with the other scenarios, architectures have a very low score in the NA metric. However, this results need to be interpreted carefully as the NA metric is upper-bounded by the global coverage that the network can provide. In that sense, as 71% of the Earth's surface is covered by water and because the antenna mask at a height of 600km is relatively small, the maximum availability achievable (by having a OGS on every piece of continental land) is approximately 29%. As an example, the current configuration of the NEN would score very poorly (5% availability).
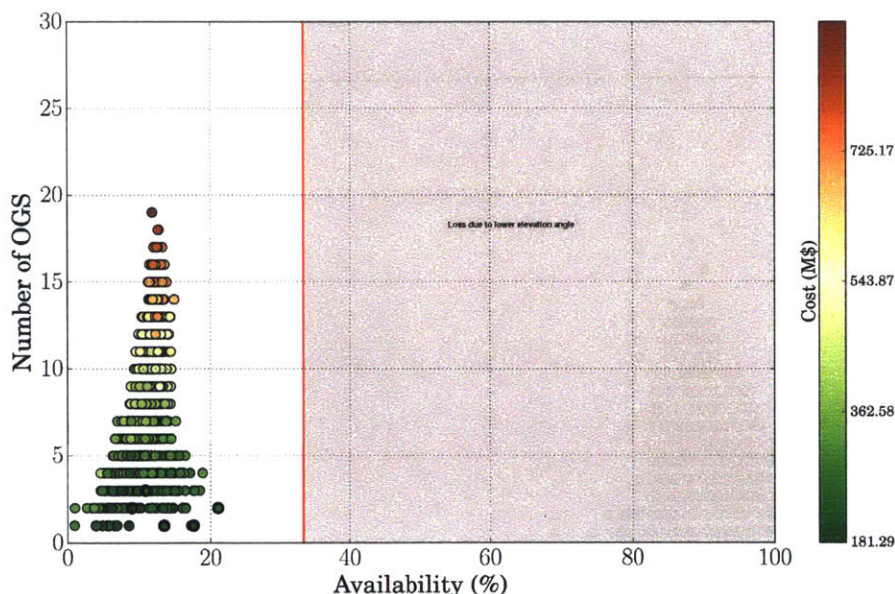
Figure 4-18: Relative availability of a network equipped with optical terminals with respect to the same network with RF equipment

It is interesting to analyze what's the availability of a network of LEO OGSs as compared to the same network equipped with RF antennas. Figure 4-18 represents the relative availability between the availability achieved by a optical network and the same network equipped with RF antennas. The mean value of this relative availability is 0.103. This means that in order to achieve the same data volume that could be downloaded with RF, satellites carrying optical terminals on-board and using the

DTE approach need to transmit at a data rate 10 times higher than with RF. Finally, this lower value of availability of optical network is due to two factors. First, as the minimum elevation angle required for optical communications is higher than for RF communications, there is a loss as the regions of coverage of the OGSs are smaller than for the RF ground stations. This loss accounts for 66.6% of the difference in availability (grayed out in Figure 4-18) for the minimum elevation angle values used in our analysis (20o for OGSs and 5o for RF terminals). Second, the cloudiness of the locations are responsible of an extra loss, which in the case of this analysis is another 60%. The effect of only cloud conditions on the relative availability between a RF-equipped and optical network using DTE is depicted in Figure 4-19.
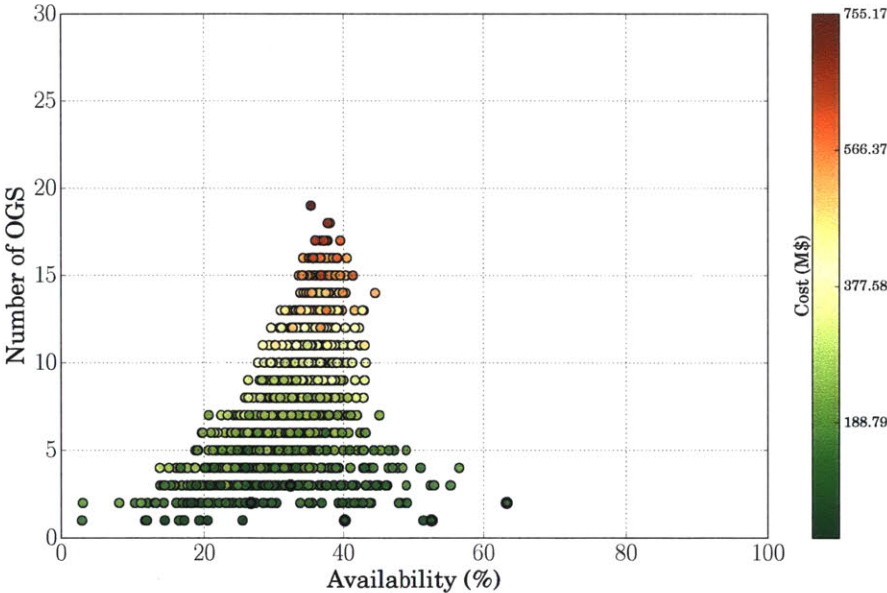
Figure 4-19: Relative availability of a network equipped with optical terminals with respect to the same network with RF equipment due only to the effect of cloud conditions

Orbital slots for the relay satellites

In this section the effect of allowing geostationary slots for the relay satellites different to those currently assigned for NASA use is quantified. The slot assignment process is coordinated by the International Telecommunications Unit (ITU-R), in order to

guarantee rational, equitable, efficient and economical use of the radio-frequency spectrum. Currently NASA has satellites in the following orbital slots: 41 W, 62 W, 171 W, 174 W, and 85 E. However, enabling some flexibility in the orbital slot where the relay satellites are placed might lead to increases in availability.

To measure this effect, Set D of candidate OGSs is used to compute the availability both for a fixed assignment of relay satellites (best choice among current NASA's slots) and the best choice considering every orbital slot in the geostationary belt. With one single constrain; the satellites must be *evenly* spaced among them (i.e., 120 deg among them ± 10 deg). Figure 4-20 shows an histogram of the gain in availability (expressed as a percentage of the availability when using the fixed assignment of relay satellites) for 3,000 architectures. The mean gain in availability when allowing flexible locations for the relay satellites is 11.8%. However, for a large number of architectures the gain is lower than 1%, which means that some specific architectures benefit a lot of new satellite allocations, while others do not observe big differences.
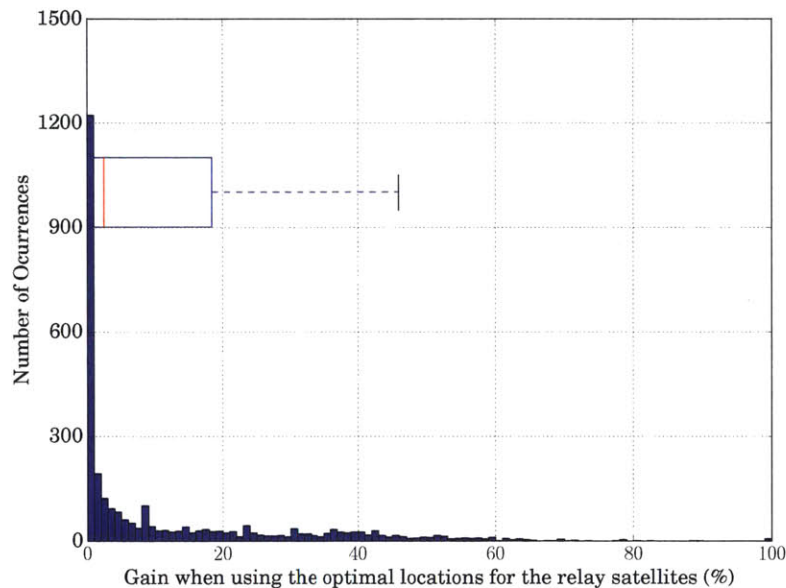
Figure 4-20: Histogram of increase in availability (in percentage) when using flexible relay satellite slot-allocations.

Finally, Figure 4-21 shows the preferred orbital slots when ONGSA chooses them

to maximize the network availability. The slots located in 146 W, 112 W, 30 W, 4 E, 90 E, and 120 E are the ones that present the highest popularity. Note that these slots correspond to two different sets of evenly-spaced orbital slots in the GEO belt (146 W, 30 W, 90 E; and 112 W, 4 E, 90 E). There are two different strategies with these locations. The first set tries to cover simultaneously several regions with favorable weather (e.g., the satellite in 30 W covers at the same time the east of Africa and the west of America, and the satellite in 90 E covers the Arabian Peninsula and the east of Australia). However, in the second set each relay satellite covers one region of the Earth: America (112 W), Europe and Africa (4 E), and Australia and the east of Asia (90 E). The choice of one or another strategy depends on the location of the ground facilities on each architecture.
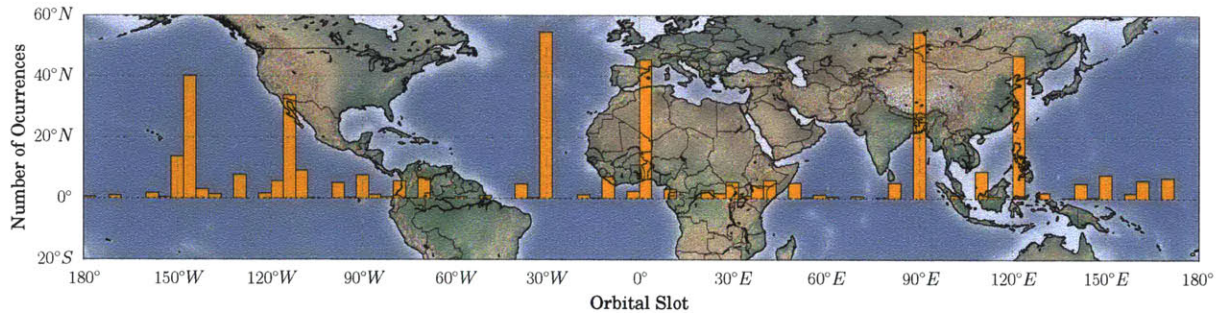
Figure 4-21: Most popular slots for the relay satellites .

108

Chapter 5

Conclusions

5.1 Thesis summary

This thesis analyzes the problem of placement of optical ground stations to maximize the availability of a space communications optical network ground segment. The first chapter explains the need for this analysis and exposes the main challenges that optical communications face when traversing the atmospheric channel. The literature review reveals three points that have not been analyzed in the previous literature and motivate this thesis. First and foremost, none of the previous approaches considered new locations as possible candidates for placing an OGS. In addition, no analyses regarding the performance of networks composed of existing assets versus networks that incorporate new locations have been conducted. Second, most of the previous works lacked an explicit cost model that allowed understanding of the trade-offs between availability and cost of different globally spread ground stations. Finally, most of the previous work focused on networks that operate in a particular region of the Earth rather than on a global scale.

The second chapter describes the Optical Network Ground Segment Analyzer (ONGSA), a computational tool that determines the optimal locations for a global network of OGSs. Section 2.2 provides a general overview of the tool. Section 2.3 describes each of the modules that compose the tool: Section 2.3.1 presents the mathematical basis of the cloud model and the dataset used; Section 2.3.2 introduces

an overview of the cost module that provides estimates of the life-cycle cost of an OGS; and lastly, Section 2.3.3 outlines the formulation of the availability model. Finally, Section 2.4 depicts the different optimization techniques built-in within ONGSA to explore the candidate location-space and determine the best architectural alternatives.

The third chapter of the thesis is devoted to the validation of ONGSA. Data from two different cloud datasets was gathered to compare the values obtained from the cloud model of ONGSA with those that result from using other datasets. The analyses validated the spatial correlation model and the network availability model. For the first one, the mean absolute error was lower than 0.057, whereas for the latter the MAE was below 0.052. The estimates computed by the cost model were benchmarked against cost values provided in the Optical Links Study Group report [17].

Finally, Chapter 4 uses several analyses to evaluate different architectural alternatives for the ground segment of an optical communications network to serve LEO satellite customer missions. First, ONGSA was used to analyze several scenarios where a set of existing facilities was considered as candidate locations. These analyses allowed us to understand the limitations associated with the use of current networks such as the DSN, the SN, the NEN, or different sets of existing astronomical observatories. Next, the tool was used in the unconstrained scenario to analyze potential new locations and the performance of an architecture that incorporates them instead of existing assets. The results of the unconstrained scenario compared favorably to those obtained when using fixed candidate sets of locations. Lastly, ONGSA was used to determine the benefit of using alternative mitigation techniques such as inter-satellite links among the relay satellites, which would allow us to reduce the number of supporting ground stations.

5.2 Main contributions

The principal goal of this thesis was to identify the optical ground segment architecture(s) that better address the needs of future near-Earth space missions by (1) implementing a model that considers cloud coverage worldwide and, given the

location of the ground stations, evaluates its availability and cost and (2) exploring the architecture space defined by combinations of ground stations, presence of relay satellites in GEO and presence of ISL among them. The achievement of these goals has led to the following contributions:

- A new simplified cloud model to assess the availability of a network of OGSs. The model uses monthly cloud probabilities (instead of previously used 15-minute interval datapoints) and incorporates a spatial correlation model to compute several-site joint cloud probabilities. The mean absolute error of this model is lower than 0.05 with respect to the values obtained using data-intensive methods. This model's simplicity and compactness enables fast evaluation and tradespace exploration analyses.

- A cost model to estimate the life-cycle investment required to build an arbitrary network of OGSs. The main cost drivers were identified and different data sources were combined to assemble the model: cost information from the Air Force was used to estimate the building costs, service pricing data from the US General Services Administration to determine the cost of the WAN fees, and models from previous literature to assess the telescope costs.

- The Optical Network Ground Segment Analyzer (ONGSA), a computational tool that determines the optimal locations for a network of OGSs. This tool integrates the two models mentioned above with a variable chromosome length genetic algorithm optimizer. The tool is capable of enumerating thousands of architectures using different search strategies and then evaluating them quickly using parallel computing. The search modes that are available depend on the size of the scenario under evaluation: full enumeration is used in those scenarios where a fixed set of candidate locations is defined, whereas genetic algorithms and variable chromosome length genetic algorithms are used for the unconstrained scenarios, where vast regions of the Earth are considered as candidate locations.

5.3 Limitations

The research conducted until now has several limitations that need to be addressed in future work. This section outlines these limitations, while Section 5.4 describes futures steps to overcome them.

- ONGSA cannot evaluate architectures where an OGS is spatially correlated to two or more other OGSs. This failure happens since the spatial correlation model can only compute the joint cloud probability of two OGSs. As described in Section 2.3.3, ONGSA eliminates the architectures that do not fulfill this condition during its search process. Expanding the current spatial correlation model so that it can capture the effect of multiple OGSs spatially correlated is one of the areas of future work. Some ideas in this direction are outlined in Section 5.4.

- The current cost model is a first order approximation, useful for comparison purposes among different architectures, of the real cost of the ground segment network. Its main limitation is the uncertainty associated with the cost of laying down optical fiber highly depends on the country, type of fiber (aerial, underground, underwater) and terrain conditions. These facts must be taken into account when assessing the significance of the results (especially when comparing certain regions of the tradespaces of different sets of architectures, as in Section 4.3.1).

- Satellite-imagery based datasets cannot model certain cloud conditions accurately. For example, satellite models normally report higher cloud probability values for those regions that are located at the top of steep mountains (e.g., Teide Observatory in the Canary Islands or Mauna Kea in Hawaii). These higher values occur since clouds linger below the actual OGS forming what is known as *a sea of clouds*, but the instrument capturing the images has not enough resolution to capture the different conditions between the mountain peak and its slopes. Solving this problem may require the use of local datasets (e.g.,

NOAA's Automated Weather Observing Systems report weather conditions at 20-minute intervals for more than 5,000 terrestrial weather stations) or more complex analytical models that include these uncommon situations.

5.4 Future work

Several areas of improvement have been identified to extend ONGSA and refine its outputs. In particular, the main streams of research for the future are these:

- Expand the cloud model to overcome the aforementioned limitations and improve the accuracy of the spatial correlation model. Two other approaches have been explored for that purpose. First, a set of Bernoulli stochastic processes that are pairwise cross-correlated by a coefficient ρ_{ij} can be used to simulate the cloud probabilities of OGSs. Monte Carlo sampling can be employed to generate a set of realizations of these stochastic processes, by drawing a set of normal random variables (latent distribution) that are later truncated. More details on this approach can be found in [35]. Second, the accuracy of the current model could be improved just by using a neural network to approximate the statistical dependence index (χ_{AB}). Preliminary results show that a mean absolute error lower than 0.02 can be achieved by using this latter method.

- Quantify the level of uncertainty in the network availability values that results from ignoring second order cloud-effects such as day-night correlations or jet-stream effects. In addition, quantify the uncertainty and understand the implications of not considering different types of clouds, with varying levels of scatter and opacity within the cloud model. Note that addressing this last point requires complex atmospheric models that consider cloud conditions at different layers of the atmosphere, and that datasets containing world-wide historical data with this information might not be available.

- Add an atmospheric channel model that accounts for the losses caused by other elements such as absorption and scattering due to aerosols, intensity

113

scintillation due to atmospheric turbulence, or fading and losses due to rain and fog. This modeling could be done using existing datasets on satellite-based aerosol concentration and type of clouds for particular regions of the Earth. However, to the best of my knowledge, no datasets that model the distribution of the refraction index structure parameter C_n^2 on every latitude-longitude point on Earth.

- Incorporate the network reliability as another metric of the tradespace in addition to the availability of the network. This reliability metric would quantify the effect on the availability of losing one of the OGSs due to maintenance operations or unexpected events. A probabilistic model that assigns different failure profiles to each ground asset (based on different conditions such as country location or weather conditions) would be necessary. The effect of the downtime on the overall network availability could be computed analytically as this value depends only on the number of ground stations a satellite can downlink information to, their failure probabilities, and the presence of ISL.

Overall, pursuing these research directions to expand ONGSA and advance the work carried out in this thesis will allow a better understanding of the trade-offs present when designing the ground segment for future optical communications networks.

Appendix A

Description of candidate locations for the different sets

Table A.1: List of Possible Locations for the OGSs for the Set 1 - NASA's NEN facilities and Set 2 - All NASA facilities

Name	Code	Latitude	Longitude	Altitude (m)	City / State	Country	Network
ᐧAlaska Satellite Facility	ASF	64.86	−147.85	0.0	Alaska	USA	NEN (NASA)
Canberra DSN	CAN	−35.40	148.98	48.0	Canberra	Australia	DSN
Clewiston	CLE	26.73	−82.03	3.0	Florida	USA	NEN (Others)
Esrange	ESR	67.88	21.07	341.0	Esrange	Sweden	NEN (Others)
Florida Ground Station	FGS	29.00	−81.00	0.0	Florida	USA	NEN (NASA)
Fucino	FUC	42.00	13.55	652.0	Fucino	Italy	NEN (Others)
Goldstone DSN	GOLD	35.30	−116.91	987.0	California	USA	DSN
Guam Remote	GRT	13.59	144.84	134.0	Guam	USA	SN
Hartebeesthoek	HBK	−25.64	28.08	1288.0	Hartebeesthoek	South Africa	NEN (Others)
Inuvik	INU	68.40	−133.50	51.0	Inuvik	Canada	NEN (Others)
Madrid DSN	MAD	40.44	−4.24	648.0	Madrid	Spain	DSN
McMurdo Ground Station	MMGS	−77.81	166.69	183.0	McMurdo	Antartica	NEN (NASA)
North Pole	NPE	64.80	−147.50	145.0	Alaska	USA	NEN (Others)
O'Higgins	O'H	−63.32	−57.90	26.0	-	Antartica	NEN (Others)
Poker Flat	PFA	65.12	−148.45	0.0	Alaska	USA	NEN (Others)
Punta Arenas	PAN	−53.00	−71.00	88.0		Argentina	NEN (Others)
Santiago Satellite Station	SSS	−33.13	−70.67	698.0	Santiago	Chile	NEN (Others)
South Point	SPN	19.00	−155.60	164.0	Hawaii	USA	NEN (Others)
Svalbard Ground Station	SGS	78.22	15.39	248.0	Svalbard	Norway	NEN (NASA)
USN Western Australia	USNWA	−29.05	114.90	24.0	-	Australia	NEN (Others)
Wallops Flight Facility Ground Stations	WFF	37.94	−75.49	11.0	Virginia	USA	NEN (NASA)
Weilheim	WEIL	47.84	11.14	561.0	Weilheim	Germany	NEN (Others)
White Sands	WSC	32.38	−106.49	1313.0	New Mexico	USA	SN
Yatharagga	YATH	−29.05	115.35	280.0	-	Australia	NEN (Others)

Table A.2: List of Possible Locations for the OGSs for the Set 3 - Astronomical Observatories proposed by NASA

Name	Code	Latitude	Longitude	Altitude (m)	City / State	Country	Network
AliceSprings	ALIC	−23.70	133.88	581.0	-	Australia	Observatories
AngloAust	ANGL	−31.28	149.07	1135.0	-	Australia	Observatories
Arequipa	ARQP	−16.41	−71.54	2321.0	Arequipa	Peru	Observatories
Astron	ASTR	−32.38	20.81	1737.0	-	South Africa	Observatories
Brukkaros	BRKK	−25.88	17.78	945.0	-	Namibia	Observatories
CalarAlto	CALR	37.22	−2.55	2157.0	Granada	Spain	Observatories
Gamsberg	GAMB	−23.33	16.33	1781.0	-	Namibia	Observatories
HESS	HESS	−22.61	17.06	1706.0	Windhoek	Namibia	Observatories
KittPeak	KITT	31.96	−111.60	1991.0	Arizona	USA	Observatories
La Palma	PALM	28.71	−17.91	1006.0	Canary Islands	Spain	Observatories
LasCampanas	CAMP	−33.42	−70.56	688.0	-	Chile	Observatories
LaSilla	LSILL	−29.26	−70.74	2332.0	-	Chile	Observatories
MaunaKea	MAUK	19.82	−155.47	4184.0	Hawaii	USA	Observatories
McDonald	MCDN	30.67	−104.02	2001.0	Texas	USA	Observatories
Haleakala	HKLA	20.72	−156.26	2109.0	Hawaii	USA	Observatories
Stromlo	STRM	−35.32	149.01	779.0	-	Australia	Observatories
Wilson	WILS	34.23	−118.07	1728.0	California	USA	Observatories
Palomar	PLMR	33.36	−116.84	1780.0	California	USA	Observatories
Paranal	PRNL	−24.63	−70.40	2065.0	Cerro Paranal	Chile	Observatories
Perth	PERT	−32.07	115.83	25.0	Perth	Australia	Observatories
PurpleMountain	PPMT	32.07	118.83	159.0	-	China	Observatories
ShokinMajdanak	SHMJ	38.72	66.88		-	Uzbekistan	Observatories
Starfire	STAR	34.52	−105.87	1950.0	New Mexico	USA	Observatories
TableMountain	TABM	37.19	−118.58	2719.0	California	USA	Observatories
Teide	TEID	28.27	−16.64	2340.0	Canary Islands	Spain	Observatories

Table A.3: List of Possible Locations for the OGSs for the Set 4 - Astronomical Observatories > 1000 m

Name	Code	Latitude	Longitude	Altitude (m)	City / State	Country
Airdrie Public Observatory	AIPO	55.90	−4.00	1085.0	Airdrie	Scotland
Apache Point Observatory	APPO	32.80	−105.80	2791.6	New Mexico	USA
Aryabhatta Research Institute of Observational Sciences	ARIO	29.40	79.50	1932.0	Uttarakhand	India
Atacama Desert Observatory	ATDO	−23.90	−69.10	2641.7	Antofagasta	Chile
Big Bear Lake Solar Observatory	BBLO	34.30	−116.90	2057.3	Big Bear City	California
Bosscha Observatory	BOSO	−6.80	107.60	1304.9	West Java	Indonesia
Byurakan Observatory	BYUO	40.50	44.20	4058.8	Mount Aragats	Armenia
Capilla Peak Observatory	CAPO	34.70	−106.40	2837.6	New Mexico	USA
Chamberlin Observatory	CHAO	39.70	−105.00	1643.1	Denver	Colorado
Dome C	DOMC	−75.10	123.40	3265.0	-	Antartica
Felix Aguilar Observatory	FXAO	−31.80	−69.30	2420.5	San Juan	Argentina
Guillermo Haro Observatory	GUHO	31.10	−110.40	2477.3	Sonora	Mexico
Haleakala Observatory	HKLO	20.72	−156.26	3025.5	Hawaii	USA
Hartebeesthoek Radio Astronomy Observatory	HBTO	−25.64	28.08	1723.5	Gauteng	South Africa
Hat Creek Radio Observatory	HCRO	40.80	−121.50	1018.9	Shasta County	California
Herrett Observatory	HRTO	42.60	−114.50	1138.2	Twin Falls	Idaho
High Energy Stereoscopic System	HESS	−23.30	16.50	1826.7	Khomas Region	Namibia
IRAM 30m Telescope	IRAM	37.10	−3.40	3364.5	Pico Veleta	Spain
Jack C. Davis Observatory	JCDO	39.20	−119.80	1426.8	Carson City	Nevada
James Clerk Maxwell Telescope	JCMT	19.80	−155.50	4197.3	Mauna Kea	Hawaii
KOSMA Observatory	KOSM	46.00	7.80	3109.7	Gornergrat	Switzerland
La Silla Observatory	LSLO	−29.26	−70.74	2331.1	CoquimboÂä	Chile
Large Millimeter Telescope	LMMT	19.00	−98.20	2144.0	Puebla	Mexico
Las Brisas Observatory	LBRO	38.90	−105.30	2615.8	Colorado	USA
Lick Observatory	LICK	37.30	−121.60	1285.4	Mount Hamilton	San Jose
Lowell Observatory	LWLL	35.20	−111.70	2204.9	Arizona	USA
Mount Graham	MNTG	32.70	−109.90	3259.3	Arizona	USA
Observatorio Astronomico Nacional	OASN	4.60	−74.10	2555.0	Bogota	Colombia
Ooty Radio Telescope	OORT	11.40	76.70	2249.1	Tamil Nadu	India
Pachmarhi Array of Cerenkov Telescopes (PACT)	PACT	22.50	78.40	1065.7	Madhya Pradesh	India
Pine Mountain Observatory	PMTO	43.80	−120.90	1908.8	Bend	Oregon
Red Buttes Observatory	RBTO	41.30	−105.60	2184.2	Laramie	Wyoming
Siding Spring Observatory	SSPO	−31.30	149.10	1134.7	New South Wales	Australia
Sierra Nevada Observatory	SNVO	38.80	−3.40	2034.7	Sierra Nevada	Spain
Skinakas Observatory	SKKO	35.20	24.80	1585.3	Crete	Greece
Teide Observatory	TEID	28.27	−16.64	2386.2	Tenerife	Canary Islands
Very Large Array	VLA	34.10	−107.60	2123.7	Socorro	New Mexico
West Mountain Observatory	WMO	40.10	−111.80	1385.7	Utah	USA
Winer Observatory	WINR	31.70	−110.70	1488.8	Sonoita	Arizona
Yunnan Astronomical Observatory	YUNN	24.90	102.80	1929.9	Yunnan	China

THIS PAGE INTENTIONALLY LEFT BLANK

Appendix B

Politically unstable countries banning criteria

This Appendix describes the procedure followed in order to determine which politically unstable countries were banned from our analyses. As described in Section 1.3.3, one of the main requirements for a candidate OGS location is to be in a politically stable country. Determining which countries can be categorized as politically stable is a complex question that is subject to geopolitical interests, international relations and partnerships with local governments, etc. In order to objectively determine which countries are and are not politically stable, the *Political Stability and Absence of Violence/Terrorism* index from the Worldwide Governance Indicators dataset of the WorldBank will be used.

The *Political Stability and Absence of Violence/Terrorism* index measures perceptions of the likelihood of political instability and/or politically motivated violence, including terrorism. It combines a variety of metrics such as intensity of internal conflicts, govern stability, political terror scale, violent demonstrations, presence of armed conflict or terrorism thread, and international tensions. After processing all the available values for the metrics defined, values are aggregated into a single metric that ranks from 0 to 100.
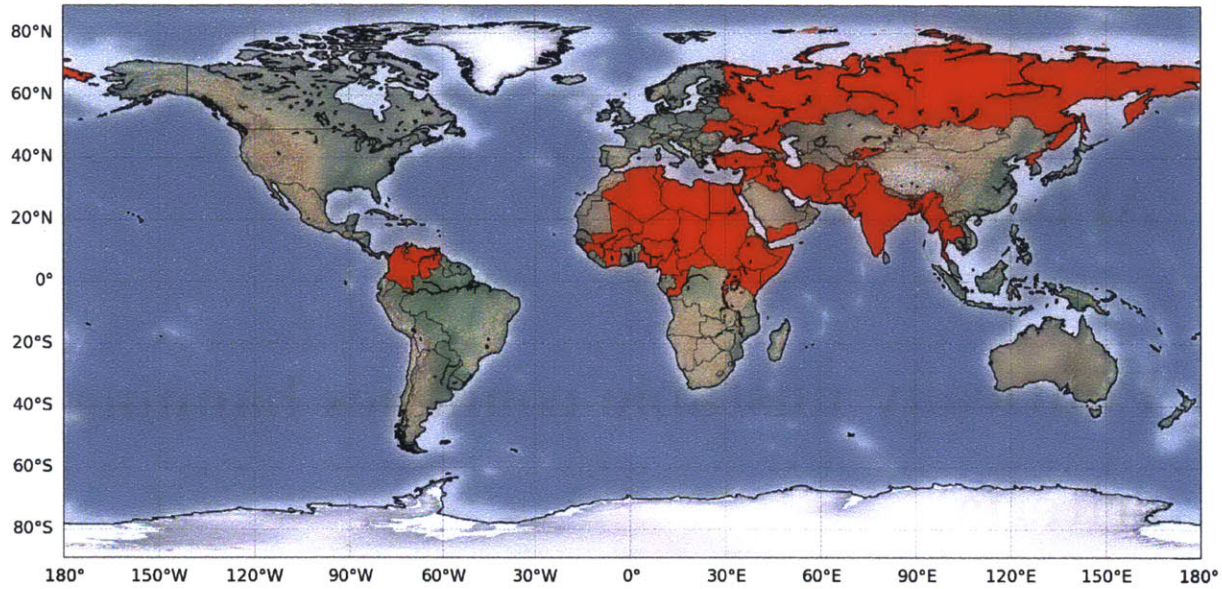
Figure B-1: Banned countries for the Set E of candidate locations described in Section 4.2.1

In the unconstrained scenario we decided to ban those countries that have a value for the indicator lower than 20%. Note that as the indicator is comparative, this corresponds to ban the 20% lowest scoring countries, or in other words, the 20% less politically stable countries. Table B.1 shows which countries were banned as well as their score in the *Political Stability and Absence of Violence/Terrorism* index. Figure B-1 highlights these countries in red in a world map.

Note how most of the countries in Saharan Africa were considered unstable, as well as those in the Middle East and most of the countries in the South of Asia (from Syria and Iraq to Myanmar and Thailand going through India and Pakistan). In addition, Colombia and Venezuela in the north of South America, as well as Russia were banned.

Table B.1: List of banned countries for the unconstrained scenario described in Section 4.2.1

Country	%	Country	%	Country	%	Country	%
Syria	0.0	Nigeria	5.3	Colombia	10.7	Uganda	16.0
Central African Rep.	0.5	Palestine	5.8	North Korea	11.2	Thailand	16.5
Sudan	1.0	Ukraine	6.3	Burma	11.7	Iran	17.0
Yemen	1.5	Mali	6.8	Turkey	12.1	Burundi	17.5
Somalia	1.9	Lebanon	7.3	Cote d'Ivore	12.6	Bangladesh	18.0
Iraq	2.4	Egypt	7.8	Israel	13.1	Russia	18.4
Afghanistan	2.9	Chad	8.3	India	13.6	Venezuela	18.9
Pakistan	3.4	Kenya	8.7	Cameroon	14.1	Burkina Faso	19.4
Sudan	3.9	Niger	9.2	Bahrain	14.6	Kyrgyzstan	19.9
Libya	4.4	Ethiopia	9.7	Tunisia	15.0		
Congo	4.9	Algeria	10.2	Guinea	15.5		

THIS PAGE INTENTIONALLY LEFT BLANK

Bibliography

[1] Larry C Andrews and Ronald L Phillips. *Laser beam propagation through random media*, volume 52. SPIE press Bellingham, WA, 2005.

[2] Pierre Yves Bely. Large space optics. In *Next Generation Space Telescope Science and Technology*, volume 207, page 25, 2000.

[3] Abhijit Biswas, Keith E Wilson, Sabino Piazzolla, Janet P Wu, and William H Farr. Deep-space optical communications link availability and data volume. In *Lasers and Applications in Science and Engineering*, pages 175–183. International Society for Optics and Photonics, 2004.

[4] Alexandru Horia Brie and Philippe Morignot. Genetic planning using variable length chromosomes. In *ICAPS*, pages 320–329, 2005.

[5] Vincent WS Chan. Free-space optical communications. *Lightwave Technology, Journal of*, 24(12):4750–4762, 2006.

[6] Kalyanmoy Deb, Amrit Pratap, Sameer Agarwal, and TAMT Meyarivan. A fast and elitist multiobjective genetic algorithm: NSGA-II. *Evolutionary Computation, IEEE Transactions on*, 6(2):182–197, 2002.

[7] Department of Defense. The DoD Facilities Pricing Guide, 2015.

[8] M Derrien and H Le Gléau. Msg/seviri cloud mask and type from safnwc. *International Journal of Remote Sensing*, 26(21):4707–4732, 2005.

[9] EUMETSAT. MSG Ground Segment LRIT/HRIT Mission Specific Implementation, 2015.

[10] Christian Fuchs and Florian Moll. Ground station network optimization for space-to-ground optical communication links. *Optical Communications and Networking, IEEE/OSA Journal of*, 7(12):1148–1159, 2015.

[11] Stephane Gagnon, Bruno Sylvestre, Louis Gagnon, Alexander Koujelev, Daniel Gratton, and Steve Hranilovic. Recent developments in satellite laser communications: Canadian context. In *Proceedings of 2012 International Conference on Space Optical Systems and Applications*, pages 9–12, 2012.

[12] Pedro Garcia, Ana Benarroch, and Jose Manuel Riera. Spatial distribution of cloud cover. *International Journal of Satellite Communications and Networking*, 26(2):141–155, 2008.

[13] M Reyes Garcia-Talavera, C Rivera, G Murga, I Montilla, and A Alonso. Analysis of large optical ground stations for deep-space optical communications. In *International Conference on Space Optics*, volume 7, page 10, 2014.

[14] Ahmad Gharanjik, Konstantinos Liolis, MR Shankar, and Bjorn Ottersten. Spatial multiplexing in optical feeder links for high throughput satellites. In *Signal and Information Processing (GlobalSIP), 2014 IEEE Global Conference on*, pages 1112–1116. IEEE, 2014.

[15] Dirk Giggenbach, Florian Moll, Christian Fuchs, and Martin Brechtelsbauer. Direct optical high speed downlinks and ground station networks for small LEO missions. In *16th Ka-and Broadband communications conference*, 2010.

[16] MC Green and Milton Lomask. Vanguard-a history. 1970.

[17] Optical Link Study Group. Optical link study group final report. Technical report, Interagency Operations Advisory Group, June 2012.

[18] Hamid Hemmati. *Near-earth laser communications*. CRC Press, 2009.

[19] Hennes Henniger and Otakar Wilfert. An introduction to free-space optical communications. *Radioengineering*, 19(2):203–212, 2010.

[20] John H Holland. *Adaptation in natural and artificial systems: an introductory analysis with applications to biology, control, and artificial intelligence*. U Michigan Press, 1975.

[21] David J. Israel, Gregory W. Heckler, and Robert J. Menrad. Space mobile network: A near earth communications and navigation architecture. In *2016 IEEE Aerospace Conference*, 2016.

[22] Il Yong Kim and OL De Weck. Variable chromosome length genetic algorithm for progressive refinement in topology optimization. *Structural and Multidisciplinary Optimization*, 29(6):445–456, 2005.

[23] F Lacoste, A Guérin, A Laurens, G Azema, C Périard, and D Grimal. Fso ground network optimization and analysis considering the influence of clouds. In *Antennas and Propagation (EUCAP), Proceedings of the 5th European Conference on*, pages 2746–2750. IEEE, 2011.

[24] JR Lesh and DL Robinson. A cost-performance model for ground-based optical communications receiving telescopes. *TDA Progress Report 42*, 87:56–64, 1986.

[25] Robert Link, Mary Ellen Craddock, and Randall J Alliss. Mitigating the impact of clouds on optical communications. In *Aerospace Conference, 2005 IEEE*, pages 1258–1265. IEEE, 2005.

[26] Arun K Majumdar. *Advanced Free Space Optics (FSO): A Systems Approach*, volume 186. Springer, 2014.

[27] Ujjwal Maulik and Sanghamitra Bandyopadhyay. Fuzzy partitioning using a real-coded variable-length genetic algorithm for pixel classification. *Geoscience and Remote Sensing, IEEE Transactions on*, 41(5):1075–1081, 2003.

[28] Florian Moll and Markus Knapek. Wavelength selection criteria and link availability due to cloud coverage statistics and attenuation affecting satellite, aerial, and downlink scenarios. In *Optical Engineering+ Applications*, pages 670916–670916. International Society for Optics and Photonics, 2007.

[29] Office of the Assistant Secretary for Research and Technology, U.S. Department of Transportation. Unit cost entries for fiber optic cable installation.

[30] Nicolas Perlot and Josep Perdigues-Armengol. Model-oriented availability analysis of optical GEO-ground links. In *SPIE LASE*, pages 82460P–82460P. International Society for Optics and Photonics, 2012.

[31] S Poulenard, M Ruellan, B Roy, J Riédi, F Parol, and A Rissons. High altitude clouds impacts on the design of optical feeder link and optical ground station network for future broadband satellite services. In *SPIE LASE*, pages 897107–897107. International Society for Optics and Photonics, 2014.

[32] Sylvain Poulenard, Michael Crosnier, and Angélique Rissons. Ground segment design for broadband geostationary satellite with optical feeder link. *Journal of Optical Communications and Networking*, 7(4):325–336, 2015.

[33] William B Rossow and Robert A Schiffer. Isccp cloud data products. *Bulletin of the American Meteorological Society*, 72(1):2–20, 1991.

[34] Marc Sanchez Net, Iñigo del Portillo, Bruce Cameron, Edward F Crawley, and Daniel Selva. Integrated tradespace analysis of space network architectures. *Journal of Aerospace Information Systems*, 12(8):564–578, 2015.

[35] Marc Sanchez Net, Iñigo del Portillo, Bruce Cameron, Edward F Crawley, and Daniel Selva. Approximation methods for estimating the availability of optical ground networks (manuscript in preparation). *Journal of Optical Communications and Networking*, 2016.

[36] Theodor Schmidt-Kaler and Peter Rucks. Telescope costs and cost reduction. In *Optical Telescopes of Today and Tomorrow*, pages 635–640. International Society for Optics and Photonics, 1997.

[37] KJ Schulz, J Rush, et al. Optical link study group final report. *IOAG-15b, June*, 2012.

[38] Daniel Selva. *Rule-based System Architecting of Earth Observation Satellite Systems*. PhD thesis, Massachusetts Institute of Technology Department of Aeronautics and Astronautics, Cambridge, Massachusetts, June 2012.

[39] Daniel Selva. *Rule-based System Architecting of Earth Observation Satellite Systems*. PhD thesis, Massachusetts Institute of Technology Department of Aeronautics and Astronautics, Cambridge, Massachusetts, June 2012.

[40] Willard L. Simmons. *A Framework for Decision Support in Systems Architecting*. PhD thesis, Massachusetts Institute of Technology Department of Aeronautics and Astronautics, Cambridge, Massachusetts, February 2008.

[41] H. Philip Stahl, Ginger Holmes Rowell, Gayle Reese, and Alicia Byberg. Multivariable parametric cost model for ground-based telescopes. volume 5497, pages 173–180, 2004.

[42] Larry M Stepp, Larry G Daggert, and Paul E Gillett. Estimating the cost of extremely large telescopes. In *Astronomical Telescopes and Instrumentation*, pages 309–321. International Society for Optics and Photonics, 2003.

[43] Gilbert Syswerda. Uniform crossover in genetic algorithms. 1989.

[44] Yoshihisa Takayama, Morio Toyoshima, and Nobuhiro Kura. Estimation of accessible probability in a low earth orbit satellite to ground laser communications. *Radioengineering*, 19(2):249–253, 2010.

[45] J Teles, MV Samii, and CE Doll. Overview of TDRSS. *Advances in Space Research*, 16(12):67–76, 1995.

[46] Gary S Wojcik, Heather L Szymczak, Randall J Alliss, Robert P Link, Mary Ellen Craddock, and Michael L Mason. Deep-space to ground laser communications in a cloudy world. In *Optics & Photonics 2005*, pages 589203–589203. International Society for Optics and Photonics, 2005.

[47] B Younes, K Perko, and J Shier. Space communications and navigation (scan) network architecture definition document (add) volume 1: Executive summary. *NASA SCaN-ADD-V1, Revision*, 2:21.